Title
Elucidating structure-function relationships in molybdenum chalcogenides for H adsorption and electrocatalysis

Author
Ortiz-Rodríguez, Jessica Cristina

Publication Date
2023

Peer reviewed|Thesis/dissertation

Elucidating structure-function relationships in molybdenum chalcogenides for H adsorption and electrocatalysis

By

JESSICA CRISTINA ORTIZ-RODRÍGUEZ

DISSERTATION

Submitted in partial satisfaction of the requirements for the degree of

DOCTOR OF PHILOSOPHY

in

Chemistry

in the

OFFICE OF GRADUATE STUDIES

of the

UNIVERSITY OF CALIFORNIA

DAVIS

Approved:

Jesús M. Velázquez, Chair

Louise Berben

Susan M. Kauzlarich

Committee in Charge

2023

Dedication

I would like to dedicate this work to Joshua Jude. An amazing colleague, friend, baker, and the best dancer.

May all the days in heaven be a dance floor.

Acknowledgements

I would like to begin by thanking my advisor, Professor Jesús Velázquez for taking a chance on me and allowing me to participate in the UC Davis ChemEnergy REU in 2017. Thank you for always believing in me and reminding me to "connect with the why" when things get complicated. I am grateful for the academic and moral support of Dr. Ivonne Ferrer. Thanks for making me feel that I have a family here. I am also thankful for my co-workers at the Velázquez lab. A special thanks to Dr. Joseph Perryman for all the time invested in making me a better writer and scientist. I also thank Dr. Brian Wuille Bille for incentivizing curiosity through his insightful questions.

I am deeply grateful for all the collaborators that believed in my work and helped enhance my scientific stories. It was a pleasure to work with Prof. Charles Musgrave, Dr. Nicholas R. Singstock, Prof. Bryan Enderle, Prof. Kristina Lilova, and many other scientists throughout my doctorate degree. I also acknowledge my dissertation committee members, Prof. Susan Kauzlarich and Prof. Louise Berben, for their availability and support in moving my reaching projects forward.

I am very fortunate to have interacted with great mentors that guided me through undergrad and helped me get into graduate school. Special thanks to Prof. William Atchison, Prof. Claudia Turro, Cyndi Freeman, Prof. Dalvin Méndez-Hernández, Prof. Robert Ross, Prof. Vibha Bansal and Dr. Alexandra Colón-Rodríguez. Thanks for all your time and dedication to increasing minority representation in STEM fields. Lastly, I would like to thank all my family and friends who served as my support system on this journey. Thanks for celebrating every accomplishment, as little as it may seem.

Copyright and Publication Information

This dissertation is based on the following publications:

1. Ortiz-Rodríguez, J.C. †; Singstock, N. †; Perryman, J.; Hyler, F.; Jones, S.; Holder, A.; Musgrave, C.*; Velázquez, J. M.*, Stabilizing Hydrogen Adsorption Through Theory-Guided Substitution in Chevrel-Phase Mo6X8 (X=S, Se, Te) Electrocatalysts, *ACS Applied Materials and Interfaces*, 2020, 12 (32) 35995–36003.
2. Ortiz-Rodríguez, J.C.; Perryman, J.T.; Velázquez, J.M.*, Charge transport dynamics in microwave synthesized one-dimensional molybdenum chalcogenides, *Industrial & Engineering Chemistry Research*, 2021, 60 (45) 16153–16161.
3. Ortiz-Rodríguez, J.C.; Velázquez, J.M., Structure-reactivity relationships in Chevrel Phase electrocatalysts for small-molecule reduction reactions, *Current Opinion in Electrochemistry*, 2022, 34, 101002.

† Joint first author

* Corresponding author

Abstract

The increased energy demands of the rising global population in a fossil fuel-based energy economy have caused unprecedented anthropogenic CO_2 emissions, which presents a potentially irreversible threat to human societies. The imperative transition to carbon-neutral or carbon-negative energy solutions requires the interplay of advanced technologies that can provide electricity generated from renewable sources, including wind, solar, and hydropower, while also providing energy-dense liquid fuels for long-term storage. To this end, electrochemical processes such as CO_2 reduction, N_2 reduction and hydrogen evolution could provide chemical feedstocks and fuels currently obtained by large-scale emission processes without requiring massive changes to the present energy infrastructures. The economic viability of this approach is highly dependent on the design of catalysts from earth-abundant elements that exhibit high activity and selectivity along with chemical and catalytic stability over long periods of operation. In aqueous solutions, CO_2 and N_2 reduction must compete with the kinetically more facile hydrogen evolution reaction, which is one of the main challenges in achieving catalytic selectivity. Therefore, understanding hydrogen adsorption interactions on the catalyst surface can simultaneously assist in improving hydrogen evolution activity, as well as increasing selectivity for CO_2 and N_2 reduction reactions. To this end, compositionally diverse families of materials such as molybdenum chalcogenides (sulfides, selenides, and tellurides) offer an ideal platform to evaluate hydrogen adsorption interactions and develop composition-structure-function relationships. This dissertation details an integrative research approach that includes the (1) synthesis of molybdenum chalcogenides compositions through approaches that allow facile compositional changes as well as control of morphology and dimensionality, (2) characterization of their local and electronic structures, and (3) proposed structure-function relations that could assist in the design of molybdenum chalcogenides for hydrogen evolution, CO_2 reduction and N_2 reduction reactions.

Chapter 1 introduces metal chalcogenides as promising family of materials to evaluate the influence of composition, local chemical coordination, and electronic structure in energy conversion reactions. A discussion of the crystal structure, thermodynamic stability, and synthetic accessibility of binary pseudo-molecular Chevrel-Phases Mo_6X_8 (X = S, Se, Te) and ternary 1-dimensional Pseudo-Chevrel-Phases ($K_2Mo_6X_6$; X=S, Se, Te) is included. Foundational information relevant to the generation of reactivity descriptors for electrocatalysis and the microwave-assisted solid state synthetic approach used in the following chapters is also provided.

Chapter 2 outlines the use of a rapid, microwave-assisted solid-state method to synthesize Chevrel-Phase sulfides, selenides, and tellurides. Hydrogen adsorption interactions are evaluated electrochemically under hydrogen evolution conditions as a function of chalcogen (S, Se, Te). Density functional theory and X-ray absorption spectroscopy are used to understand the interactions of the chalcogen with the adsorbed hydrogen and explain reactivity trends.

Chapter 3 expands the study of hydrogen adsorption interactions to Pseudo-Chevrel-Phases. Scanning electron microscopy, powder X-ray diffraction, and energy dispersive X-ray spectroscopy are used to elucidate the dimensional modifications in Pseudo-Chevrel-Phases as a function of chalcogen. Additional properties for this family of materials, such as charge transfer kinetics for proton reduction and specific capacitance are also discussed.

Chapter 4 summarizes the state of the art in experimental and computational evaluations of Chevrel Phases as electrocatalysts for hydrogen evolution, CO_2 reduction, and nitrogen reduction reactions. The review examines composition-dependent physicochemical properties that have shown promising electrocatalytic activity for such small-molecule reduction reactions. Future directions to generate promising multinary chalcogenides for energy conversion reactions are also included.

Contents

List of Abbreviations

HER	Hydrogen evolution reaction
CO_2R	CO_2 reduction
CO_2RR	CO_2 reduction reaction
NRR	N_2 reduction reaction
ORR	O_2 reduction reaction
CPs	Chevrel Phases
PCPs	Pseudo Chevrel Phases
H^*	Hydrogen adsorption
DFT	Density functional theory
XAS	X-ray absorption spectroscopy
ΔG_H	Gibbs free energy for hydrogen adsorption
PXRD	Powder X-ray diffraction
SEM	Scanning electron microscope
EDX	Energy dispersive X-ray
XPS	X-ray photoelectron spectrometer
SSRL	Stanford synchrotron radiation lightsource
PTFE	Polytetrafluoroethylene
LSV	Linear sweep voltammetry
ECSA	Electrochemically active surface area
C_{dl}	Double-layer capacitance
CV	Cyclic voltammograms
C_s	Specific capacitance
EIS	Electrochemical impedance spectroscopy
RPBE	Revised perdew-burke-ernzerhof
SCAN	Strongly constrained and appropriately normed
DOS	Densities and densities of states
NIST JANAF	National Institute of Standards and Technology Joint Army–Navy–Air Force

XANES	X-ray absorption near edge structure
R_{ct}	Charge-transfer resistance
LSV	Linear sweep voltammetry
STEM	Scanning transmission electron microscopy
i_0	Exchange current density
η	Overpotential
ECSTM	Electrochemical scanning tunneling microscopy
DEMS	Differential electrochemical mass spectrometry
FTIR	Fourier transform infrared spectroscopy

List of Figures and Tables

hydrogen evolution in Ar-saturated electrolyte. (c) Schematic illustration of the proposed binding mechanism for N_2 absorption and subsequent conversion to NH_3. Copyright 2021 American Chemical Society. Figure reproduced with permission from ref 33.

Chapter 1: Introduction

Developing sustainable net-zero emission systems to produce fuels and commodity chemicals plays a significant role in supporting the global population's needs without further negative impacts on the environment. A prospective option is to develop electrochemical conversion processes that can convert readily available molecules such as water, carbon dioxide, and nitrogen into higher-value products using renewable energy sources (Fig. 1.1).[1,2] The hydrogen generation from water electrolysis through the hydrogen evolution reaction (HER) has been one of the more studied electrochemical reactions due to the high energy density of hydrogen, which could be used for light-duty vehicles and long-distance transportation services. The capture of CO_2 from point sources such as power plants, followed by the electrochemical reduction of carbon dioxide (CO2R) into chemical feedstocks (HCOOH, C_2H_4) and fuels ($C_xH_yO_z$), could provide products currently obtained by crude oil refining without requiring massive changes to the present energy infrastructures. Furthermore, ammonia produced through electrocatalytic nitrogen reduction reaction (NRR) is another alternative fuel that contains no carbon and may be used in an engine, cracked to produce hydrogen, or used directly for fertilizer production. Although these three

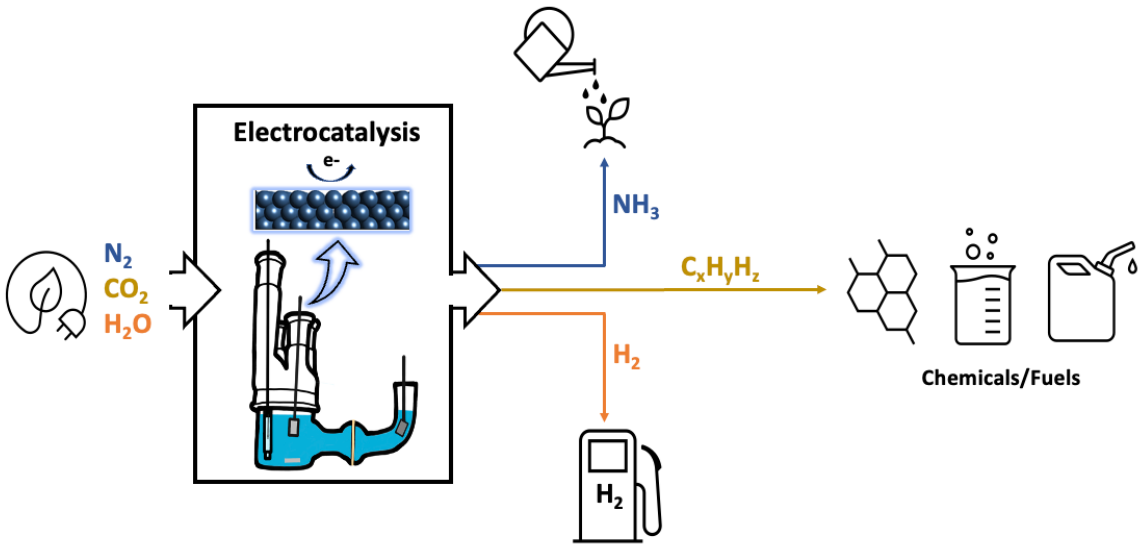

Figure 1.1. Diagram illustrating a sustainable energy landscape in which renewable energy sources are used to promote the electrocatalytic conversion of N_2, CO_2 and H_2O into value-added products.

electrochemical reactions have different technological objectives, they share the challenge of developing advanced cathodic electrocatalysts with the enhanced performance needed to enable widespread penetration of clean energy technologies.[3]

Materials with tunable compositions offer a platform to study structure-function relations that could lead to design principles for improved catalysis [4–10]. Among the highly tunable families of materials, metal chalcogenides have been particularly attractive due to their low cost, high abundance, and good electrochemical stability.[3,11,12] Metal chalcogenides have also shown to mediate various electrocatalytic conversion reactions. Among these, molybdenum dichalcogenides have shown electrocatalytic activity that is both versatile and complies with figures of merit. The surface edges of molybdenum disulfide (MoS_2) have shown to have a binding energy for hydrogen very close to the value of Pt, making them an excellent HER catalyst.[13–15] Figure 1.2a shows the presence of undercoordinated sulfur atoms at the molybdenum edges of MoS_2, which possess a metallic character and are responsible for efficiently binding H to drive HER. [16–19]

The edge sites of molybdenum diselenide ($MoSe_2$) and MoS_2 have also been shown to facilitate the binding of CO2R intermediates and are expected to overcome some of the challenges that limit the activity and selectivity of CO2R in transition metal catalysts.[20–22] Computational studies in transition metal surfaces have illustrated that CHO and COOH adsorption energies scale thermodynamically linearly with CO adsorption energy, which hinders the independent stabilization of reaction intermediates and limits the range of accessible CO2R products.[23,24] As shown in Fig. 1.2b, molybdenum dichalcogenides allow the selective binding of COOH and CHO at the uncoordinated S sites and preferential CO binding at the molybdenum edge.[22] Therefore, $MoSe_2$ and MoS_2 are expected to overcome the scaling relations that limit the activity and selectivity of CO2R in transition metal catalysts.[21] Additionally, the chemical similarity of molybdenum edge sites to the active site of nitrogenase enzymes makes them a promising point of study for NRR.[25,26] Given the electrocatalytic diversity of molybdenum chalcogenides, the systematic study of

electrocatalysts with analogous compositions, local chemical coordination, and electronic structure could unravel the discovery of earth-abundant materials that are potentially stable and active for a wide range of electrochemical reactions.

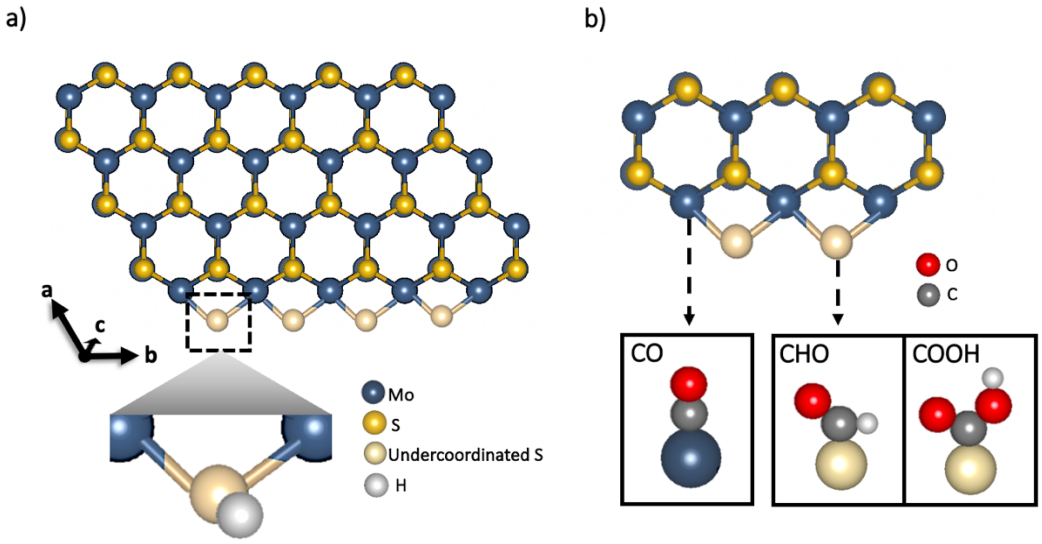

Figure 1.2. a) Top-down schematic of 2H MoS_2 depicting the catalytically active $(10\bar{1}0)$ Mo edge covered by S monomers. The undercoordinated S atoms along the $(10\bar{1}0)$ edge are responsible for efficiently binding H to drive HER. Figure adapted from ref 17 and 19. b) Binding configurations of COOH, CO, and CHO to the Mo edge of MoS_2. COOH and CHO bind to the undercoordinated S atoms, whereas CO binds to the Mo atoms. Figure adapted from ref 22.

Chevrel-Phase and Pseudo-Chevrel-Phase Molybdenum Chalcogenide Compositions Spaces:

Simple modifications to the molybdenum to chalcogen ratio of molybdenum dichalcogenides result in another tunable family of materials known as Chevrel Phases (CPs). Since their discovery in 1971,[27] CPs have attracted attention due to their superconductivity properties,[28–33] catalytic potential,[34–41] and intercalation ability which makes them promising energy conversion and storage materials.[42,43] Fig. 1.3a shows the crystal structure of CPs, which is comprised of discrete molybdenum octahedron inside a chalcogen cage with the general formula Mo_6X_8 (X=S, Se, Te). The chalcogen cage can be partially substituted by chalcogens or halogens, whereas the molybdenum octahedron can be partially or totally replaced by another transition metal, like Nb, Ta, Re, or W.

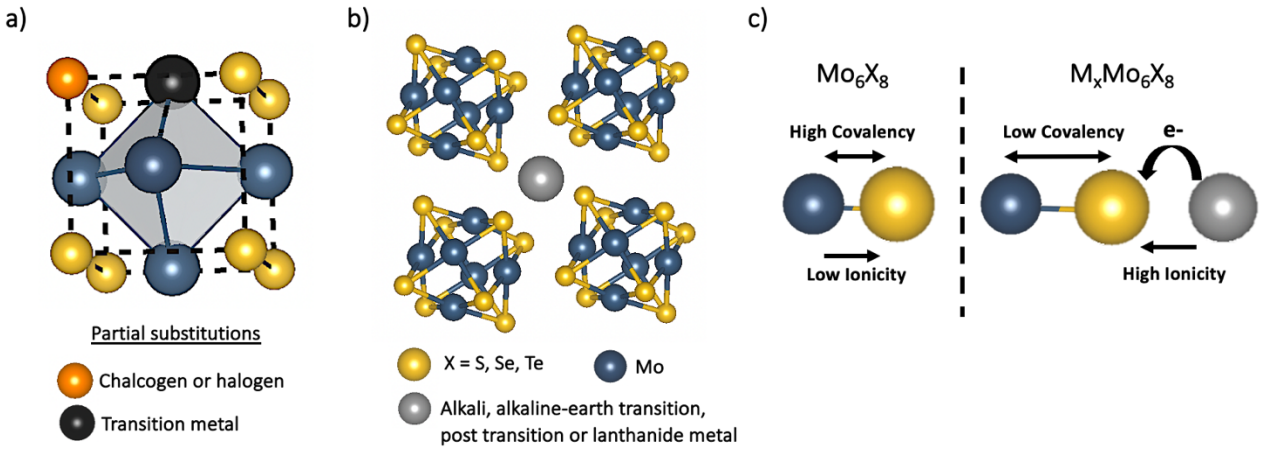

Figure 1.3. Structure of CPs depicting a) the Mo_6X_8 unit formed by a molybdenum octahedron inside a chalcogen cage and b) the extended structure illustrating the cavities in which metals can be intercalated. c) The reductive effects of M species intercalation into Mo_6X_8, which decrease the covalency of the Mo–X interactions and increase the relative charge on Mo and S to yield a net increase in ionic bonding character within the structure.

Molecular orbital calculations indicate that the stability of the Mo_6 octahedron in CPs is essentially due to twelve covalent metal-metal bonds.[44,45] This means that the formation of an undistorted Mo_6 octahedron requires 24 valance electrons. For Mo_6S_8, the electron-withdrawing nature of the chalcogen results in only twenty electrons available to populate the Mo-Mo orbitals, making the compound metastable [$(6Mo \times 6e^-) - (8S \times 2e^-) = 20\ e^-$]. Cation intercalation is a common route for stabilizing the intrinsically electron deficient Mo_6S_8 structure. As shown in Fig. 1.3b, the extended Mo_6X_8 framework forms large cavities that allow the intercalation of monovalent, divalent, or trivalent metals, with stoichiometries varying from 0 to 4. Electron donation from the intercalant to the Mo_6S_8 cluster stabilizes the electron-deficient structure and leads to the contraction of the Mo octahedra.[46,47] Thus, Mo_6S_8 can be synthesized indirectly by first making the cation-stabilized ternary phase $Cu_2Mo_6S_8$ and then leaching the cation. [43]

Previous work shows competing stabilizing and destabilizing effects from the intercalated metal that depend on the identity of cation and its stoichiometry.[46] Fig. 1.3c shows the competing ionic and covalent contributions elucidated in CP sulfides upon intercalation of 3d transition metals. Intercalating cations into the Mo_6S_8 framework increases the charge density on Mo via electron donation from the

cation.[48,49] Although the electron donation stabilizes the Mo_6 octahedron, there is a decrease in strength of the Mo–S bond, which leads to a reduction in covalency and destabilization of the CP structure. A more significant increase in ionicity is predicted as the electropositivity and stoichiometry of the intercalant increases, which will destabilize the structure.[46] Therefore, stable $M_xMo_6S_8$ compositions have an ideal ionicity component that can stabilize the Mo_6 octahedron without significantly decreasing the covalency of the Mo–S bond. The covalency between Mo-X also increases as the electron-withdrawing nature of the chalcogen decreases, making Mo_6Se_8 and Mo_6Te_8 accessible by direct high-temperature solid-state synthesis. [50,51]

Similar to their 2D metal chalcogenide analogs, CPs have shown to be active for a broad range of electrochemical resections, being oxygen reduction reaction (ORR) one of the most studied.[41,52–55] Vante et al. performed an extensive evaluation of different CP compositions for the oxygen reduction reaction (ORR) and elucidated that ORR activity increased in partially substituted CPs (i.e., $Mo_4Ru_2Se_8$) compared to binary (Mo_6X_8) and metal-intercalated CPs ($M_yMo_6X_8$). [34,38,52,56] The activity relationship seems to originate from the increase in electrons on the cluster due to the partial substitution of molybdenum which increases the electrons available at the Fermi level from 20 to 24. Binary sulfide (Mo_6S_8) and metal-intercalated CPs have also shown to promote the 6-electron electrochemical reduction of CO_2 to methanol and formate in aqueous solution.[57,58] The formate pathway was further circumvented by using CO as a reduction target, which produces only methanol in the liquid phase. Additionally, the similar structure of $Fe_2Mo_6S_8$ to FeMo nitrogenases has shown to facilitate nitrogen adsorption and conversion to ammonia with faradaic efficiencies of 12.5% in aqueous conditions.[59,60] Although there is room to explore other CP compositions for CO2R and NRR, one of the main challenges for both reactions is the competing parasitic HER, which hinders catalyst efficiency and selectivity.

An approach to increase activity and selectivity involves obtaining a deeper understanding of the absorption energies of key reactant intermediates for competing reactions. Reactant intermediates that

adsorb too strongly can poison the catalyst surface and slow reaction kinetics.[61] In contrast, reactant intermediates that bind too weakly are prone to desorb from the surface and limit the overall activity. As stated by the Sabatier principle, an ideal catalyst will have moderate adsorption energies of key reaction intermediates.[62] Therefore, modifications in the adsorption energies of important reactive species can direct the reaction toward the desired products and avoid unwanted side reactions.

The highly tunable structure of CPs allows changes in the electronic structure that can influence charge transfer and binding of intermediates at the catalyst surface. Moreover, morphology and dimensionality changes can be further induced by decreasing the chalcogen content in CPs. As shown in Fig.1.4, the decrease in chalcogen content drives the progressive fusion of molybdenum octahedra and transforms the discrete Mo_6X_8 units of CPs into continuous Mo_6X_6 units, known as Pseudo Chevrel Phases (PCPs). [63]

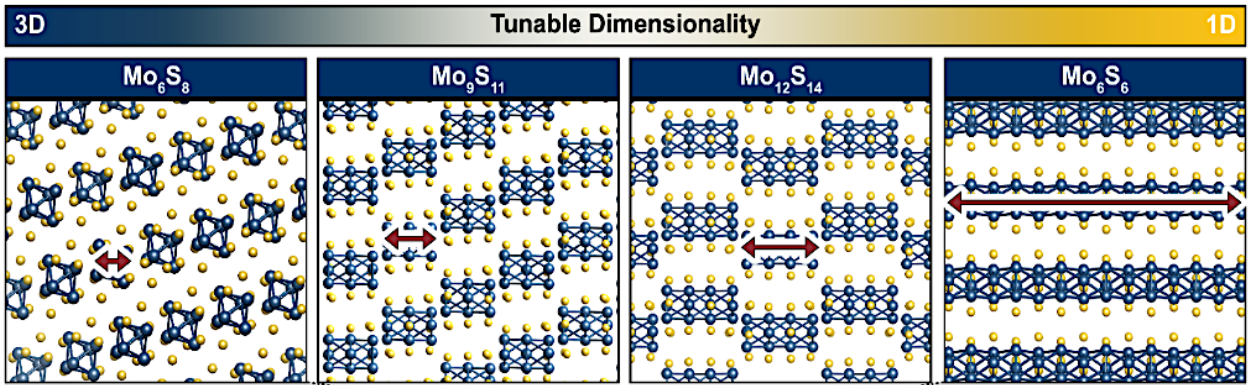

Figure 1.4. Progressive fusion of molybdenum octahedra as the chalcogen to molybdenum ratio decreases. The structure transforms from 3-dimensional CPs (Mo_6X_8) to 1-dimensional PCPs (Mo_6X_6).

The PCP structure is characterized by one-dimensional infinite $Mo_6X_6^{2-}$ (X=S, Se, Te) chains which run parallel to the hexagonal c-axis and are isolated from each other by metal ions from groups I, II, and III (Fig. 1.5). The infinite linear chains of $Mo_6X_6^{2-}$ have a large intercluster distance of ~6.40 Å in contrast to the distance of ~3.40 Å observed in CPs. The lower intercluster interaction makes the PCP structure very anisotropic [64] and facilitates solution chemistry reactions such as ion-exchange reactions and formation of

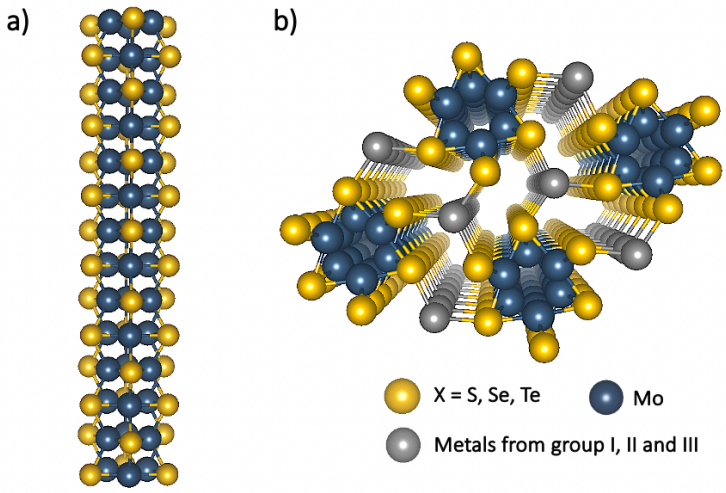

Figure 1.5. Structure of PCPs depicting a) the $Mo_6X_6^{2-}$ unit formed by infinite one-dimensional Mo_6 units inside an hexagonal chalcogen framework, and b) extended structure illustrating the cavities in which metals can be intercalated.

colloidal suspensions in highly polar solvents. [65,66] From a catalytic standpoint, one-dimensional materials have a high surface area and few crystal boundaries, which can provide channels for fast charge transport with reduced scattering. [67] Additionally, $K_2Mo_6S_6$ exhibits Mo binding sites spaced 3.2 Å apart, which is within the range in which CO_2 intermediates bind in neighboring adsorption sites to promote C-C coupling on copper.[20,68] Therefore, the geometric structural changes of CPs vs. PCPs provide diverse chemical environments at the atomic scale with composition-dependent physicochemical properties that can effectively alter reaction pathways. [69–72]

Design of catalytic materials using reactivity descriptors:

Due to the numerous thermodynamically accessible CP and PCP compositions, improved catalysts' design will benefit from identifying properties that can describe and predict catalytic performance, coined reactivity descriptors. The development of reactivity descriptors has enabled the rational design of heterogeneous catalysts and facilitated the screening of high-throughput catalysts. Such descriptors can relate the electronic properties of materials to their reactivity in catalysis (electronic descriptors), regulate

reactivity by changing the surface structure of the catalyst (structural descriptors), or combine electronic and structural properties to predict reaction trends (binary descriptors). [62]

One of the most popular reactivity descriptors is the d-band model used to describe bond formation on transition-metal surfaces.[73–76] This electronic descriptor predicts stronger bonds between the adsorbate and the metal surface when the d states are higher in energy relative to the Fermi level. Fig. 1.6a shows the filling of antibonding orbitals below the fermi level. Electrons in antibonding molecular orbitals cause the system to be destabilized since the out of phase overlap of the metal and adsorbate orbitals makes the energy associated with the binding of the adsorbate higher than the energy of the unbound atom. Therefore, increasing the energy of the d states will result in higher antibonding states, which will be less likely to be populated and thus provide a stronger binding of the adsorbate (Fig. 1.6b).

The p-band center of bulk-phase oxygen has also been used as a descriptor to predict ORR activity on perovskite cathodes.[9,77,78] For this case, decreasing the distance of the oxygen p-band center with respect to the Fermi level improves OER activity. Fig. 1.7 shows how the charge transfer gap between

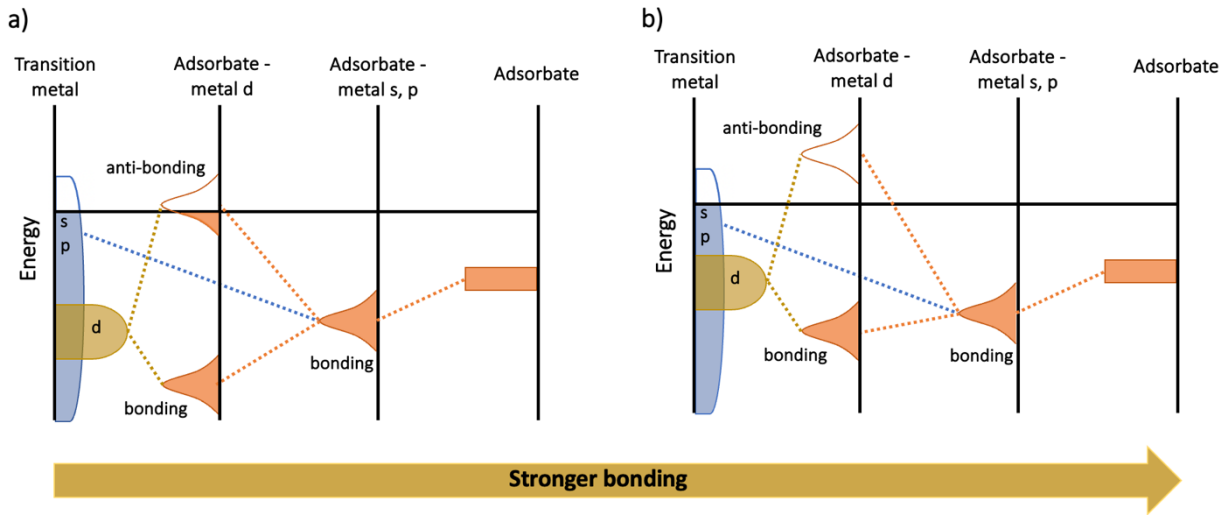

Figure 1.6. a) Schematic illustration of the d-band model showing the interaction of the adsorbate with the s, p and d states of the transition metal surface. b) The higher d states with respect to the Fermi level result in higher unoccupied anti-binding orbitals and thus stronger binding of the adsorbate to the transition metal surface. Figure adapted from ref 76.

oxygen 2p and transition metal 3d orbitals narrows by uplifting the O p-band center. The increase in covalency between oxygen and the metal stabilizes the adsorbates and reduces the charge transfer barrier. Therefore, increasing metal-oxygen covalency changes the rate-limiting step from an electron-limiting transfer process to a deprotonation-limiting process, improving reaction efficiencies.[79–81] The aforementioned descriptors are limited to specific classes of materials, either metal [62,82,83] or metal oxide surfaces.[77,84,85] Hence, there is motivation to expand to other families of materials, such as molybdenum chalcogenides, as well as develop universal reactivity descriptors.

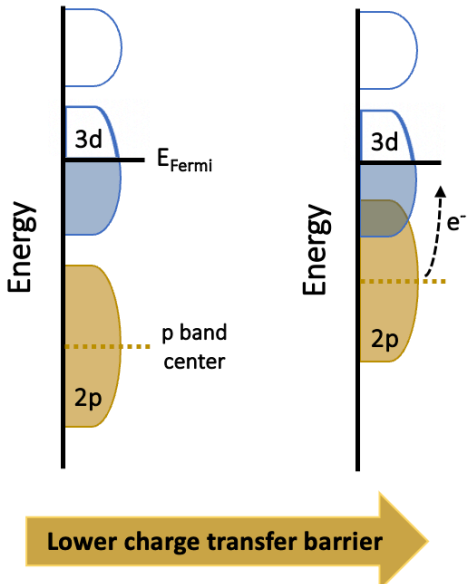

Figure 1.7. Schematic illustration of the simplified density of states of perovskites showing the transition metal 3d (blue) and O 2p (orange) bands. Improved charge transfer kinetics for OER are observed by raising the p band center with respect to the fermi level, which increases the covalency between the transition metal and oxygen. Figure adapted from ref 79,80,81.

Rapid Microwave-Assisted Solid-State Synthesis:

The systematic evaluation of electrocatalysts as a function of composition required to establish reactivity descriptors can be influenced by the feasibility and complexity of the electrocatalyst's synthetic approach. CP and PCPs have traditionally been obtained through high-temperature solid-state methods that involved mixing stoichiometric amounts of the metallic precursors, which are then sealed under vacuum and heated

in a furnace for 12+ hours to obtain a homogenous product. A novel microwave-assisted solid-state synthesis approach is used to obtain the CP and PCPs evaluated in Chapters 2 and 3 which shortens the synthesis time from days to minutes, facilitating the study of multiple CP and PCP compositions. The included methodology describes the first time a conventional microwave has been used to synthesize CP and PCP selenides and tellurides. The decrease in synthesis time observed through solid-state microwave heating originates from its energy conversion mechanism. While precursors are heated through conduction in a furnace, microwave radiation generates heat through the motion of electrons in the solid material. The electrons obtain kinetic energy from the external electric field, which is converted to thermal energy due to electron collision. This process, known as Joule heating, is given by the following formula:

$$H = I^2 \, x \, R \, x \, t \qquad \text{eq. 1.1}$$

- H is the heat produced by the conductor (J)
- I is the electrical current flowing through the conductor (A)
- R is the electrical resistance (Ω)
- t is the elapsed time (s)

As stated in eq. 1.1, the heat generated is proportional to the current squared. Given the higher electron mobility of metals compared to chalcogenides, Joule heating allows the preferential electric conduction of the metallic components of CP and PCPs, which can react very quickly with the chalcogen before it volatilizes. This heating approach facilitates the synthesis of metal chalcogenides which can be challenging due to the high volatility of chalcogens.[86] It is also believed that microwave solid-state synthesis provides more homogeneous heating since the temperature is raised simultaneously in the whole reaction volume rather than interacting through the vessel wall. Therefore, the heating profile is the inverse of conventional heating samples in which the material's surface is hotter than the interior. [87,88]

The heating mechanism of solid-state microwave synthesis can be further improved by using heat susceptors such as carbon-based solids. These materials can quickly convert electromagnetic energy to heat not only by Joule heating but also by accumulating mobile charges to the surface, known as interfacial

polarization.[89] At sharp edges, tips and submicroscopic irregularities, the surface charge density and the external electric field may reach very high values. When these charges accumulate enough kinetic energy, they will jump out of the material, resulting in the ionization of the surrounding medium.[90] This electric discharge releases thermal energy, which assists in the further heating of the microwave susceptor. Fig. 1.8 depicts the synthesis setup for the microwave-assisted solid-state synthesis discussed in Chapters 2 and 3. Graphite is used as a heat susceptor which provides temperatures above 1000C within minutes, allowing the rapid synthesis of CP and PCPs.

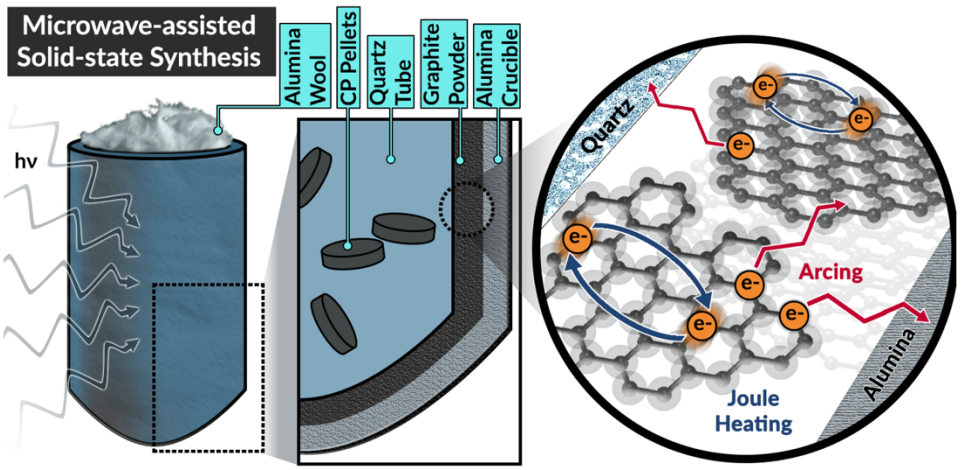

Figure 1.8. Schematic of the microwave-assisted solid-state approach used to synthesize the materials in this work. Inset captures the heating of the heat susceptor through Joule heating and electric discharge.

Thesis overview:

This thesis details the electrocatalytic evaluation of CP (Mo_6S_8, Mo_6Se_8, Mo_6Te_8) and PCP ($K_2Mo_6S_6$, $K_2Mo_6Se_6$, $K_2Mo_6Te_6$) with the aim of expanding the use of reactivity descriptors to molybdenum chalcogenides. In the interest of understanding the interactions that facilitate HER in CPs - and hence decrease the selectivity for CO_2R and NRR- the synergies that govern H adsorption (H^*) in CPs as a function of chalcogen are evaluated electrochemically under hydrogen evolution conditions (Chapter 2). It is hypothesized that changes in chalcogen electronegativity will directly impact electron localization at the molybdenum sites, directly impacting H^* interactions (Fig. 1.9). The systematic evaluation of CP

chalcogenides will elucidate the effect of electron localization on H_{ads} and provide guidelines to regulate HER. A combination of electrochemical techniques, Density functional theory (DFT), and X-ray absorption spectroscopy (XAS) are utilized to elucidate the chalcogen- H^* interactions that lead to improvements in HER activity. The study of H^* interactions is expanded to the PCP family in Chapter 3. Due to the changes in morphology and dimensionality, comparing chalcogen-H^* interactions provides an opportunity of identifying similar H^* interactions between CP and PCPs and establish structure-function relations for multiple families of molybdenum chalcogenides.

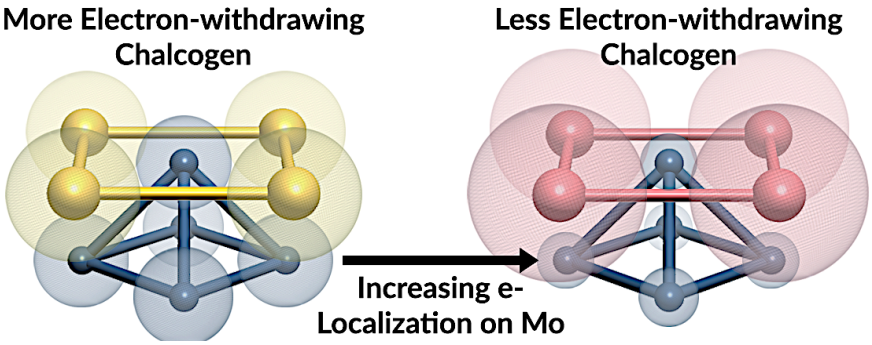

Figure 1.9. Effect of substituting sulfur for selenium in the molybdenum electron localization of CPs. The electron density of the Mo_6 octahedron can be increased by decreasing the electron withdrawing nature of the chalcogen species, thereby controlling the formal Mo_6 valence electron count.

Chapter 4 relates the results discussed in Chapters 2 and 3 with previous literature reports and work developed in the Velázquez Lab evaluating the electrocatalytic activity of CPs as electrocatalysts for HER, CO_2RR, and N_2RR. The chapter provides an overview of the factors in the electronic structure of CPs that preferentially favor interactions with reaction intermediates for HER, CO_2RR and N_2RR, as well as reactivity trends as a function of composition for each of these reactions. Current limitations in improving the catalytic activity of CPs and future directions are also mentioned. The discussion included in this thesis provides a reproducible narrative spanning synthesis, operation, and understanding of the electrocatalytic activity of CP and PCPs to the scientific community. It is intended that the results of this work and the

compendium of literature included stimulates the further study of CP and PCPs, expanding their composition design and electrocatalytic evaluation.

Reference

(1) Davis, S. J.; Lewis, N. S.; Shaner, M.; Aggarwal, S.; Arent, D.; Azevedo, I. L.; Benson, S. M.; Bradley, T.; Brouwer, J.; Chiang, Y. M.; Clack, C. T. M.; Cohen, A.; Doig, S.; Edmonds, J.; Fennell, P.; Field, C. B.; Hannegan, B.; Hodge, B. M.; Hoffert, M. I.; Ingersoll, E.; Jaramillo, P.; Lackner, K. S.; Mach, K. J.; Mastrandrea, M.; Ogden, J.; Peterson, P. F.; Sanchez, D. L.; Sperling, D.; Stagner, J.; Trancik, J. E.; Yang, C. J.; Caldeira, K. Net-Zero Emissions Energy Systems. *Science* 2018, *360* (6396), eaas9793.

(2) Seh, Z. W.; Kibsgaard, J.; Dickens, C. F.; Chorkendorff, I.; Nørskov, J. K.; Jaramillo, T. F. Combining Theory and Experiment in Electrocatalysis: Insights into Materials Design. *Science* 2017, *355* (6321), eaad4998.

(3) Giuffredi, G.; Asset, T.; Liu, Y.; Atanassov, P.; di Fonzo, F. Transition Metal Chalcogenides as a Versatile and Tunable Platform for Catalytic CO2 and N2 Electroreduction. *ACS Mater. Au* 2021, *1* (1), 6–36.

(4) Perryman, J. T.; Velázquez, J. M. Design Principles for Multinary Metal Chalcogenides: Toward Programmable Reactivity in Energy Conversion. *Chem. Mater.* 2021, *33* (18), 7133–7147.

(5) Wang, X.; Wang, C.; Ci, S.; Ma, Y.; Liu, T.; Gao, L.; Qian, P.; Ji, C.; Su, Y. Accelerating 2D MXene Catalyst Discovery for the Hydrogen Evolution Reaction by Computer-Driven Workflow and an Ensemble Learning Strategy. *J. Mater. Chem. A* 2020, *8* (44), 23488–23497.

(6) Tatarchuk, T.; Al-Najar, B.; Bououdina, M.; Aal Ahmed, M. A. Catalytic and Photocatalytic Properties of Oxide Spinels. In *Handbook of Ecomaterials*; Springer International Publishing, 2019; Vol. 3, pp 1701–1750.

(7) Zhang, Z.; Zhu, Q.; Sadakane, M.; Murayama, T.; Hiyoshi, N.; Yamamoto, A.; Hata, S.; Yoshida, H.; Ishikawa, S.; Hara, M.; Ueda, W. A Zeolitic Vanadotungstate Family with Structural Diversity and Ultrahigh Porosity for Catalysis. *Nat.Commun.* 2018, *9* (1), 3789.

(8) Löffler, T.; Meyer, H.; Savan, A.; Wilde, P.; Garzón Manjón, A.; Chen, Y. T.; Ventosa, E.; Scheu, C.; Ludwig, A.; Schuhmann, W. Discovery of a Multinary Noble Metal–Free Oxygen Reduction Catalyst. *Adv. Energy Mater.* 2018, *8* (34), 1802269.

(9) Suntivich, J.; May, K. J.; Gasteriger, H. A.; Goodenough, J. B.; Shao-Horn, Y. A Perovskite Oxide Optimized for Oxygen Evolution Catalysis from Molecular Orbital Principles. *Science (1979)* 2011, *334* (6061), 1380–1383.

(10) Reed, D. A.; Hochuli, T. J.; Gadjieva, N. A.; He, S.; Wiscons, R. A.; Bartholomew, A. K.; Champsaur, A. M.; Steigerwald, M. L.; Roy, X.; Nuckolls, C. Controlling Ligand Coordination Spheres and Cluster Fusion in Superatoms. *J. Am. Chem. Soc.* 2021, 144(1), 306-313.

(11) Tang, Z.; Yang, H. Transition Metal Chalcogenides for Energy Storage and Conversion. In *Advanced Nanomaterials for Electrochemical-Based Energy Conversion and Storage*; Ran, F., Chen, S., Eds.; Elsevier, 2019; pp 355–391.

(12) Wang, J.; Liu, J.; Zhang, B.; Ji, X.; Xu, K.; Chen, C.; Miao, L.; Jiang, J. The Mechanism of Hydrogen Adsorption on Transition Metal Dichalcogenides as Hydrogen Evolution Reaction Catalyst. *Phys. Chem. Chem. Phys.* 2017, *19* (15), 10125–10132.

(13) Chorkendorff, I.; Bonde, J.; Jorgensen, K. P.; Horch, S.; Jaramillo, T. F.; Nielsen, J. H. Identification of Active Edge Sites for Electrochemical H2 Evolution from MoS2 Nanocatalysts. *Science (1979)* 2007, *317* (5834), 100–102.

(14) Kibsgaard, J.; Chen, Z.; Reinecke, B. N.; Jaramillo, T. F. Engineering the Surface Structure of MoS 2 To Preferentially Expose Active Edge Sites For Electrocatalysis. *Nat Mater* 2012, *11* (11), 963–969.

(15) Benck, J. D.; Hellstern, T. R.; Kibsgaard, J.; Chakthranont, P.; Jaramillo, T. F. Catalyzing the Hydrogen Evolution Reaction (HER) with Molybdenumsulfide Nanomaterials. *ACS Catal* 2014, *4*, 3957–3971.

(16) Ni, B.; Wang, X. Face the Edges: Catalytic Active Sites of Nanomaterials. *Adv. Sci. 2015, 2, 1500085*.

(17) Chen, Z.; Forman, A. J.; Jaramillo, T. F. Bridging the Gap between Bulk and Nanostructured Photoelectrodes: The Impact of Surface States on the Electrocatalytic and Photoelectrochemical Properties of MoS2. *J. Phys. Chem. C* 2013, 117 (19), 9713–9722.

(18) Tsai, C.; Abild-Pedersen, F.; Nørskov, J. K. Tuning the MoS2 Edge-Site Activity for Hydrogen Evolution via Support Interactions. *Nano Lett* 2014, *14* (3), 1381–1387.

(19) Lazar, P.; Otyepka, M. Role of the Edge Properties in the Hydrogen Evolution Reaction on MoS2. *Chemistry - A European Journal* 2017, *23* (20), 4863–4869.

(20) Francis, S. A.; Velazquez, J. M.; Ferrer, I. M.; Torelli, D. A.; Guevarra, D.; McDowell, M. T.; Sun, K.; Zhou, X.; Saadi, F. H.; John, J.; Richter, M. H.; Hyler, F. P.; Papadantonakis, K. M.; Brunschwig, B. S.; Lewis, N. S. Reduction of Aqueous CO2 to 1-Propanol at MoS2 Electrodes. *Chemistry of Materials* 2018, *30* (15), 4902–4908.

(21) Hong, X.; Chan, K.; Tsai, C.; Nørskov, J. K. How Doped MoS2 Breaks Transition-Metal Scaling Relations for CO2 Electrochemical Reduction. *ACS Catal* 2016, *6* (7), 4428–4437.

(22) Chan, K.; Tsai, C.; Hansen, H. A.; Nørskov, J. K. Molybdenum Sulfides and Selenides as Possible Electrocatalysts for CO 2 Reduction. *ChemCatChem* 2014, *6* (7), 1899–1905.

(23) Peterson, A. A.; Nørskov, J. K. Activity Descriptors for CO 2 Electroreduction to Methane on Transition-Metal Catalysts *J. Phys. Chem.* 2012, *3* (2), 251–258.

(24) Shi, C.; Hansen, H. A.; Lausche, A. C.; Nørskov, J. K. Trends in Electrochemical CO2 Reduction Activity for Open and Close-Packed Metal Surfaces. *Phys. Chem. Chem. Phys.* 2014, *16* (10), 4720–4727.

(25) Zhang, Z.; Xu, X. Mechanistic Study on Enhanced Electrocatalytic Nitrogen Reduction Reaction by Mo Single Clusters Supported on MoS2. *ACS Appl Mater Interfaces* 2022, *14* (25), 28900–28910.

(26) Suryanto, B. H. R.; Wang, D.; Azofra, L. M.; Harb, M.; Cavallo, L.; Jalili, R.; Mitchell, D. R. G.; Chatti, M.; MacFarlane, D. R. MoS 2 Polymorphic Engineering Enhances Selectivity in the Electrochemical Reduction of Nitrogen to Ammonia. *ACS Energy Lett* 2019, *4* (2), 430–435.

(27) Chevrel, R.; Sergent, M.; Prigent, J. Sur de Nouvelles Phases Sulfurées Ternaires Du Molybdène. *J Solid State Chem* 1971, *3* (4), 515–519.

(28) Umarji, A. M.; Rao, G. V. S.; Janswadkar, M. P.; Radhakrishnan, T. S. Structure and Superconductivity of Pb1-XAxMo6S8 (A=Ag,In,Bi) Chevrel Phases. *Solid State Commun.* 1980, *37*, 1–5.

(29) Sergent, M.; Chevrel, R.; Rossel, C. On the Superconductivity of PbMo6S8 and the Series MxPbMo6S8 and MxPb1-XMo6S8. *J Less Common Met* 1978, *58*, 179–193.

(30) Peña, O. Chevrel Phases: Past, Present and Future. *Phys. C: Supercond. Appl.* 2015, *514*, 95–112.

(31) Lin, F.; Fang, Y.; Che, X.; Zhang, S.; Huang, F. Superconductivity in the Electron-Doped Chevrel Phase Compound Mo6S6.8Te1.2. *Inorg. Chem* 2020, *59* (10), 6785–6789.

(32) Chevrel, R.; Hirrien, M.; Sergent, M. Superconducting Chevrel Phases: Prospects and Perspectives. *Polyhedron* 1986, *5* (1–2), 87–94.

(33) Fischer. Chevrel Phases: Superconducting and Normal State Properties. *Applied Physics* 1978, *16* (1), 1–28.

(34) Strachan, J.; Masters, A. F.; Maschmeyer, T. The Catalytic Nature of Chevrel Phases (MxMo6S8) in Review. *Mater Res Bull* 2021, *139*, 111286.

(35) Peña, O. Chevrel Phases: Past, Present and Future. *Phys. C: Supercond. Appl.* 2015, *514*, 95–112.

(36) Ortiz-Rodríguez, J. C.; Velázquez, J. M. Structure–Reactivity Relationships in Chevrel Phase Electrocatalysts for Small-Molecule Reduction Reactions. *Curr Opin Electrochem* 2022, *34*, 101002.

(37) Schubert B; Tributsch H. Single-Metal Catalytic Centers for Hydrogen Evolution. *J. Electrochem. Soc* 1993, *140*, 98–103.

(38) Alonso-Vat, C. N.; Schubert, B.; Tributsch, H. Transition Metal Cluster Materials for Multi-Electron Transfer. *Mater. Chem. Phys.* 1989, *22*, 281–307.

(39) Alonso-Vante, N.; Shubert, B; Tributsch, H.; Perrin, A. Influence of D-State Density and Chemistry of Transition Metal Cluster Selenides on Electrocatalysis. *J Catal* 1988, *112*, 384–391.

(40) Tributsch, H.; Pohlmann Ludwing. Electron Transfer: Classical Approaches and New Frontiers. *Science* 1998, *279*, 1891–1895.

(41) Jaegermann, W.; Pettenkofer, C.; Alonso Vante, N.; Schwarzlose, Th.; Tributsch, H. Chevrel Phase Type Compounds: Electronic, Chemical and Structural Factors in Oxygen Reduction Electrocatalysis. *Ber. Bunsenges. Phys. Chem.* 1990, *94* (4), 513–520.

(42) Aurbach, D.; Lu, Z.; Schechter, A.; Gofer, Y.; Gizbar, H.; Turgeman, R.; Cohen, Y.; Moshkovich, M.; Levi, E. Prototype Systems for Rechargeable Magnesium Batteries. *Nature* 2000, *407*, 13–16.

(43) Lancry, E.; Levi, E.; Gofer, Y.; Levi, M.; Salitra, G.; Aurbach, D. Leaching Chemistry and the Performance of the Mo6S8 Cathodes in Rechargeable Mg Batteries. *Chemistry of Materials* 2004, *16* (14), 2832–2838.

(44) Chevrel, R.; Gougeon, P.; Potel, M.; Sergent, M. Ternary Molybdenum Chalcogenides: A Route to New Extended Clusters. *J. Solid State Chem.* 1985, *57*, 25–33.

(45) Timothy Hughbanks; Roald Hoffmann. Molybdenum Chalcogenides: Clusters, Chains, and Extended Solids. The Approach to Bonding in Three Dimensions. *J Am Chem Soc* 1983, *105* (5), 1150–1162.

(46) Lilova, K.; Perryman, J. T.; Singstock, N. R.; Abramchuk, M.; Subramani, T.; Lam, A.; Yoo, R.; Ortiz-Rodríguez, J. C.; Musgrave, C. B.; Navrotsky, A.; Velázquez, J. M. A Synergistic Approach to Unraveling the Thermodynamic Stability of Binary and Ternary Chevrel Phase Sulfides. *Chem. Mater.* 2020, *32* (16), 7044–7051.

(47) Levi, E.; Aurbach, D. Chevrel Phases, MxMo6T8 (M = Metals, T = S, Se, Te) as a Structural Chameleon: Changes in the Rhombohedral Framework and Triclinic Distortion. *Chem. Mater.* 2010, *22* (12), 3678–3692.

(48) Yvon K; Paoli A. Charge Transfer and Valence Electron Concentration in Chevrel Phases. *Solid State Commun.* 1977, *24*, 41–45.

(49) Hyler, F. P.; Wuille Bille, B. A.; Ortíz-Rodríguez, J. C.; Sanz-Matias, A.; Roychoudhury, S.; Perryman, J. T.; Patridge, C. J.; Singstock, N. R.; Musgrave, C. B.; Prendergast, D.; Velázquez, J. M. X-Ray Absorption Spectroscopy Insights on the Structure Anisotropy and Charge Transfer in Chevrel Phase Chalcogenides. *Physical Chemistry Chemical Physics* 2022, *24* (28), 17289–17294.

(50) Andersen, O. K.; Klose, W.; Nohl, H. Electronic Structure of Chevrel-Phase High-Critical-Field Superconductors. *Phys. Rev. B* 1978, *17* (3), 1209–1237.

(51) Bullett, D. W. Relation between Electronic Structure and Tc in Binary and Ternary Molybdenum Chalcogenides. *Phys Rev Lett* 1977, *39* (10), 664–666.

(52) Alonso-Vante, N. Chevrel Phases and Chalcogenides. In *Handbook of fuel cells: fundamentals, technology, and applications*; John Wiley & Sons, 2003; Vol. 2, pp 534–543.

(53) Zhang, L.; Zhang, J.; Wilkinson, D. P.; Wang, H. Progress in Preparation of Non-Noble Electrocatalysts for PEM Fuel Cell Reactions. *J. Power Sources* 2006, *156* (2), 171–182.

(54) Lee, J. W.; Popov, B. N. Ruthenium-Based Electrocatalysts for Oxygen Reduction Reaction-a Review. *J. Solid State Electrochem.* 2007, *11* (10), 1355–1364.

(55) Mora-Hernández, J.; Luo, Y.; Alonso-Vante, N.; Mora-Hernández, J. M. What Can We Learn in Electrocatalysis, from Nanoparticulated Precious and/or Non-Precious Catalytic Centers Interacting with Their Support? *Catalysts* 2016, *6* (145), 1–55.

(56) Schubert, B.; Alonso-Vante N.; Gocke, E.; Tributsch, H. Oxygen Reduction Electrocatalysis by Chevrel Phase Sulfides Supported on Carbon Paste Electrodes. *Phys. Chem.* 1988, *92*, 1279–1283.

(57) Perryman, J. T.; Ortiz-Rodrıguez, J. C.; Jude, J. W.; Hyler, F. P.; Davis, R. C.; Mehta, A.; Kulkarni, A. R. Metal-Promoted Mo6S8 Clusters: A Platform for Probing Ensemble Effects on the Electrochemical Conversion of CO2 and CO to Methanol. *Mater Horiz* 2020, *7*, 193–202.

(58) Liu, P.; Choi, Y.; Yang, Y.; White, M. G. Methanol Synthesis from H2 and CO2 on a Mo6S8 Cluster: A Density Functional Study. *J. Phys. Chem. A*. 2010, *114* (11), 3888–3895.

(59) Lu, K.; Xia, F.; Li, B.; Liu, Y.; Abdul Razak, I. B.; Gao, S.; Kaelin, J.; Brown, D. E.; Cheng, Y. Synergistic Multisites Fe2Mo6S8 Electrocatalysts for Ambient Nitrogen Conversion to Ammonia. *ACS Nano* 2021, *15* (10), 16887–16895.

(60) Singstock, N. R.; Musgrave, C. B. How the Bioinspired Fe2Mo6S8Chevrel Breaks Electrocatalytic Nitrogen Reduction Scaling Relations. *J Am Chem Soc* 2022, *144* (28), 12800–12806.

(61) Ooka, H.; Huang, J.; Exner, K. S. The Sabatier Principle in Electrocatalysis: Basics, Limitations, and Extensions. *Front. Energy Res.* 2021, *9*, 654460.

(62) Zhao, Z. J.; Liu, S.; Zha, S.; Cheng, D.; Studt, F.; Henkelman, G.; Gong, J. Theory-Guided Design of Catalytic Materials Using Scaling Relationships and Reactivity Descriptors. *Nat. Rev. Mater.* 2019, *4* (12), 792–804.

(63) King, R. B. Chemical Bonding Topology of Superconductors. I. Ternary Molybdenum Chalcogenides (Chevrel Phases). *J Solid State Chem* 1987, *71* (1), 224–232.

(64) Hughbanks, T.; Hoffmann, R. Molybdenum Chalcogenides Clusters, Chains, and Extended Solids. The Approach to Bonding in Three Dimensions. *J. Am. Chem. Soc.* 1983, *105*, 1150–1162.

(65) Tarascon, J. M.; DiSalvo, F. J.; Chen, C. H.; Carroll, P. J.; Walsh, M.; Rupp, L. First Example of Monodispersed (Mo3Se3)1∞ Clusters. *J Solid State Chem* 1985, *58* (3), 290–300.

(66) Dronskowskit, R.; Hoffmann, R. Bond Reactivities, Acidities, and Basicities within AMo3X3 Phases (A = Li, Na, K, In; X = Se, Te). *Inorg. Chem* 1992, *31*, 3107–3113.

(67) Li, J.; Zheng, G. One-Dimensional Earth-Abundant Nanomaterials for Water-Splitting Electrocatalysts. *Adv. Sci. 2017,*2017, *4* (3), 1600380.

(68) Zheng, Y.; Vasileff, A.; Zhou, X.; Jiao, Y.; Jaroniec, M.; Qiao, S. Z. Understanding the Roadmap for Electrochemical Reduction of CO2 to Multi-Carbon Oxygenates and Hydrocarbons on Copper-Based Catalysts. *J Am Chem Soc* 2019, *141* (19), 7646–7659.

(69) Pérez-Ramírez, J.; López, N. Strategies to Break Linear Scaling Relationships. *Nat. Catal.* 2019, *2* (11), 971–976.

(70) He, J.; Johnson, N. J. J.; Huang, A.; Berlinguette, C. P. Electrocatalytic Alloys for CO2 Reduction. *ChemSusChem* 2018, *11* (1), 48–57.

(71) Lee, C. W.; Yang, K. D.; Nam, D. H.; Jang, J. H.; Cho, N. H.; Im, S. W.; Nam, K. T. Defining a Materials Database for the Design of Copper Binary Alloy Catalysts for Electrochemical CO2 Conversion. *Adv. Mater.* 2018, *30*, 1704717.

(72) Hill, C. M.; Mendoza-Cortes, J. L.; Velazquez, J. M.; Whittaker-Brooks, L. Multi-Dimensional Designer Catalysts for Negative emissions Science (NES): Bridging the Gap Between synthesis, Simulations, and Analysis. *iScience* 2020, *23* (6), 101152.

(73) Nørskov, J. K.; Abild-Pedersen, F.; Studt, F.; Bligaard, T. Density Functional Theory in Surface Chemistry and Catalysis. *Proc. Natl. Acad. Sci.* 2011, *108* (3), 937–943.

(74) Hammer, B.; Norskov, J. B. K. Electronic Factors Determining the Reactivity of Metal Surfaces. *Surf. Sci.* 1995, *343*, 211–220.

(75) Hammer, B.; Nørskov, J. K. Theoretical Surface Science and Catalysis-Calculations and Concepts. *Adv. Catal.* 2000, *45*, 71–129.

(76) Li, M.; Garg, S.; Chang, X.; Ge, L.; Li, L.; Konarova, M.; Rufford, T. E.; Rudolph, V.; Wang, G. Toward Excellence of Transition Metal-Based Catalysts for CO2 Electrochemical Reduction: An Overview of Strategies and Rationales. *Small Methods* 2020, *4* (7), 200033.

(77) Lee, Y. L.; Kleis, J.; Rossmeisl, J.; Yang, S. H.; Morgan, D. Prediction of Solid Oxide Fuel Cell Cathode Activity with First-Principles Descriptors. *Energy Environ. Sci.* 2011, *4* (10), 3966–3970.

(78) Hong, W. T.; Stoerzinger, K. A.; Lee, Y. L.; Giordano, L.; Grimaud, A.; Johnson, A. M.; Hwang, J.; Crumlin, E. J.; Yang, W.; Shao-Horn, Y. Charge-Transfer-Energy-Dependent Oxygen Evolution Reaction Mechanisms for Perovskite Oxides. *Energy Environ. Sci.* 2017, *10* (10), 2190–2200.

(79) Hong, W. T.; Risch, M.; Stoerzinger, K. A.; Grimaud, A.; Suntivich, J.; Shao-Horn, Y. Toward the Rational Design of Non-Precious Transition Metal Oxides for Oxygen Electrocatalysis. *Energy Environ. Sci.* 2015, *8*, 1404-1427.

(80) Hong, W. T.; Stoerzinger, K. A.; Lee, Y. L.; Giordano, L.; Grimaud, A.; Johnson, A. M.; Hwang, J.; Crumlin, E. J.; Yang, W.; Shao-Horn, Y. Charge-Transfer-Energy-Dependent Oxygen Evolution Reaction Mechanisms for Perovskite Oxides. *Energy Environ. Sci.* 2017, *10* (10), 2190–2200.

(81) Grimaud, A.; May, K. J.; Carlton, C. E.; Lee, Y. L.; Risch, M.; Hong, W. T.; Zhou, J.; Shao-Horn, Y. Double Perovskites as a Family of Highly Active Catalysts for Oxygen Evolution in Alkaline Solution. *Nat Commun* 2013, *4*, 2439.

(82) Nørskov, J. K.; Abild-Pedersen, F.; Studt, F.; Bligaard, T. Density Functional Theory in Surface Chemistry and Catalysis. *Proc Natl Acad Sci USA* 2011, *108* (3), 937–943.

(83) Bhattacharjee, S.; Waghmare, U. v.; Lee, S. C. An Improved D-Band Model of the Catalytic Activity of Magnetic Transition Metal Surfaces. *Sci Rep* 2016, *6,* 35916.

(84) Jacobs, R.; Hwang, J.; Shao-Horn, Y.; Morgan, D. Assessing Correlations of Perovskite Catalytic Performance with Electronic Structure Descriptors. *Chem. Mater* 2019, *31* (3), 785–797.

(85) Hwang, J.; Rao, R. R.; Giordano, L.; Katayama, Y.; Yu, Y.; Shao-Horn, Y. Perovskites in Catalysis and Electrocatalysis. *Science* 2017, *358* (6364), 751-756.

(86) Whittaker, A. G.; Mingos, D. M. P. Microwave-Assisted Solid-State Reactions Involving Metal Powders. *J. Chem. Soc., Dalton Trans*. 1992, *18*, 2751–2752.

(87) Schanche, J. S. Microwave Synthesis Solutions from Personal Chemistry. *Mol Divers* 2003, *7* (2–4), 293–300.

(88) Kitchen, H. J.; Vallance, S. R.; Kennedy, J. L.; Tapia-Ruiz, N.; Carassiti, L.; Harrison, A.; Whittaker, A. G.; Drysdale, T. D.; Kingman, S. W.; Gregory, D. H. Modern Microwave Methods in Solid-State Inorganic Materials Chemistry: From Fundamentals to Manufacturing. *Chem Rev* 2014, *114* (2), 1170–1206.

(89) Kim, T.; Lee, J.; Lee, K. H. Microwave Heating of Carbon-Based Solid Materials. *Carbon Letters* 2014, *15* (1), 15–24.

(90) Sun, J.; Wang, W.; Yue, Q. Review on Microwave-Matter Interaction Fundamentals and Efficient Microwave-Associated Heating Strategies. *Materials* 2016, *9*, 231.

Chapter 2: Stabilizing Hydrogen Adsorption through Theory-Guided Chalcogen Substitution in Chevrel-Phase Mo_6X_8 (X=S, Se, Te) Electrocatalysts

Abstract

In this work, we implement a facile microwave-assisted synthesis method to yield three binary Chevrel-Phase chalcogenides (Mo_6X_8; X = S, Se, Te) and investigate the effect of increasing chalcogen electronegativity on hydrogen evolution catalytic activity. Density functional theory predictions indicate that increasing chalcogen electronegativity in these materials will yield a favorable electronic structure for proton reduction. This is confirmed experimentally via X-ray absorption spectroscopy as well as traditional electrochemical analysis. We have identified that increasing the electronegativity of X in Mo_6X_8 increases the hydrogen adsorption strength owing to a favorable shift in the p-band position as well as an increase in the Lewis basicity of the chalcogen, thereby improving hydrogen evolution reaction energetics. We find that Mo_6S_8 exhibits the highest hydrogen evolution activity of the Mo_6X_8 series of catalysts, requiring an overpotential of 321 mV to achieve a current density of 10 mA cm^{-2}_{ECSA}, a Tafel slope of 74 mV per decade, and an exchange current density of 6.01×10^{-4} mA cm^{-2}_{ECSA}. Agreement between theory and experiment in this work indicates that the compositionally tunable Chevrel-Phase chalcogenide family is a promising framework for which electronic structure can be predictably modified to improve catalytic small-molecule reduction reactivity.

Introduction

Renewable hydrogen production has become an attractive alternative to transition away from fossil fuels and reduce carbon dioxide emissions.[1] In addition to its high gravimetric energy density as well as the environment-friendliness of its combustion product, hydrogen is attractive due to its role in industrial processes such as ammonia synthesis, hydrogenation reactions, crude oil refining, and biogas processing.[2–

[4] Currently, hydrogen gas is predominantly generated via steam methane reforming, which leads to substantial anthropogenic CO_2 emission.[5] Alternatively, hydrogen can be generated via electrochemical water splitting—a process that leaves virtually no carbon footprint when coupled to renewable sources of electricity such as wind and solar energy.[2,6] This electrochemical process occurs according to the half-reaction:

$$2H^+ + 2e^- \rightleftharpoons H_2 \qquad (1)$$

Following Sabatier's principle for heterogeneous catalysis, the Gibbs free energy for hydrogen adsorption of a maximally efficient HER catalyst will be thermoneutral ($\Delta G_H \approx 0$). While Pt is currently championed as the most efficient HER catalyst owing to its nearly thermoneutral H adsorption, scalability of systems based upon noble metals is hindered by high production costs engendered by elemental scarcity.[7,8] Many cases in nature (e.g. hydrogenase and nitrogenase enzymes) have succeeded in achieving favorable ΔG_H with Earth-abundant catalyst compositions that often include non- precious transition metal chalcogenides with Fe, Ni, and Mo at their active sites.[9,10] These revelations highlighted the promise of inorganic analogs such as MoS_2, where H adsorption at edge sites indeed approach the ΔG_H of Pt. [11,12] This observation is consistent with the popular d-band center model which suggests that HER reactivity correlates with the density of transition metal d states near the Fermi level of the catalyst.[13] Recent advances have identified a range of transition metal dichalcogenides such as WS_2,[14,15] FeS_2,[16,17] CoS_2,[18,19] WSe_2,[20] $MoSe_2$,[20–22] $CoSe_2$,[23,24] and $CoTe_2$[25,26] as active catalysts for HER. It is believed that the HER activity of this family of compounds relies on the negatively polarized chalcogenide anions, which results in lower free energy barriers for proton adsorption.[27] To investigate the effect of electronic structure and active-site coordination on chemically analogous Earth-abundant catalysts, we examined Chevrel-Phase (CP) chalcogenides with the generic formula $M_yMo_6X_8$ (M =alkali, alkaline, transition or post-transition metals, y = 0-4; X = S, Se, Te); specifically focusing on the binary Mo_6X_8. This chalcogenide family is especially attractive due to its interconnected cluster framework (Fig. 2.1) and its tunable composition that affords

fine control over the electronic structure, which has led to previously observed catalytic activity for hydrodesulfurization,[28–30] oxygen reduction,[31–35] and CO_2 reduction reactions.[36]

Metal intercalated CP frameworks have been shown to be stable and relatively active HER catalysts over a range of operating conditions[31,37–39] however, the effect of chalcogen composition on HER reactivity in CPs is not well understood. We hypothesized that the electronegative chalcogenide surface sites would bond with adsorbed hydrogen, and that varying the chalcogen identity would directly affect the strength of this bond, as well as shifting the position of the Mo d-states relative to the Fermi level. Density Functional Theory (DFT) calculations support this hypothesis and provide additional insight into the contributions of both the local coordination environment and the bulk electronic structure to H adsorption and suggest that the p-band center provides a useful descriptor for bond strength. To confirm the results of DFT calculations, we implemented a time- and energy-efficient synthetic method to yield all three binary CP chalcogenide compositions. Predicted changes to CP electronic structure were confirmed experimentally via X-Ray Absorption Spectroscopy (XAS) and were correlated to changes in catalytic HER reactivity under acidic operating conditions. The results presented herein offer insights into the tunability of electrocatalytic reactivity exhibited by CP chalcogenides, and our integrated theoretical and experimental effort represents a promising route toward rational and iterative material design driven by reliable computational prediction.

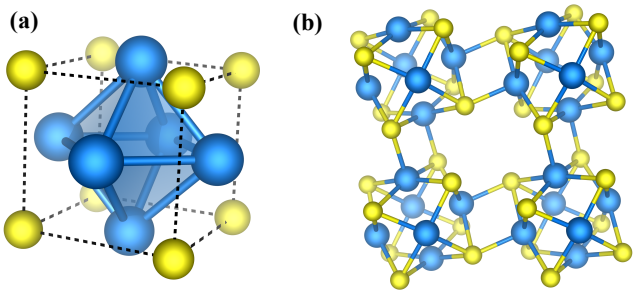

Figure 2.1. Structure of the binary CP chalcogenides depicting (a) the Mo_6X_8 unit cell with the metallic Mo-Mo bonds of the octahedra shown within the chalcogenide cage, as indicated by the dashed lines, and (b) four Mo_6X_8 units illustrating the ionic Mo-X bonds within and between the clusters, and the large cavities formed between clusters.

Experimental Section

Chemicals and Materials

MoS_2 powder (99%, ∼325 mesh), Cu powder (99.995%, ~100 mesh), $MoSe_2$ powder (99.999%, ~200 mesh) and Pt mesh (99.99%) were used as purchased from Alfa Aesar. Mo powder (99.99%, ∼100 mesh), Te powder (99.8%, ~200 mesh) and concentrated H_2SO_4 acid (ACS grade) were used as purchased from Sigma Aldrich. Fused quartz tubes (2 mm thick) were purchased from AdValue Technology and made into round-bottom tubes with an in-house oxy-hydrogen torch. Ultra-high purity grade H_2 (99.999%) was used as purchased from Praxair Direct. Toray Carbon Paper (060 with Micro Porous Layer) and 20% Pt/C on Vulcan Carbon Cloth were purchased from Fuel Cell Store. Ag/AgCl reference electrodes were purchased through ALS Japan. Selemion® anion exchange membrane was purchased from AGC Engineering and stored in ultra-pure deionized water prior to use in electrochemical experiments.

Catalyst Synthesis

CP chalcogenides studied here were synthesized using a high-temperature heating method described in detail in our previous work.[36,40] Briefly, appropriate precursor powders were mixed via ball-milling and pressed into pellets, transferred into quartz tubes under N_2 under tightly packed Al_2O_3 microfiber, then submerged in a bath of ∼325 mesh graphite powder in a conventional microwave oven under Ar where the samples were irradiated for multiple minutes at a power of up to 1000 W. As the electronegativity of the chalcogen decreases the number of electrons per Mo_6 cluster increases up to a limit of 24 electrons for a completely filled valence shell.[41] The increase in valence electron count when less electronegative chalcogens are incorporated leads to an increase in cluster stability and decreases the heating time required to obtain phase-pure CPs. This is particularly important for Mo_6S_8, where—owing to the electron-withdrawing strength of S—the Mo_6 octahedron is slightly electron-deficient at $20e^-$, making the cluster metastable and prone to decomposition under the high-temperature conditions of this synthetic method.

To mitigate the destabilizing effects of this electron deficiency, a metallic Cu precursor was included to stabilize the Mo_6 octahedron in a $Cu_2Mo_6S_8$ framework. The heating time required to produce Mo_6Te_8, Mo_6Se_8 and $Cu_2Mo_6S_8$ varied from 5, 8 and 10 mins, respectively. To obtain de-intercalated Mo_6S_8, Cu was chemically etched in O_2-bubbled 6.0 M HCl according to literature methods.[42]

Structural and Electronic Characterization

The phase purity of CPs was analyzed via Powder X-ray Diffraction (PXRD) using a Bruker D8 Advance diffractometer with Cu K-alpha radiation (1.541 Å). Catalyst morphology and bulk composition were analyzed before and after electrolysis using a FEI (Hillsboro, OR) 430 Nano Scanning Electron Microscope (SEM) and a FEI Scios Dual-Beam SEM with an Oxford Energy Dispersive X-ray (EDX) detector, respectively. Surface composition analysis before and after electrolysis was completed using a PHI Versaprobe 3 X-ray Photoelectron Spectrometer (XPS).

X-ray Absorption Spectroscopy and Data Analysis

CP chalcogenides were all scanned at their respective Mo L_3-edge. All XAS scans were taken at the Stanford Synchrotron Radiation Lightsource (SSRL) at the SLAC National Accelerator Laboratory. Mo_6Se_8 scans were taken at beamline 14-3, while Mo_6S_8 and Mo_6Te_8 scans were performed at beamline 4-3. All edge scans were performed under He with a chamber O_2 content <0.04% in order to minimize interactions between tender X-rays and the gas inside the sample chamber. Energy calibration of the beam was performed using elemental Mo foil. For each sample, fluorescence data were collected using a Lytle detector over the course of three scans which were averaged together to improve the signal-to-noise ratio.

Electrochemical Characterization

Electrochemical measurements were performed in a custom three-electrode H-shaped cell (Fig. S2.1) where the working electrode and counter electrode compartments were separated by an anion-exchange

membrane. Working electrodes were fabricated using powder-based inks for each catalyst prepared using 3.0 mL isopropanol, 50 µL polytetrafluoroethylene (PTFE) suspension, 5 mg of carbon black and 6.01×10^{-5} moles of each respective catalyst. The PTFE serves as a binding agent while the carbon black increases conductivity. The PTFE/carbon black mixture facilitates the transport of the evolving hydrogen from the reaction site through hydrophobic pores and provides robust mechanical properties to the electrode.[43,44] Inks were sonicated for 20 mins and then drop cast onto conductive carbon paper (Fig. S2.2). The working (CP), reference (Ag/AgCl), and counter (Pt mesh) electrodes were submerged in 0.5 M H_2SO_4 electrolyte that was purged with H_2 gas for 30 mins to remove any dissolved O_2. All electrochemical experiments were performed using a Bio-Logic VSP-300 multichannel potentiostat with potentials converted to RHE scale using the following equation:

$$E_{RHE} = E(Ag/AgCl) + 0.210 + 0.059 \times pH \qquad (2)$$

Hydrogen evolution activity was evaluated via Linear Sweep Voltammetry (LSV) at a scan rate of 5 mVs^{-1}. During these experiments, a H_2 flow was maintained over the electrolyte and the electrolyte was stirred at 1200 rpm to remove hydrogen gas bubbles from the working electrode surface and maintain consistent local pH. Catalyst stability was observed in two different experiments for each catalyst: 1) Chronopotentiometry experiments where a specific current density was maintained over time while observing changes in overpotential, and 2) LSV experiments performed both before and after 500 and 1000 cyclic voltammograms. Electrochemically Active Surface Area (ECSA) for each electrode was determined by measuring their double-layer capacitance (C_{dl}), where cyclic voltammograms (CV's) were acquired at various scan rates in a non-Faradaic region where observable current could be attributed strictly to capacitive charging. [45] The current at a chosen potential near open circuit in these CV's was plotted as a function of scan rate and the slope of this graph gives C_{dl}. Figs. S2.3 and S2.4 show the representative CV's and linear plots used to calculate C_{dl}. The intrinsic C_{dl} of each catalyst was taken as the difference of the C_{dl}

of the electrode (PTFE/carbon black/catalyst) and the C_{dl} of the blank (PTFE/carbon black). The ECSA was then calculated by dividing C_{dl} by the specific capacitance (C_s) of the sample

$$ECSA = \frac{C_{DL}}{C_S} \quad (3)$$

where a specific capacitance of 60 μFcm^{-2} was chosen based on the reported capacitance for a flat MoS_2 sample in 0.5 M H_2SO_4.[46] Charge-transfer resistance was measured via Electrochemical Impedance Spectroscopy (EIS) at -0.27 V vs. RHE with a superimposed AC bias oscillating at frequencies from 1 MHz to 1 Hz with a 10 mV sinus amplitude.

Computational Methods and Models

DFT calculations were performed using the Vienna Ab initio Simulation Package (VASP).[47] The Revised Perdew-Burke-Ernzerhof (RPBE)[48] generalized gradient approximation exchange-correlation functional was used to compute structures and zero-point energies, while the Strongly Constrained and Appropriately Normed (SCAN) semilocal density functional[49] was used to compute enthalpies, charge densities and densities of states (DOS). All calculations were performed with a plane-wave cutoff of 520 eV and a Γ-centered Monkhorst-Pack k-point grid with a density of $1000/\mathrm{N}$ where N is the number of atoms in the unit cell. All calculations were performed using the implicit water solvation model as implemented in VASPsol.[50] Zero-point energies were calculated using the dynamical matrix approach within Henkelman's VTST Tools package. Charge densities were calculated using DDEC6 atomic population analysis.[51]

Adsorption energies at 298.15 K are calculated using:

$$\Delta G_{ads} = \Delta H_{ads} + \Delta E_{ZPE} - T\Delta S_{ads} \quad (4)$$

Adsorption enthalpies are calculated with:

$$\Delta H_{ads} = H_{ads} - H_{surf} - 1/2H_{H_2} \quad (5)$$

Where H_{ads}, H_{surf}, and H_{H_2} are the computed total enthalpies of the surface with an adsorbate, the bare surface, and H_2, respectively. The change in zero-point energy is calculated using:

$$\Delta E_{ZPE} = E_{ZPE,H^*} - \frac{1}{2}E_{ZPE,H_2} \quad (6)$$

where E_{ZPE,H^*} is the zero-point energy of adsorbed hydrogen (H*) and E_{ZPE,H_2} is the experimental zero-point energy of H_2 (0.27 eV).[52] We make the approximation that

$$T\Delta S_{ads} \approx -\frac{1}{2}S_{H_2 std} \text{ at } 298.15 \text{ K} \quad (7)$$

because the vibrational entropy of H* is negligibly small relative to hydrogen in solution.[53] $S_{H_2 std} = 0.4038$ eV is obtained from the National Institute of Standards and Technology Joint Army–Navy–Air Force (NIST JANAF) thermochemical database.[54] Periodic slab models of the surfaces included a 1 × 1 × 2 supercell model of the Mo_6X_8 surface and a 2 × 2 × 3 supercell model of the (111) Pt surface due to its smaller unit cell size to reduce adsorbate-adsorbate interactions. All models for adsorption on Mo_6X_8 include one H* per supercell due to the unfavorable adsorption of H* on these materials. Additionally, these calculations included one H_2O adsorbed at the Mo surface site due to the favorable adsorption of H_2O on these surfaces. The Pt surface was modeled at ¼, ½, ¾ and full surface coverages of H*. Slab calculations included 20 Å of solvent above the slab in the z-direction to avoid interactions between periodic images.

Results and Discussion

Microwave-Assisted Solid-State Synthesis

Polycrystalline Mo_6S_8, Mo_6Se_8, and Mo_6Te_8 were all synthesized with high phase-purity through aforementioned methods. This work presents the first time that microwave-assisted high-temperature methods have been extended to Mo_6Se_8 and Mo_6Te_8. In contrast to conventional heating, which relies on slow heat transfer through evacuated quartz ampules, the microwave heating method employed here allows for rapid conversion of microwave radiation into thermal energy,[55] and the N_2 atmosphere within

the reaction vessel itself allows for virtually instantaneous heat transfer to the sample. Due to the rapid nature of this microwave heating, reaction times to obtain CPs are reduced from days to minutes, resulting in significant time and energy savings despite the required high temperatures (>900°C). Furthermore, the yield of this solid-state synthesis method is 100%, making it advantageous compared to many solution-based methods where unreacted precursors and product loss during separation often reduces overall yield.

The PXRD pattern for Mo_6S_8 shown in Fig. 2.2a indicates a rhombohedral crystal phase with an intense (101) signal that is characteristic of CPs, while the SEM image in Fig. 2.2b details the faceted polycrystalline morphology that is representative of the CPs studied in this work. The PXRD patterns, XPS spectra, and EDX spectra (Fig. S2.5) obtained before and after chemical etching confirm the complete removal of Cu from the Mo_6S_8 framework. PXRD and SEM of CP selenides and tellurides (Fig. S2.6) show similar characteristic diffraction peaks and polycrystalline morphology. Lattice parameters obtained by PXRD refinement for CP chalcogenides are shown in Table S2.1 and are consistent with literature values for the R-3H unit cell. Bulk CP composition was confirmed via EDX, as shown in Figs. S2.7-S2.9. For Mo_6S_8, the Mo L- and S K-edges overlap, convoluting quantitative determination of Mo and S, hence reported atomic % deviates significantly from expected values, although it is apparent from the EDX spectra presented in Fig. S2.7 that there is no compositional impurities.

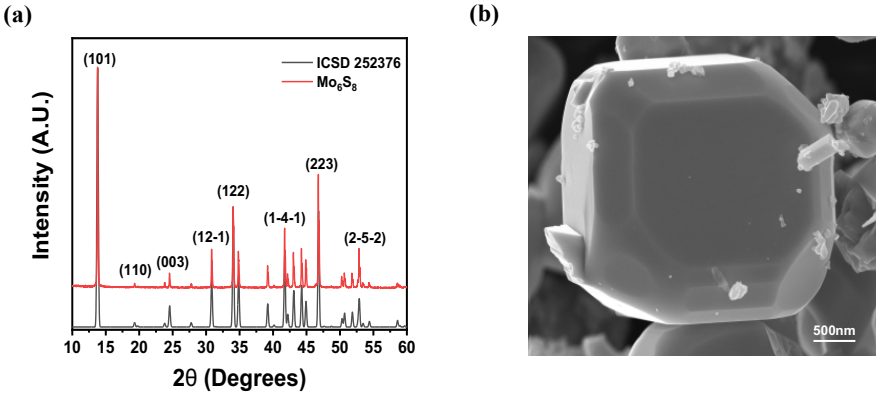

Figure 2.2. (a) PXRD patterns for Mo_6S_8 comparing experimental (red) and calculated pattern based on published data (black), and (b) SEM micrograph detailing the faceted morphology of polycrystalline Mo_6S_8.

Electronic Structure and Theoretical H Interaction*

The Mo L_3-Edge X-ray Absorption Near Edge Structure (XANES) for all three CPs are shown in Fig. 2.3 and reveal that as the electronegativity of the chalcogen species decreases, the photon energy required to induce a 2p→4d transition similarly decreases, suggesting a less oxidized Mo center which is the result of weaker electron withdrawal from Mo_6 by the X_8 cage. This is indicative that a more electronegative chalcogen strongly decreases the valence electron count of the Mo_6 octahedron, which makes the chalcogen a stronger Lewis base that will stabilize the absorbed proton more effectively during HER since H^+ is a hard Lewis acid. DFT calculations support this explanation.

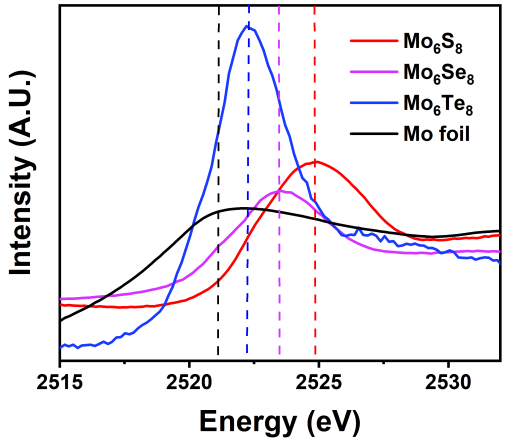

Figure 2.3. Mo L_3-Edge XANES for binary CP chalcogenides along with a Mo foil for reference, illustrating a pronounced red-shift as chalcogen electronegativity decreases from Mo_6S_8 (red) to Mo_6Te_8 (blue).

Calculated Gibbs free energies for proton adsorption (ΔG_H) on CP chalcogenides are shown in Fig. 2.4a along with Pt for reference. As expected, Pt exhibits the most favorable H^* binding interaction, while for CP chalcogenides, Mo_6S_8 is predicted to possess the most favorable ΔG_H, followed by Mo_6Se_8 and Mo_6Te_8 with ΔG_H of 0.48, 0.56, and 0.58 eV, respectively. The lower ΔG_H obtained for Mo_6S_8 corroborates our hypothesis that a stronger Lewis base adjacent to Mo stabilizes H^* more effectively thereby facilitating HER reaction kinetics. Furthermore, our calculations indicate that the most favorable adsorption site for all three CP surfaces is the bridge site between Mo and X, which can be seen in the slab images of Fig. S2.10

where H* is stabilized closest to X in Mo_6S_8 (X-H distance = 1.40 Å) and farthest from X in Mo_6Te_8 (X-H distance = 1.81 Å).

To further examine how the electronic structures of the CPs influence their reactivity, projected DOS were calculated for each material and plotted in Fig. 2.4b. As the electronegativity of the chalcogen increases, the d-band center energy decreases, suggesting a weaker interaction between H* and the Mo d-states. This result is consistent with the longer Mo-H bond calculated for Mo_6S_8. Conversely, the X-H bond strengthens as chalcogen electronegativity increases, and to a greater extent than the Mo-H bond weakens. This results in stronger overall adsorption of H* predicted for Mo_6S_8. We attribute the stronger X-H bond for the more electronegative chalcogens to both local and bulk electronic effects. The local contribution to the X-H bond strength results from orbital overlap which decreases with orbital size mismatch between the chalcogen and the H* 1s orbital (e.g. large mismatch between Te 5s and H 1s). The bulk contribution results from the charge density localization on the chalcogen atoms which increases with the electronegativity of X and is manifested in the electronic structure as a lower p-band center. The increased charge density on X leads to stronger bonding with H* and concomitantly decreases the charge density on Mo, weakening the Mo-H bond. To assess the influence of the local and bulk contributions on the strength of the X-H bond, we studied the effect of substituting only the chalcogen involved in the X-H bond with a different chalcogen. Three substitutions were considered: Se into Mo_6S_8, S into Mo_6Se_8 and S into Mo_6Te_8. The calculated ΔH_{ads} for these substitutions are shown in Fig. S2.11. We report calculated bond lengths, band centers, charge densities and ΔH_{ads} in Table S2.2. These substitutions change the local bonding environment yet have a minimal effect on the bulk electronic structure, exhibited by the negligible change in the d-band and p-band centers (< 0.05 eV) as well as by the negligible change in Mo charge densities. The Se substitution into Mo_6S_8 increases ΔH_{ads} by 0.08 eV resulting in an adsorption enthalpy that is only 0.03 eV lower than that of bulk Mo_6Se_8. Additionally, the Se-H bonds of both structures differ by only 0.01 Å, indicating that the local bonding environment influences the X-H bond strength more than the bulk electronic structure.

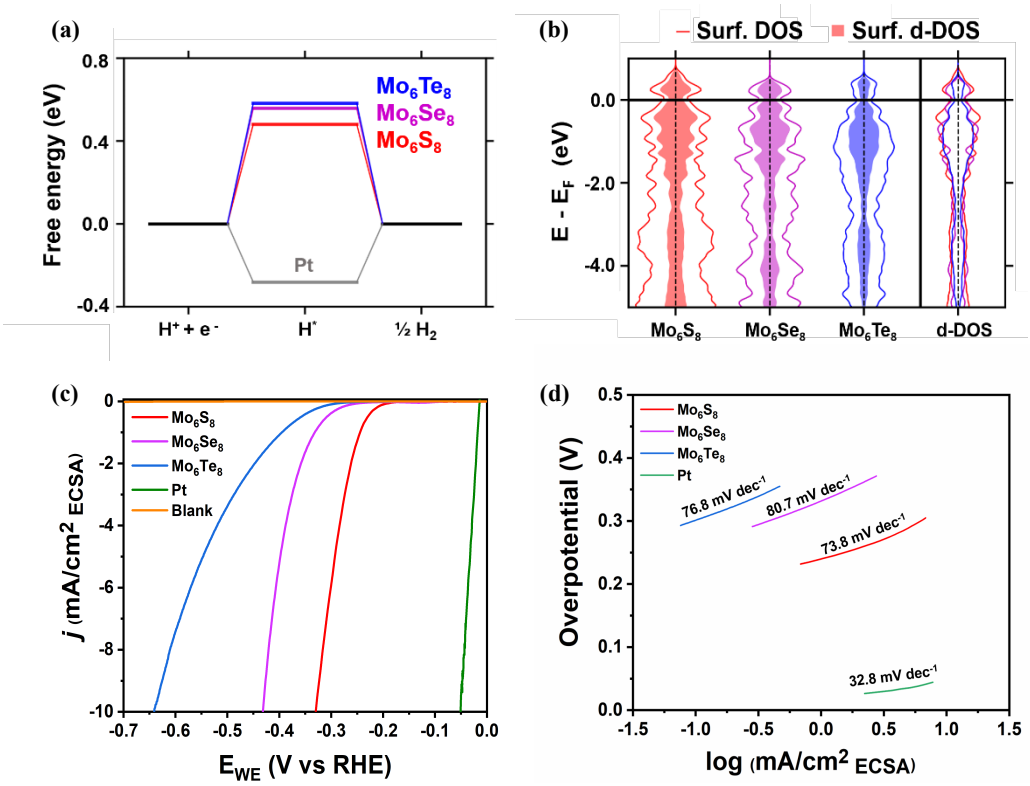

Figure 2.4. (a) Calculated adsorption energies of H* (ΔG_H) on all the surfaces discussed herein; (b) computed DOS which indicate a significantly larger d-DOS at the Fermi level for Mo_6S_8 than for Mo_6Se_8 and Mo_6Te_8; (c) HER polarization curves for CP chalcogenides electrodes in 0.5 M H_2SO_4, along with 20% Pt/C on Vulcan Carbon Cloth and a blank (carbon paper with PTFE/carbon black/IPA ink) for comparison; (d) corresponding Tafel plots for each CP catalyst, with Pt for comparison.

The S substitutions into Mo_6Se_8 and Mo_6Te_8 decrease ΔH_{ads} by 0.03 and 0.02 eV, respectively. The difference between ΔH_{ads} for the S substitution into Mo_6Se_8 and the Se substitution into Mo_6S_8 is less than 0.01 eV. However, the S-H bond is 0.14 Å shorter than the Se-H bond, further confirming that the local bonding environment contributes more substantially to the X-H bond strength, although the overall proton adsorption strength is comparable. Nonetheless, when comparing Mo_6S_8 against the two S substitutions into Mo_6Se_8 and Mo_6Te_8, ΔH_{ads} increases by 0.07 and 0.12 eV, respectively, indicating that the bulk electronic structure moderately affects the adsorption strength of the proton, which can be stabilized by decreasing the p-band center. The individual tunability of the local bonding environment and bulk electronic structure suggests that the ternary CP space may include promising HER catalysts with optimal properties for H adsorption. Furthermore, of the three chalcogenides S provides the best local bonding

environment and bulk electronic structure for stabilizing H*, in agreement with our calculations that Mo_6S_8 exhibits the lowest ΔG_H of the binary CPs.

Electrochemical HER activity

Polarization curves in 0.5 M H_2SO_4 and Tafel slopes for all three CP chalcogenides are shown in Fig. 2.4(c,d) along with curves for 20% Pt/C on Vulcan Carbon Cloth and a blank for reference, while numerical figures of merit are shown in Table 2.1. Current densities were normalized with respect to ECSA to account for any slight differences in particle sizes of the catalysts that were evaluated. Due to the ease with which tellurium compounds oxidize in air, Mo_6Te_8 electrodes were treated prior to electrolysis to ensure that the catalytic activity recorded came from Mo_6Te_8 and not the oxide. The Mo_6Te_8 electrodes were submerged in 0.5 M H_2SO_4 for 30 mins. Under these acidic conditions, TeO_2 spontaneously dissolves in the form of the telluryl ion, $HTeO_2^+$.[56,57] This ion further reduces to elemental tellurium under negative applied potential; therefore, following this 30 min dissolution period the electrolyte was replaced while continuously purging the cell with hydrogen to prevent re-oxidation of the electrode surface. The overpotential required to achieve a current density of 10 $mAcm^{-2}{}_{ECSA}$ follows the trend: $Mo_6S_8 < Mo_6Se_8 < Mo_6Te_8$, with values of 321 mV, 432 mV and 634 mV, respectively, indicating that on an energy-imput basis, Mo_6S_8 is the most efficient of the three catalysts studied. In addition, an overpotential of 265 mV is required to achieve 10 $mAcm^{-2}$ on a geometric basis for Mo_6S_8, which is consistent with many commonly reported bulk and nanostructured earth-abundant HER catalysts for which current density is normalized with respect to geometric surface area, as shown in Table S2.3.[22,46,58–61] Considering that the HER activity of Mo_6S_8 was measured using bulk polycrystalline catalyst material, considerable opportunity exists to improve the overpotential required to achieve a current density of 10 $mAcm^{-2}$ through dimensional reduction, as has been successful in many other HER catalyst materials such as MoS_2.[46]

The observed HER behavior agrees with the measured trend in Mo L-edge position across the three binary CPs, as coordination of Mo to an increasingly electronegative X species will yield a harder X_8 cage that favors H^* stabilization. Catalytic activity also agrees with calculated ΔG_H, confirming the effect ΔG_H plays on reaction kinetics. The Tafel slopes obtained for CP chalcogenides are all significantly higher than the Tafel slope for platinum, which suggests that the reaction proceeds via a Volmer-Heyrovsky mechanism that involves electrochemical desorption during a concerted proton-coupled electron transfer as the final step toward H_2 production.[62] The endergonic ΔG_H for all three CPs suggests low H^* surface coverage, further supporting a Volmer-Heyrovsky mechanism. The lower ΔG_H obtained for Mo_6S_8 agrees with its lower Tafel slope, which indicates fast proton adsorption followed by a sluggish desorption step,[63] while the CP selenides and tellurides undergo faster desorption due to their higher adsorption free energy.

To further investigate HER kinetics over CP electrocatalyst surfaces, EIS was performed to measure charge-transfer resistance (R_{ct}) at -0.5 V vs. Ag/AgCl as shown in Fig. S2.12. The significant increase R_{ct} from Mo_6S_8 (40.2Ω) to Mo_6Te_8 (436.0Ω) suggests significantly more sluggish kinetics as the electronegativity of the chalcogen decreases, which is to be expected based on previously discussed trends in the electronic structure.

Material	η at -10mAcm$^{-2}_{ECSA}$ (mV)	Tafel Slope (mVdec^{-1})	Exchange current density (mAcm$^{-2}_{ECSA}$)	R_{ct} (Ω)
Mo_6S_8	321	74	6.01×10^{-4}	3.2
Mo_6Se_8	432	81	9.57×10^{-5}	154.4
Mo_6Te_8	634	77	3.01×10^{-5}	446.0

Table 2.1. Compiled figures of merit for all three binary CPs studied herein.

Cycling stability as shown in Fig. 2.5a and Fig. S2.13 indicates an increase in overpotential to achieve 10 mA cm^{-2} after 1000 cycles of 5 mV for Mo_6S_8, 15 mV for Mo_6Se_8, and 16 mV for Mo_6Te_8; hence, Mo_6S_8 appears to be the most robust of the three CP compositions studied. EDX spectra for the binary CPs reveal consistent bulk composition of the catalysts after cycling, while SEM images indicate no significant changes

to the morphology or distribution of catalyst on the surface over the course of electrolysis for the sulfides and selenides (Figs. S2.7-S2.8). In the case of the tellurides, SEM images show a significant decrease in the surface coverage over the course of electrolysis (Fig. S2.9). We hypothesize that this is a result of weaker interactions between Mo_6Te_8 and the PTFE binding agent, making it less mechanically robust under the electrolysis conditions. XPS spectra shown in Figs. S2.14-2.16 indicate the presence of a native oxide layer that is significantly smaller after electrolysis on Mo_6S_8 and Mo_6Se_8 but slightly larger for Mo_6Te_8 as a result of the ease with which tellurium is oxidized under ambient conditions. However, it appears that the surface Mo and X composition is relatively consistent over the course of electrolysis, and due to the pre-treatment used for the CP tellurides it is unlikely that any native oxide persists under electrolysis conditions.

In order to confirm the apparent stability of the Mo_6S_8 composition, chronopotentiometry experiments were performed where current density was maintained at 10 mA cm^{-2} for 48hrs in order to observe overpotential as a function of electrolysis time. Fig. 2.5b shows that the overpotential for Mo_6S_8 was steady even over the course of long periods of electrolysis. The PXRD pattern for the Mo_6S_8 electrode before electrolysis (Fig. S2.17) reveals the characteristic (101) signal of CPs, which remains after 48 hrs of electrolysis without any significant changes in the diffraction pattern. Figs. S2.18-S2.19 show XPS spectra and SEM images of the electrode, respectively, which further confirm consistent catalyst composition and morphology over the course of prolonged electrolysis.

It is clear from the electrochemical and spectroscopic analyses presented here that Mo_6S_8 is the most promising binary CP catalyst composition, owing to its increased X site basicity that promotes favorable HER kinetics. This was also found to be the most stable composition of all three CPs and is, therefore, a promising candidate for systematic electronic structure and electrocatalytic evaluation

following ternary element intercalation between Mo_6X_8 units. Furthermore, CP sulfides have also been shown to be stable under reductive applied bias in basic conditions,[37,39] which extends the range of conditions in which ternary phases can be evaluated.

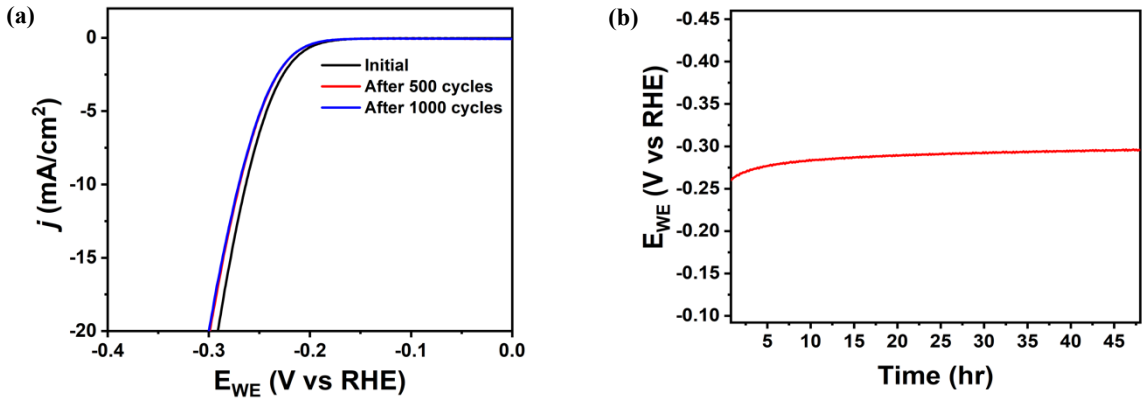

Figure 2.5. (a) HER polarization curves for Mo_6S_8 recorded before (black) and after 500 (red) and 1000 (blue) potential sweeps from 0.0 to −0.4 V vs. RHE in 0.5 M H_2SO_4 with current normalized with respect to geometric surface area; (b) Chronopotentiometry experiment with an Mo_6S_8 electrode illustrating a steady time-dependent overpotential at a current density of 10 $mAcm^{-2}$ over 48 hrs.

Conclusion

This work represents the first systematic study of the effect of chalcogen substitution on HER activity in acidic conditions for CP chalcogenide catalysts. It is also the first extension of microwave-assisted solid-state heating to molybdenum selenide and telluride materials. The result of Mo L-edge XAS for the three binary catalysts studied here reflects an expected increase in chalcogen basicity as the electron-withdrawing nature of the chalcogen increases, which leads to increased HER reactivity, in good agreement with fundamental hard-soft acid-base theory. The CP catalysts with more electronegative chalcogen species stabilized H* at HER-active Mo-X bridging sites more effectively, resulting in greatly improved HER activity for Mo_6S_8 compared to Mo_6Se_8 and Mo_6Te_8. DFT calculations indicate that this stabilization is due to a stronger X-H bond, which results from improved orbital overlap and a lower bulk p-band center. Furthermore, our calculations indicate that the position of the p-band center can be independently tuned to stabilize H* adsorption. Therefore, we conclude that for the binary CPs, the position of the p-band center

is a useful descriptor of the catalytic activity for HER which may provide critical insights for identifying ternary CP compositions with improved HER activity, and for investigating more complicated catalytic reactions where H adsorption is an important elementary step (e.g., electrochemical CO_2 and CO reduction). The p-band center may also prove to be a useful descriptor for catalytic activity of other transition metal chalcogenides.

Experimental characterization confirmed predictions from theory, indicating that HER activity decreases as the electronegativity of the chalcogen decreases. Mo_6S_8 exhibited an overpotential of 321 mV at 10 $mAcm^{-2}_{ECSA}$ compared to 432 mV and 634 mV for Mo_6Se_8 and Mo_6Te_8, respectively. Tafel slopes in the range of 74-82 $mVdec^{-1}$ for all CPs indicate that the rate-limiting step for all three compositions is electrochemical desorption as part of the Volmer-Heyrovsky mechanism. It is apparent from the strong agreement between our theoretical predictions and experimental characterization that HER activity in CP chalcogenides can be predictably affected by catalyst composition. This observation paves the way for future studies on the effect of ternary element-intercalation into CPs on catalytic activity and may ultimately lead to an effective method for predicting and analyzing new compositions of optimally reactive CP catalyst materials.

Supporting Information

Schematic of the electrochemical setup and electrode preparation setup; representative CVs of CP chalcogenides in a non-faradaic region; representative double-layer capacitance calculations; XPS and EDX survey scan of $Cu_2Mo_6S_8$ and Mo_6S_8 obtained after chemical etching; PXRD and SEM for Mo_6Se_8 and Mo_6Te_8 powders; EDX spectra for Mo6Te8 electrode before and after electrolysis; computationally predicted binding geometry for Hads on CP chalcogenides; calculated ΔHads in CP chalcogenides along with substitution of the chalcogen involved in the X–H bond for a different chalcogen; Nyquist plots for CP chalcogenides; polarization curves for Mo6Te8 and Mo6Te8 inks after 500 and 1000 cyclic voltammograms;

XPS spectra before and after electrolysis for Mo_6Te_8; PXRD for Mo_6S_8 electrode before and after chronopotentiometry over 48 h; SEM images for Mo_6S_8 electrode before and after chronopotentiometry over 48 h; lattice parameters for all CP chalcogenides; DFT calculated properties for CP chalcogenides; and comparison of the overpotentials of earth-abundant HER catalysts in acidic media

Acknowledgment

We would like to acknowledge the University of California, Davis for start-up funding, as well as support from the Cottrell Scholar program supported by the Research Corporation for Science Advancement (RCSA Grant ID#26780). We also acknowledge funding support from the NSF through UC Davis ChemEnergy REU program, grant #1560479 2) the NSF Graduate Research Fellowship, grant # 1650042. JTP thanks Chevron Corporation for funding through the UC Davis Institute of Transportation Chevron fellowship program. C.B.M. and N.R.S. were supported by the NSF (Awards CBET-1806079 and CHE-1800592). NRS was also supported by a U.S. Department of Education Graduate Assistance in Areas of National Need Fellowship under the Materials for Energy Conversion and Sustainability program. Part of this work was performed at the Stanford Nano Shared Facilities (SNSF), supported by the National Science Foundation under award ECCS-1542152. This research used resources of the National Energy Research Scientific Computing Center, a DOE Office of Science User Facility supported by the Office of Science of the U.S. Department of Energy under Contract No. DE-AC02-05CH11231 (Project ID: 60905). The SSRL Structural Molecular Biology Program is supported by the DOE Office of Biological and Environmental Research, and by the National Institutes of Health, National Institute of General Medical Sciences (including P41GM103393). The contents of this publication are solely the responsibility of the authors and do not necessarily represent the official views of NIGMS of NIH.

Publication Information, Copyright, and Author Acknowledgements

This chapter forms the basis for the following publication:

Ortiz-Rodríguez, J.C.†; Singstock, N.R.†; Perryman, J.T.; Hyler, F.P.; Jones, S.J.; Holder, A.M.; Musgrave, C.B.*; Velázquez, J. M.*, Stabilizing Hydrogen Adsorption Through Theory-Guided Substitution in Chevrel-Phase Mo_6X_8 (X=S, Se, Te) Electrocatalysts, *ACS Applied Materials, and Interfaces,* 2020, *12* (32) 35995–36003. https://pubs.acs.org/doi/10.1021/acsami.0c07207

Jessica C. Ortiz-Rodríguez conducted material synthesis, electrochemistry experiments, PXRD, SEM and EDX. NRS conducted computational calculations. JTP contributed to material synthesis as well as XPS acquisition and processing. FPH contributed to XAS acquisition and processing. SJJ contributed to material synthesis.

References

(1) Sharma, S.; Ghoshal, S. K. Hydrogen the Future Transportation Fuel: From Production to Applications. *Renew. Sustain. Energy Rev.* 2015, *43*, 1151–1158.

(2) Davis, S. J.; Lewis, N. S.; Shaner, M.; Aggarwal, S.; Arent, D.; Azevedo, I. L.; Benson, S. M.; Bradley, T.; Brouwer, J.; Chiang, Y. M.; Clack, C. T. M.; Cohen, A.; Doig, S.; Edmonds, J.; Fennell, P.; Field, C. B.; Hannegan, B.; Hodge, B. M.; Hoffert, M. I.; Ingersoll, E.; Jaramillo, P.; Lackner, K. S.; Mach, K. J.; Mastrandrea, M.; Ogden, J.; Peterson, P. F.; Sanchez, D. L.; Sperling, D.; Stagner, J.; Trancik, J. E.; Yang, C. J.; Caldeira, K. Net-Zero Emissions Energy Systems. *Science.* 2018, *360* (6396), eaas9793.

(3) Ayers, K. Review Gigawatt-Scale Renewable Hydrogen via Water Splitting as a Case Study for Collaboration : The Need to Connect Fundamental and Applied Research to Accelerate Solutions. *MRS Energy Sustain. A Rev. J.* 2017, *4*, 1–10.

(4) Baroutaji, A.; Wilberforce, T.; Ramadan, M.; Ghani, A. Comprehensive Investigation on Hydrogen and Fuel Cell Technology in the Aviation and Aerospace Sectors. *Renew. Sustain. Energy Rev.* 2019, *106*, 31–40.

(5) Spath P.L.; Mann, M. K. Life Cycle Assessment of Hydrogen Production via Natural Gas Steam Reforming. *Natl. Renew. Energy Lab.* 2001, Report No. TP-570-27637.

(6) Shamsi, H.; Haghi, E.; Raahemifar, K.; Fowler, M. Five-Year Technology Selection Optimization to Achieve Specific CO_2 Emission Reduction Targets. *Int. J. Hydrogen Energy* 2019, *44* (7), 3966–3984.

(7) Ludwig, J. R.; Schindler, C. S. Catalyst: Sustainable Catalysis. *Chem* 2017, *2* (3), 313–316.

(8) Abbas, M. A.; Bang, J. H. Rising Again: Opportunities and Challenges for Platinum-Free Electrocatalysts. *Chem. Mater.* 2015, *27* (21), 7218–7235.

(9) Evans, D. J.; Pickett, C. J. Chemistry and the Hydrogenases. *R. Soc. Chem.* 2003, *32*, 268–275.

(10) Rees, D. C.; Howard, J. B. The Interface Between the Biological and Inorganic Worlds : Iron-Sulfur Metalloclusters. *Science.* 2003, *300*, 929–932.

(11) Chorkendorff, I.; Jørgensen, K. P.; Nielsen, J. H.; Hinnemann, B.; Moses, P. G.; Nørskov, J. K.; Horch, S.; Bonde, J. Biomimetic Hydrogen Evolution: MoS_2 Nanoparticles as Catalyst for Hydrogen Evolution . *J. Am. Chem. Soc.* 2005, *127* (15), 5308–5309.

(12) Chorkendorff, I.; Bonde, J.; Jorgensen, K. P.; Horch, S.; Jaramillo, T. F.; Nielsen, J. H. Identification of Active Edge Sites for Electrochemical H_2 Evolution from MoS_2 Nanocatalysts. *Science.* 2007, *317* (5834), 100–102.

(13) Nørskov, J. K.; Abild-Pedersen, F.; Studt, F.; Bligaard, T. Density Functional Theory in Surface Chemistry and Catalysis. *Proc. Natl. Acad. Sci. U. S. A.* 2011, *108* (3), 937–943.

(14) Voiry, D.; Yamaguchi, H.; Li, J.; Silva, R.; Alves, D. C. B.; Fujita, T.; Chen, M.; Asefa, T.; Shenoy, V. B.; Eda, G.; Chhowalla, M. Enhanced Catalytic Activity in Strained Chemically Exfoliated WS_2 Nanosheets for Hydrogen Evolution. *Nat. Mater.* 2013, *12* (9), 850–855.

(15) Cheng, L.; Huang, W.; Gong, Q.; Liu, C.; Liu, Z.; Li, Y.; Dai, H. Ultrathin WS_2 Nanoflakes as a High-Performance Electrocatalyst for the Hydrogen Evolution Reaction. *Angew. Chemie - Int. Ed.* 2014, *53* (30), 7860–7863.

(16) Miao, R.; Dutta, B.; Sahoo, S.; He, J.; Zhong, W.; Cetegen, S. A.; Jiang, T.; Alpay, S. P.; Suib, S. L. Mesoporous Iron Sulfide for Highly Efficient Electrocatalytic Hydrogen Evolution. *J. Am. Chem. Soc.* 2017, *139* (39), 13604–13607.

(17) Fan, M.; Zhang, L.; Li, K.; Liu, J.; Zheng, Y.; Zhang, L.; Song, S.; Qiao, Z. A. FeS_2@C Core-Shell Nanochains as Efficient Electrocatalysts for Hydrogen Evolution Reaction. *ACS Appl. Nano Mater.* 2019, *2* (6), 3889–3896.

(18) Faber, M. S.; Dziedzic, R.; Lukowski, M. A.; Kaiser, N. S.; Ding, Q.; Jin, S. High-Performance Electrocatalysis Using Metallic Cobalt Pyrite (CoS_2) Micro- and Nanostructures. *J. Am. Chem. Soc.* 2014, *136* (28), 10053–10061.

(19) Wang, A.; Zhang, M.; Li, H.; Wu, F.; Yan, K.; Xiao, J. Combination of Theory and Experiment Achieving a Rational Design of Electrocatalysts for Hydrogen Evolution on the Hierarchically Mesoporous CoS2 Microsphere. *J. Phys. Chem. C.* 2019, *123* (22), 13428–13433.

(20) Wang, H.; Kong, D.; Johanes, P.; Cha, J. J.; Zheng, G.; Yan, K.; Liu, N.; Cui, Y. $MoSe_2$ and WSe_2 Nanofilms with Vertically Aligned Molecular Layers on Curved and Rough Surfaces. *Nano Lett.* 2013, *13* (7), 3426–3433.

(21) Yin, Y.; Zhang, Y.; Gao, T.; Yao, T.; Zhang, X.; Han, J.; Wang, X.; Zhang, Z.; Xu, P.; Zhang, P.; Cao, X.; Song, B.; Jin, S. Synergistic Phase and Disorder Engineering in 1T-$MoSe_2$ Nanosheets for Enhanced Hydrogen-Evolution Reaction. *Adv. Mater.* 2017, *29* (28), 1–8.

(22) Kong, D.; Wang, H.; Cha, J. J.; Pasta, M.; Koski, K. J.; Yao, J.; Cui, Y. Synthesis of MoS_2 and $MoSe_2$ Films with Vertically Aligned Layers. *Nano Lett.* 2013, *13* (3), 1341–1347.

(23) Zhang, X. L.; Hu, S. J.; Zheng, Y. R.; Wu, R.; Gao, F. Y.; Yang, P. P.; Niu, Z. Z.; Gu, C.; Yu, X.; Zheng, X. S.; Ma, C.; Zheng, X.; Zhu, J. F.; Gao, M. R.; Yu, S. H. Polymorphic Cobalt Diselenide as Extremely Stable Electrocatalyst in Acidic Media via a Phase-Mixing Strategy. *Nat. Commun.* 2019, *10* (1), 1–9.

(24) Zheng, Y. R.; Wu, P.; Gao, M. R.; Zhang, X. L.; Gao, F. Y.; Ju, H. X.; Wu, R.; Gao, Q.; You, R.; Huang, W. X.; Liu, S. J.; Hu, S. W.; Zhu, J.; Li, Z.; Yu, S. H. Doping-Induced Structural Phase Transition in Cobalt Diselenide Enables Enhanced Hydrogen Evolution Catalysis. *Nat. Commun.* 2018, *9* (1), 2533.

(25) Wang, K.; Ye, Z.; Liu, C.; Xi, D.; Zhou, C.; Shi, Z.; Xia, H.; Liu, G.; Qiao, G. Morphology-Controllable Synthesis of Cobalt Telluride Branched Nanostructures on Carbon Fiber Paper as Electrocatalysts for Hydrogen Evolution Reaction. *ACS Appl. Mater. Interfaces*. 2016, *8* (5), 2910–2916.

(26) McGlynn, J. C.; Dankwort, T.; Kienle, L.; Bandeira, N. A. G.; Fraser, J. P.; Gibson, E. K.; Cascallana-Matías, I.; Kamarás, K.; Symes, M. D.; Miras, H. N.; Ganin, A. Y. The Rapid Electrochemical Activation of $MoTe_2$ for the Hydrogen Evolution Reaction. *Nat. Commun.* 2019, *10* (1), 4916.

(27) Anantharaj, S.; Kundu, S.; Noda, S. Progress in Nickel Chalcogenide Electrocatalyzed Hydrogen Evolution Reaction. *J. Mater. Chem. A*. 2020, *8* (8), 4174–4192.

(28) Hilsenbeck, S. J.; Mccarley, R. E.; Goldman, A. I.; Schrader, G. L. Hydrodesulfurization Activity and EXAFS Characterization of Novel Ternary Tin and Lanthanum Molybdenum Sulfide Catalysts. *Chem. Mater.* 1998, *4756* (4), 125–134.

(29) Schewe-Miller, I. M.; Koo, K. F.; Columbia, M.; Li, F.; Schrader, G. L. Synthesis and Characterization of Lead Chevrel Phase Thin Films for Hydrodesulfurization Catalysis. *Chem. Mater.* 1994, *6* (12), 2327–2335.

(30) McCarty, K. F.; Schrader, G. L. Hydrodesulfurization by Reduced Molybdenum Sulfides: Activity and Selectivity of Chevrel Phase Catalysts. *Ind. Eng. Chem. Prod. Res. Dev.* 1984, *23* (4), 519–524.

(31) Alonso-Vante, N; Schubert, B; Tributsch, H. Transition Metal Cluster Materials for Multi-Electron Transfer Catalysis. *Mater. Chem. Phys.* 1989, *22*, 281–307.

(32) Fisher, C; Alonso-Vante, N; Fiechter, S. T. H. Electrocatalytic Properties of Mixed Transition Metal Tellurides (Chevrel-Phases) for Oxygen Reduction. *J. Appl. Electrochem.* 1995, *25*, 1004–1008.

(33) Alonso-Vante, N.; Shubert, B; Tributsch, H.; Perrin, A. Influence of D-State Density and Chemistry of Transition Metal Cluster Selenides on Electrocatalysis. *J. Catal.* 1988, *112*, 384–391.

(34) Alonso-Vante, N; Tributsch, H. Energy Conversion Catalysis Using Semiconducting Transition Metal Cluster Compounds. *Lett. to Nat.* 1986, *323*, 431–432.

(35) Yante, N. A.; Jaegermann, W. H.; Hónle, W.; Yvon, K. Electrocatalysis of Oxygen Reduction by Chalcogenides Containing Mixed Transition Metal Clusters. *J. Am. Chem. Soc.* 1987, *2025*, 3251–3257.

(36) Perryman, J. T.; Ortiz-Rodrıguez, J. C.; Jude, J. W.; Hyler, F. P.; Davis, R. C.; Mehta, A.; Kulkarni, A. R. Metal-Promoted Mo_6S_8 Clusters: A Platform for Probing Ensemble Effects on the Electrochemical Conversion of CO_2 and CO to Methanol. *Mater. Horizons*. 2020, *7*, 193–202.

(37) Naik, K. M.; Sampath, S. Cubic Mo_6S_8-Efficient Electrocatalyst Towards Hydrogen Evolution Over Wide PH Range. *Electrochim. Acta*. 2017, *252*, 408–415.

(38) Ojha, K.; Banerjee, S.; Sharma, M.; Dagar, P. Synthesis of Chevrel Phase ($Cu_{1.8}Mo_6S_8$) in Composite with Molybdenum Carbide for Hydrogen Evolution Reactions. *Bull. Mater. Sci.* 2018, *41* (5), 119.

(39) Jiang, J.; Gao, M.; Sheng, W.; Yan, Y. Hollow Chevrel-Phase $NiMo_3S_4$ for Hydrogen Evolution in Alkaline Electrolytes. *Angew. Chemie*. 2016, *128* (49), 15466–15471.

(40) Perryman, J. T.; Hyler, F. P.; Ortiz-Rodríguez, J. C.; Mehta, A.; Kulkarni, A. R.; Velázquez, J. M. X-Ray Absorption Spectroscopy Study of the Electronic Structure and Local Coordination of 1st Row Transition Metal-Promoted Chevrel-Phase Sulfides. *J. Coord. Chem.* 2019, *72* (8), 1322–1335.

(41) K.Yvon, A. P. Charge Transfer and Valence Electron Concentration in Chevrel Phases. *Solid State Commun.* 1981, *37* (86), 325–327.

(42) Lancry, E.; Levi, E.; Gofer, Y.; Levi, M.; Salitra, G.; Aurbach, D. Leaching Chemistry and the Performance of the Mo_6S_8 Cathodes in Rechargeable Mg Batteries. *Chem. Mater.* 2004, *16* (14), 2832–2838.

(43) Borodziński, J. J.; Lasia, A. Study of Hydrogen Evolution on Selected PTFE-Bonded Porous Electrodes. *Int. J. Hydrogen Energy*. 1993, *18* (12), 985–994.

(44) Su, H.; Sita, C.; Pasupathi, S. The Effect of Gas Diffusion Layer PTFE Content on the Performance of High Temperature Proton Exchange Membrane Fuel Cell. *Int. J. Electrochem. Sci.* 2016, *11* (4), 2919–2926.

(45) McCrory, C. C. L.; Jung, S.; Ferrer, I. M.; Chatman, S. M.; Peters, J. C.; Jaramillo, T. F. Benchmarking Hydrogen Evolving Reaction and Oxygen Evolving Reaction Electrocatalysts for Solar Water Splitting Devices. *J. Am. Chem. Soc.* 2015, *137* (13), 4347–4357.

(46) Kibsgaard, J.; Chen, Z.; Reinecke, B. N.; Jaramillo, T. F. Engineering the Surface Structure of MoS_2 to a Preferentially Expose Active Edge Sites for Electrocatalysis. *Nat. Mater.* 2012, *11* (11), 963–969.

(47) Kresse, G.; Furthmüller, J. Efficient Iterative Schemes for Ab Initio Total-Energy Calculations Using a Plane-Wave Basis Set. *Phys. Rev. B - Condens. Matter Mater. Phys.* 1996, *54* (16), 11169–11186.

(48) Hammer, B.; Hansen, L. B.; Nørskov, J. K. Improved Adsorption Energetics within Density-Functional Theory Using Revised Perdew-Burke-Ernzerhof Functionals. *Phys. Rev. B - Condens. Matter Mater. Phys.* 1999, *59* (11), 7413–7421.

(49) Sun, J.; Ruzsinszky, A.; Perdew, J. Strongly Constrained and Appropriately Normed Semilocal Density Functional. *Phys. Rev. Lett.* 2015, *115* (3), 036402.

(50) Mathew, K.; Sundararaman, R.; Letchworth-Weaver, K.; Arias, T. A.; Hennig, R. G. Implicit Solvation Model for Density-Functional Study of Nanocrystal Surfaces and Reaction Pathways. *J. Chem. Phys.* 2014, *140* (8), 084106.

(51) Manz, T. A.; Limas, N. G. Introducing DDEC6 Atomic Population Analysis: Part 1. Charge Partitioning Theory and Methodology. *RSC Adv.* 2016, *6* (53), 47771–47801.

(52) Atkins, P. *Physical Chemistry*, 6th ed.; Oxford University Press, 1998.

(53) Nørskov, J. K.; Bligaard, T.; Logadottir, A.; Kitchin, J. R.; Chen, J. G.; Pandelov, S.; Stimming, U. Trends in the Exchange Current for Hydrogen Evolution. *J. Electrochem. Soc.* 2005, *152* (3), J23-J26.

(54) Chase, M. W. NIST-JANAF Thermochemical Tables. *Journal of Physical and Chemical Reference Data*. 1998.

(55) Levin, E. E.; Grebenkemper, J. H.; Pollock, T. M.; Seshadri, R. Protocols for High Temperature Assisted-Microwave Preparation of Inorganic Compounds. *Chem. Mater.* 2019, *31* (18), 7151–7159.

(56) Parsons, R. Atlas of Electrochemical Equilibria in Aqueous Solutions. *J. Electroanal. Chem. Interfacial Electrochem.* 1967, *13* (4), 471.

(57) Barbier, M. J.; De Becdelievre, A. M.; De Becdelievre, J. Electrochemical Study of Tellurium Oxido-Reduction in Aqueous Solutions. *J. Electroanal. Chem.* 1978, *94* (1), 47–57.

(58) Benck, J. D.; Hellstern, T. R.; Kibsgaard, J.; Chakthranont, P.; Jaramillo, T. F. Catalyzing the Hydrogen Evolution Reaction (HER) with Molybdenum Sulfide Nanomaterials. *ACS Catal.* 2014, *4*, 3957–3971.

(59) Chen, Z.; Cummins, D.; Reinecke, B. N.; Clark, E.; Sunkara, M. K.; Jaramillo, T. F. Core-Shell MoO_3-MoS_2 Nanowires for Hydrogen Evolution: A Functional Design for Electrocatalytic Materials. *Nano Lett.* 2011, *11* (10), 4168–4175.

(60) Benck, J. D.; Chen, Z.; Kuritzky, L. Y.; Forman, A. J.; Jaramillo, T. F. Amorphous Molybdenum Sulfide Catalysts for Electrochemical Hydrogen Production: Insights into the Origin of Their Catalytic Activity. *ACS Catal.* 2012, *2* (9), 1916–1923.

(61) Merki, D.; Fierro, S.; Vrubel, H.; Hu, X. Amorphous Molybdenum Sulfide Films as Catalysts for Electrochemical Hydrogen Production in Water. *Chem. Sci.* 2011, *2* (7), 1262–1267.

(62) Zeng, M.; Li, Y. Recent Advances in Heterogeneous Electrocatalysts for the Hydrogen Evolution Reaction. *J. Mater. Chem. A*. 2015, *3* (29), 14942–14962.

(63) Feng, W.; Pang, W.; Xu, Y.; Guo, A.; Gao, X.; Qiu, X.; Chen, W. Transition Metal Selenides for Electrocatalytic Hydrogen Evolution Reaction. *ChemElectroChem*. 2020, *7* (1), 31–54.

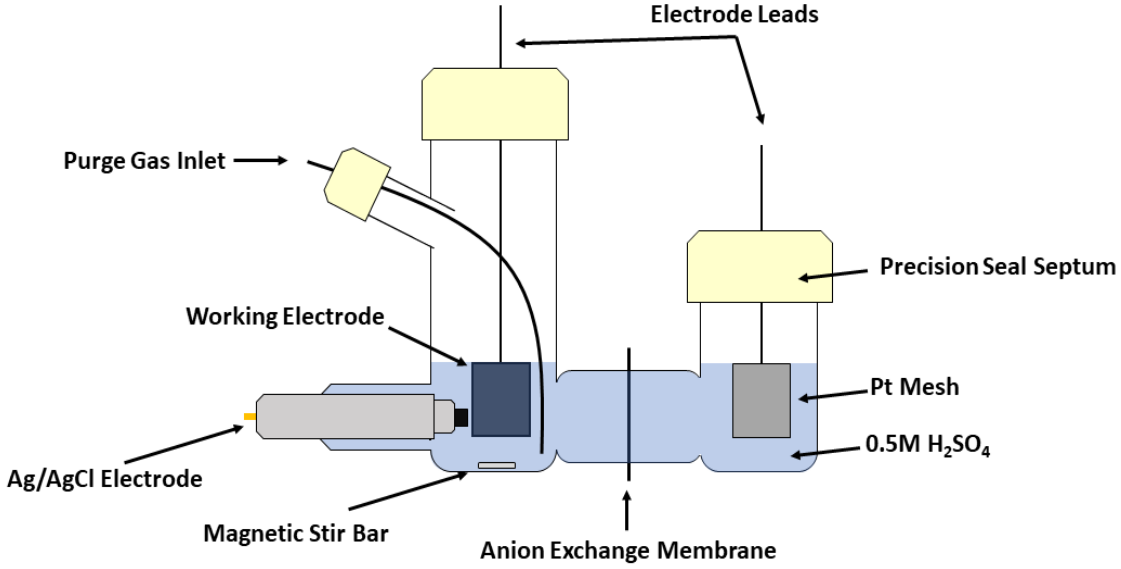

Figure S2.1. Schematic showing the custom-blown H-cell configured electrolysis cell. Platinum mesh, Toray carbon paper deposited with CP ink and Ag/AgCl were used as counter, working and reference electrodes, respectively.

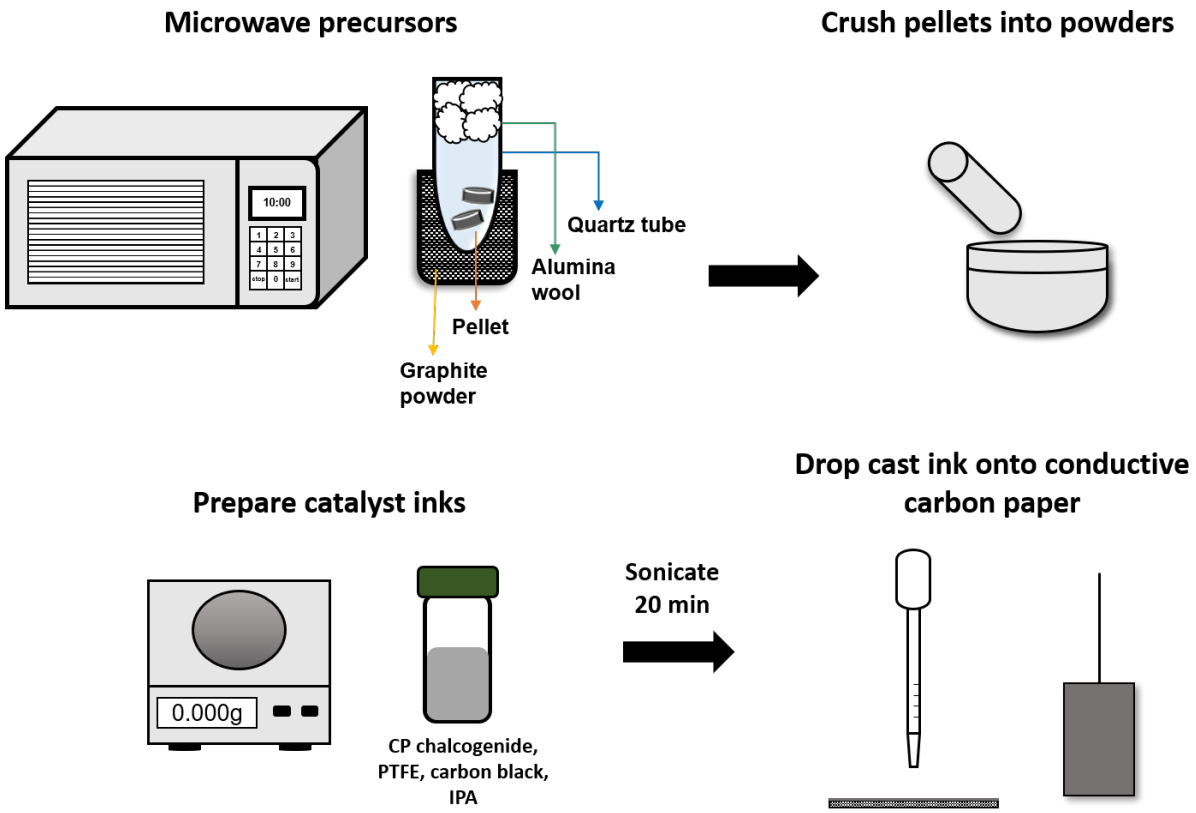

Figure S2.2. Schematic showing the fabrication process of CP electrodes. Appropriate precursors are weighted in a glovebox, ball-milled, and pressed into pellets. The pellets are then heated using a conventional microwave with an adapted Ar line. The obtained pellets are crushed into powders and made into inks consisting of CP chalcogenide, PTFE, carbon black and IPA. Catalyst inks are then drop-casted onto conductive carbon paper and dried under vacuum overnight before being used as electrodes.

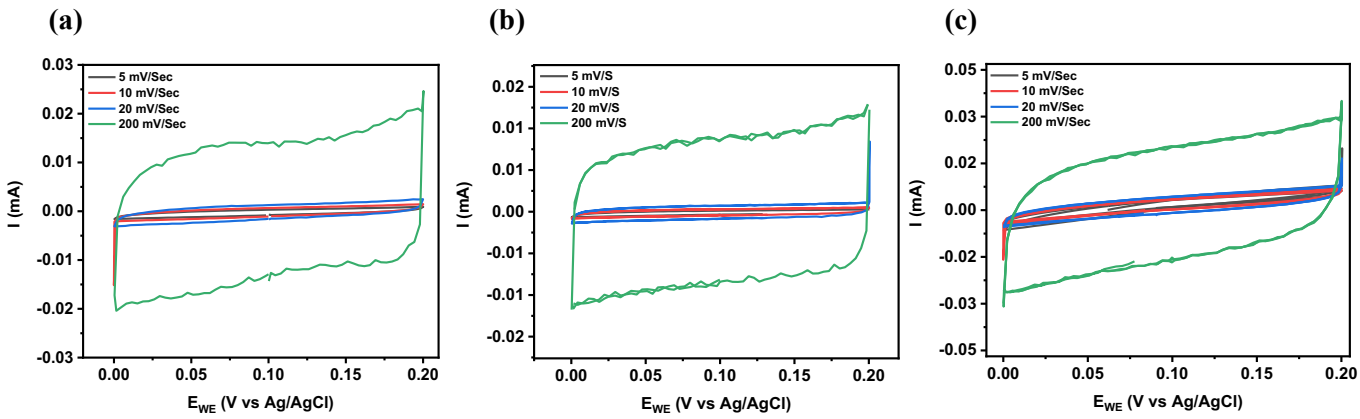

Figure S2.3. Cyclic voltammograms of (a) Mo_6S_8, (b) Mo_6Se_8, and (c) Mo_6Te_8 in a non-Faradaic region at varying scan rates.

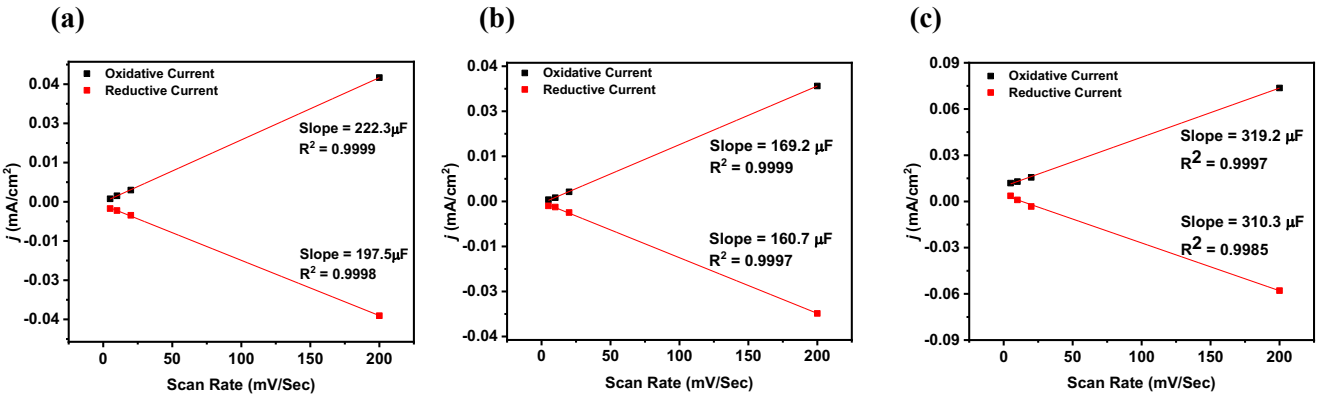

Figure S2.4. Representative cathodic and anodic charging currents plotted as a function of scan rate for (a) Mo_6S_8, (b) Mo_6Se_8, and (c) Mo_6Te_8. The double-layer capacitance of the system is taken as the average of the absolute value of the slopes.

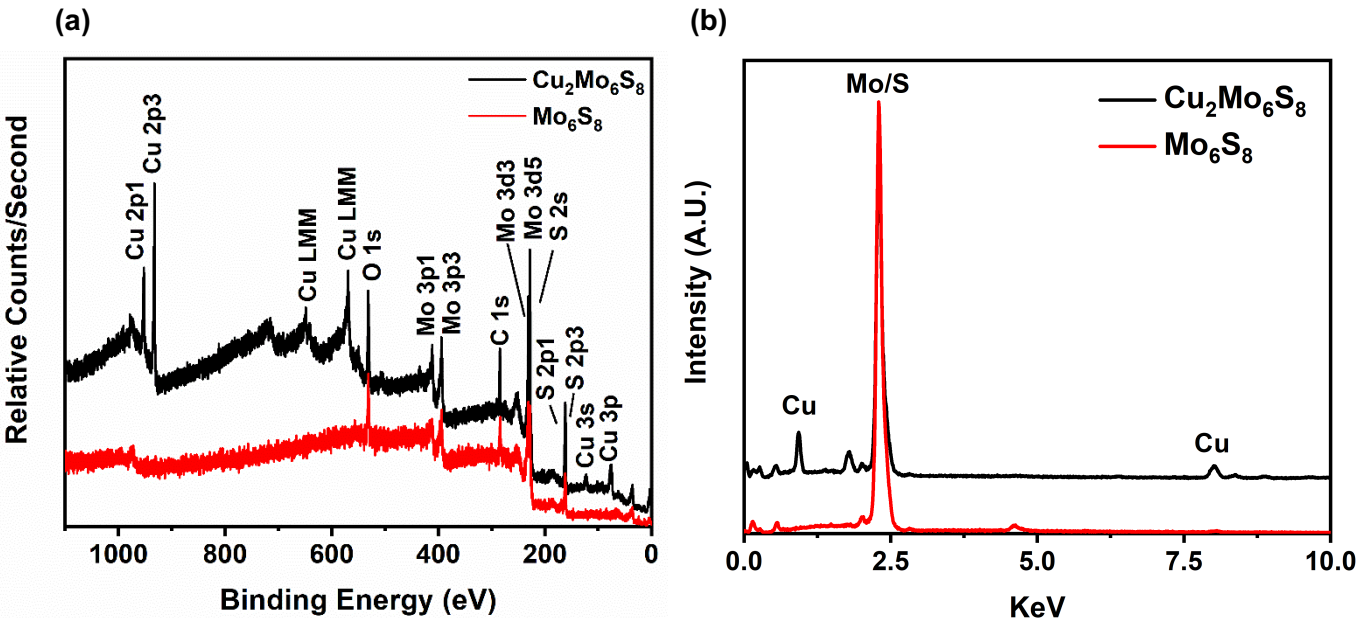

Figure S2.5. XPS (a) and EDX (b) survey scan of $Cu_2Mo_6S_8$ (black) and Mo_6S_8 obtained after chemical etching (red). The absence of Cu peaks in both, the Mo_6S_8 XPS and EDX scans confirm that there is no surface or bulk Cu in the structure in any detectable limit respectively.

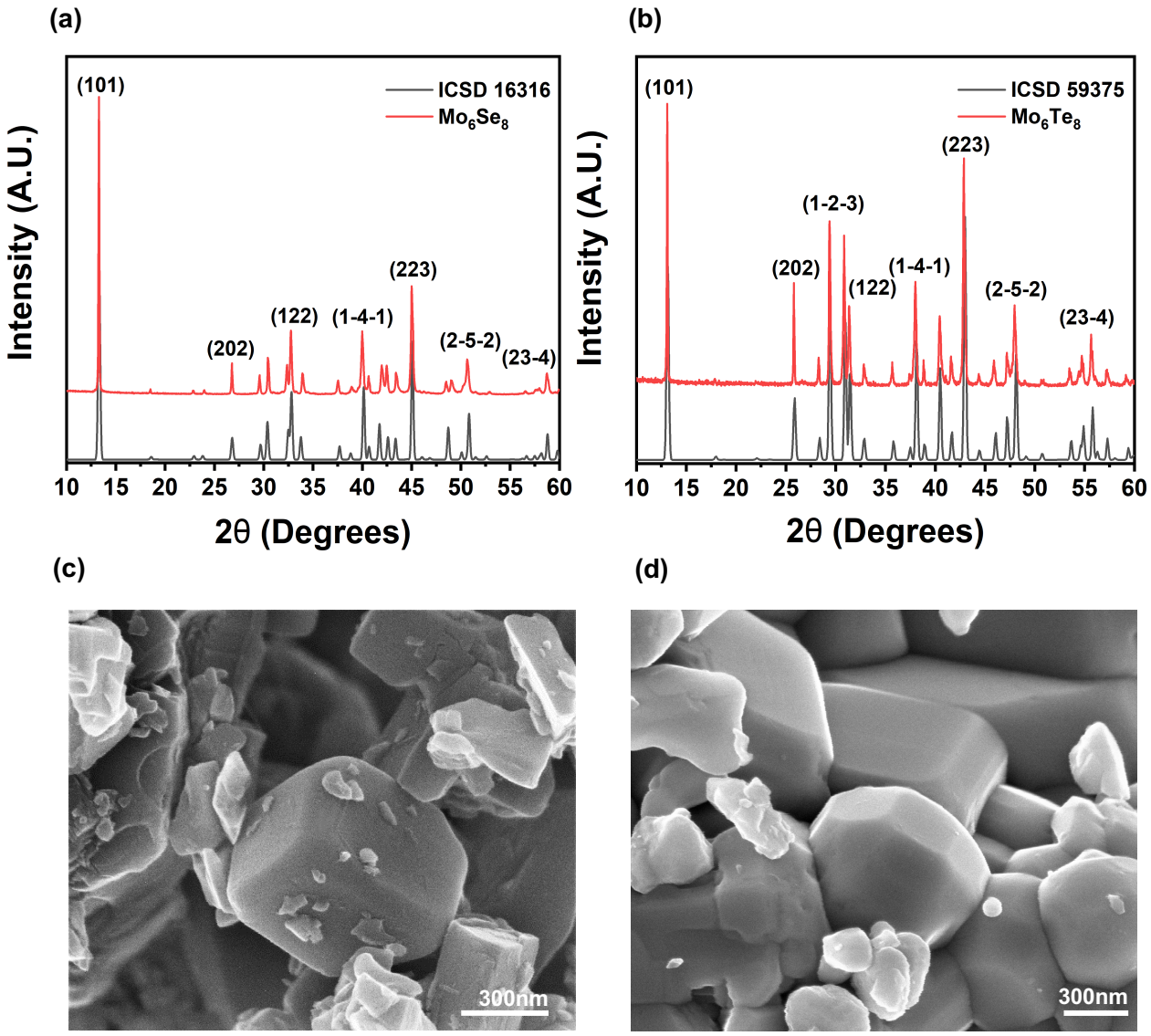

Figure S2.6. PXRD patterns for (a) Mo_6Se_8 and (b) Mo_6Te_8 along with their corresponding calculated pattern. SEM images detailing the faceted morphology of polycrystalline (c) Mo_6Se_8 and (d) Mo_6Te_8.

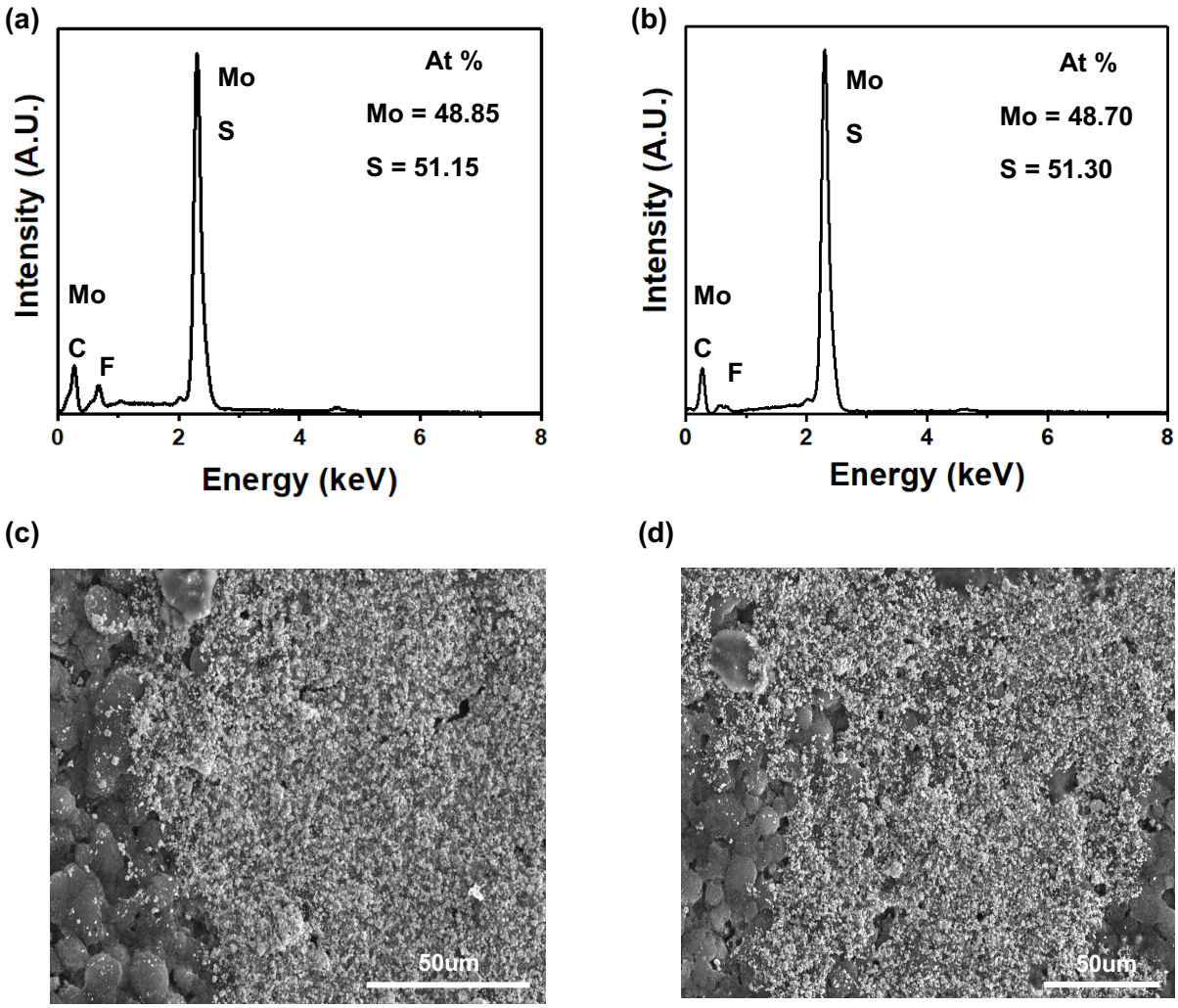

Figure S2.7. EDX spectra for Mo_6S_8 electrode (a) before and (b) after 1000 cyclic voltammograms (0.0 to −0.45 V versus RHE) in 0.5M H_2SO_4 deoxygenated via H_2 purging for 30 minutes prior to electrochemical measurements. Spectra reveal consistent bulk composition of the catalyst after electrolysis. SEM images (c) before and (d) after electrolysis on the same electrode, indicating that no significant changes to the morphology or distribution of catalyst on the surface took place over the course of electrolysis.

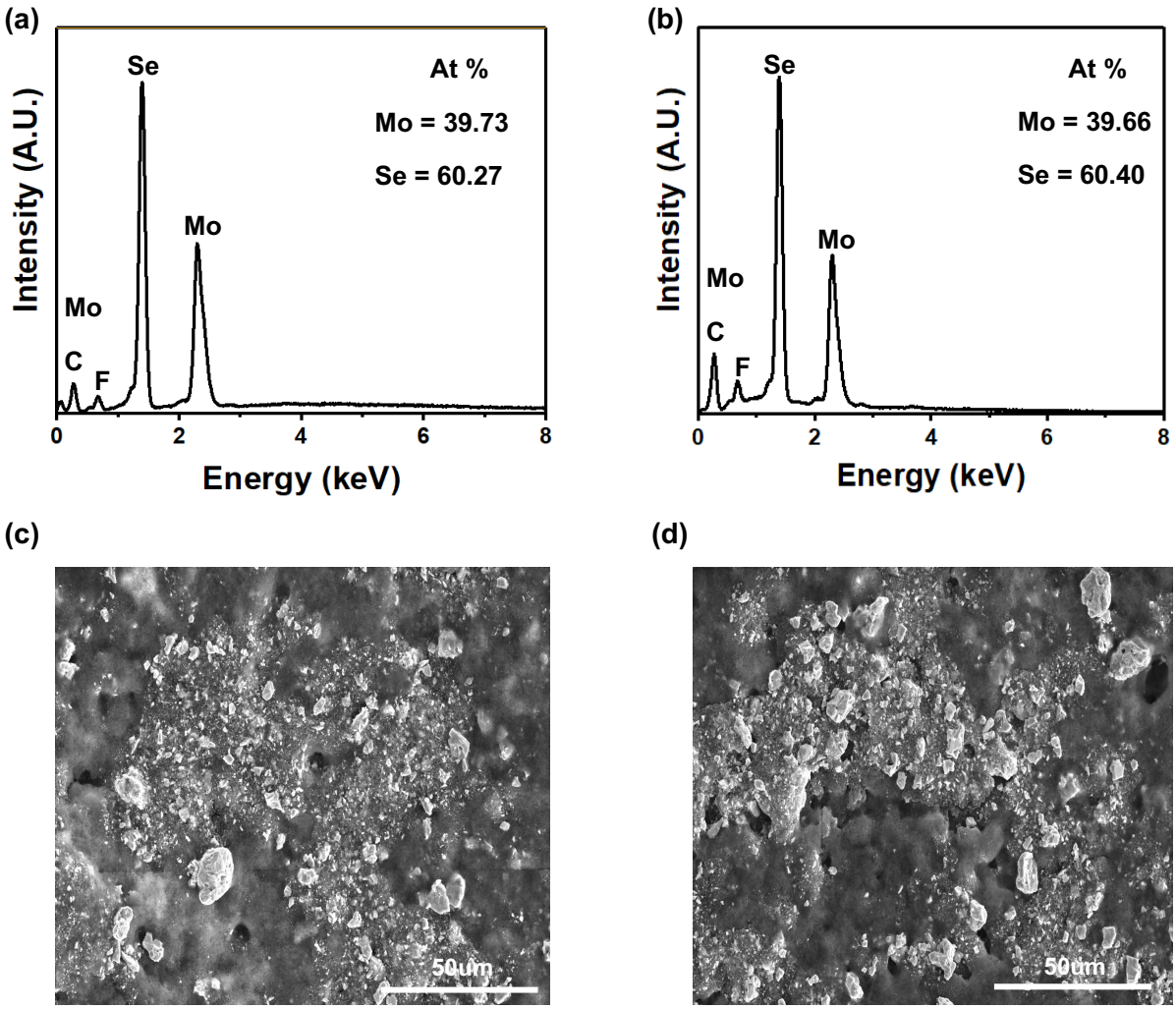

Figure S2.8. EDX spectra for Mo_6Se_8 electrode (a) before and (b) after 1000 cyclic voltammograms (0.0 to −0.45 V versus RHE) in 0.5M H_2SO_4 deoxygenated via H_2 purging for 30 minutes prior to electrochemical measurements. Spectra reveal consistent bulk composition of the catalyst after electrolysis. SEM images (c) before and (d) after electrolysis on the same electrode, indicating that no significant changes to the morphology or catalyst distribution on the surface took place over the course of electrolysis.

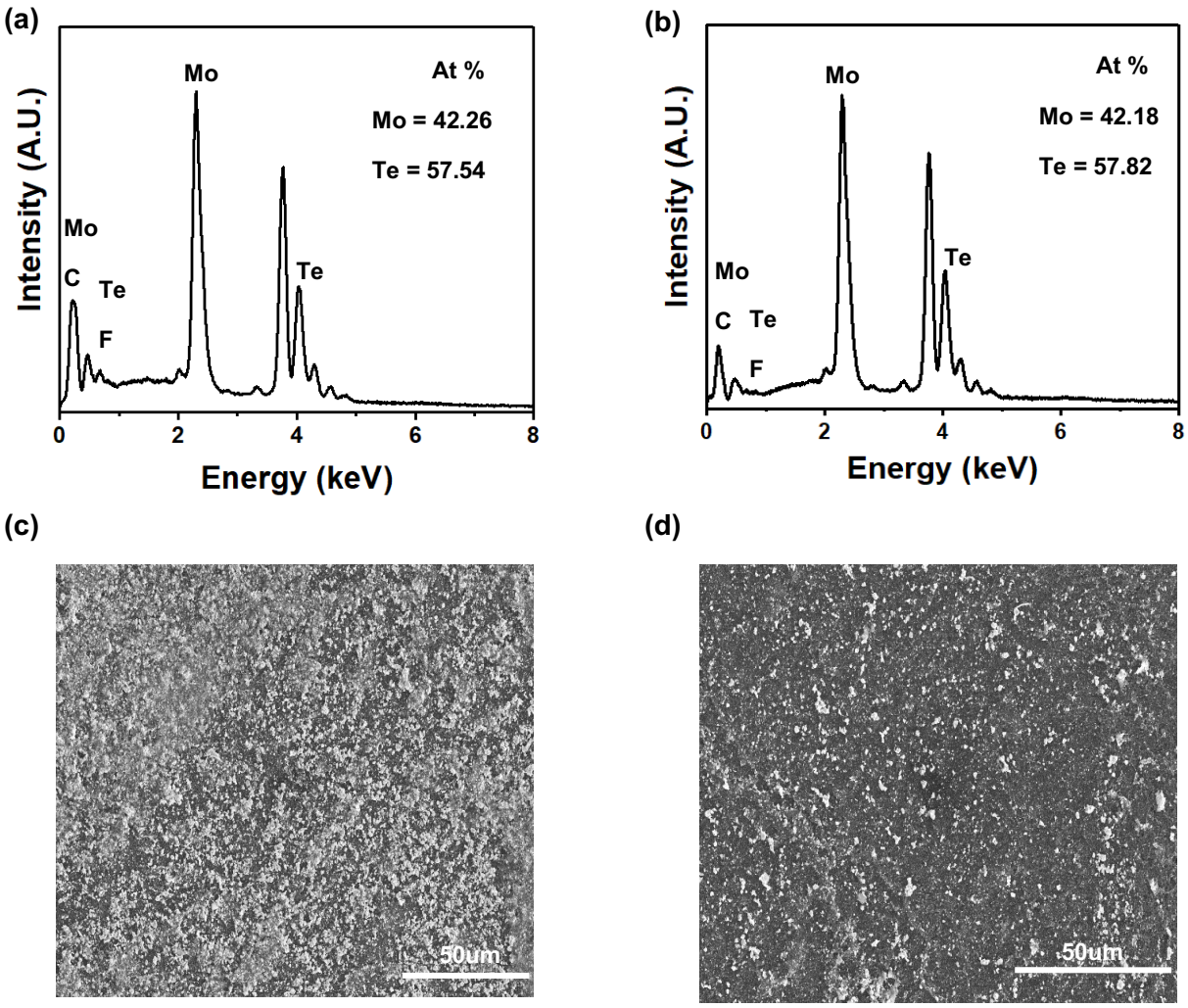

Figure S2.9. EDX spectra for Mo_6Te_8 electrode (a) before and (b) after 1000 cyclic voltammograms (0.0 to −0.45 V versus RHE) in 0.5M H_2SO_4 deoxygenated via H_2 purging for 30 minutes prior to electrochemical measurements. Spectra reveal consistent bulk composition of the catalyst after electrolysis. SEM images (c) before and (d) after electrolysis on the same electrode, indicating significant catalyst loss on the electrode surface over the course of electrolysis.

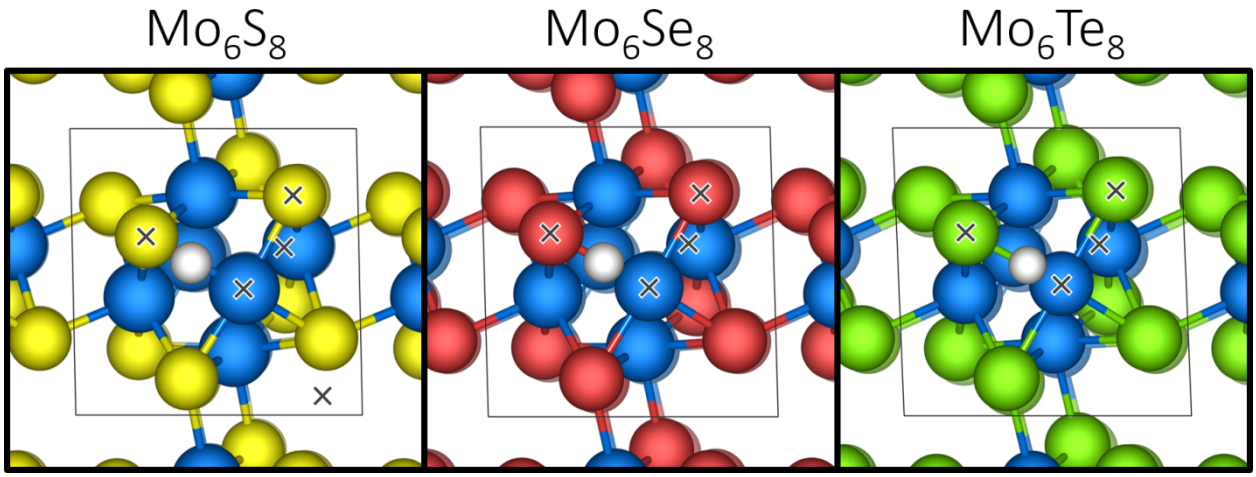

Figure S2.10. Computationally predicted binding geometry for H_{ads} (white) on each binary CP studied. In each case, H_{ads} is stabilized at bridging Mo-X sites, and black "X" indicates where adsorption free energy is unfavorable for HER. In addition to bridging Mo-X sites, Mo sites, X sites, and X-X sites were evaluated and determined to be unfavorable for each CP composition. Worth noting is that as X basicity increases, H_{ads} stabilization occurs farther from the more oxidized Mo site in Mo-X.

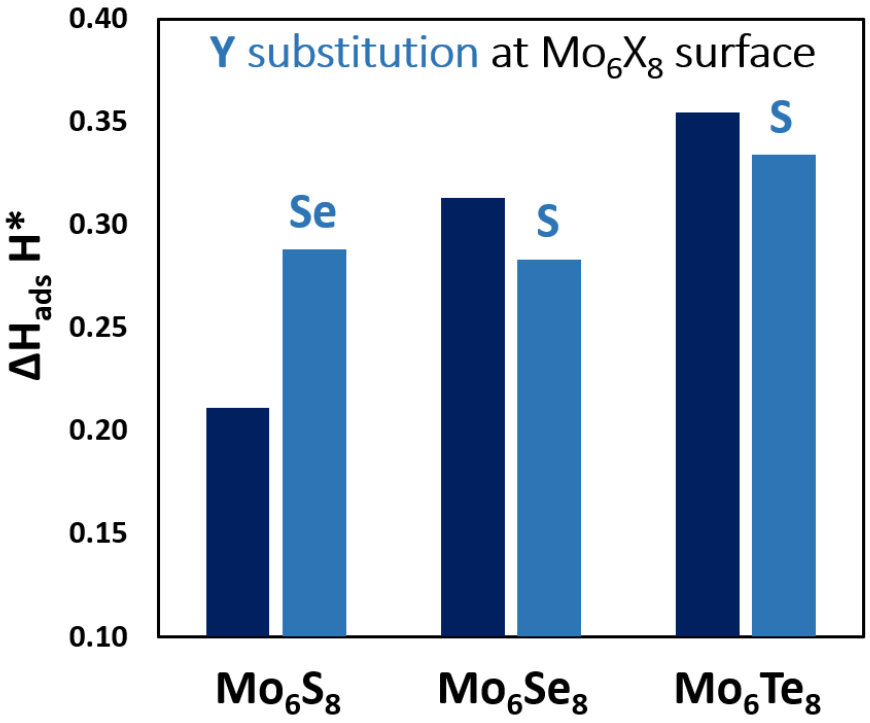

Figure S2.11. Calculated ΔH_{ads} for H* in binary CP chalcogenides along substitution of the chalcogen involved in the X-H bond for a different chalcogen.

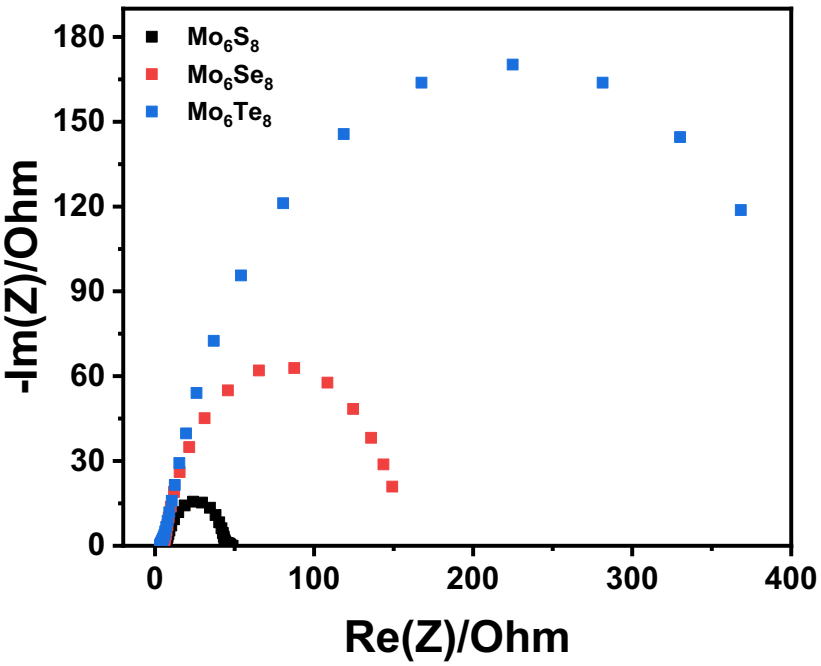

Figure S2.12. Nyquist plots of CP chalcogenides under an applied bias of -0.27V vs RHE, indicating significant increases in charge transfer resistance from Mo_6S_8 (black) to Mo_6Te_8 (blue).

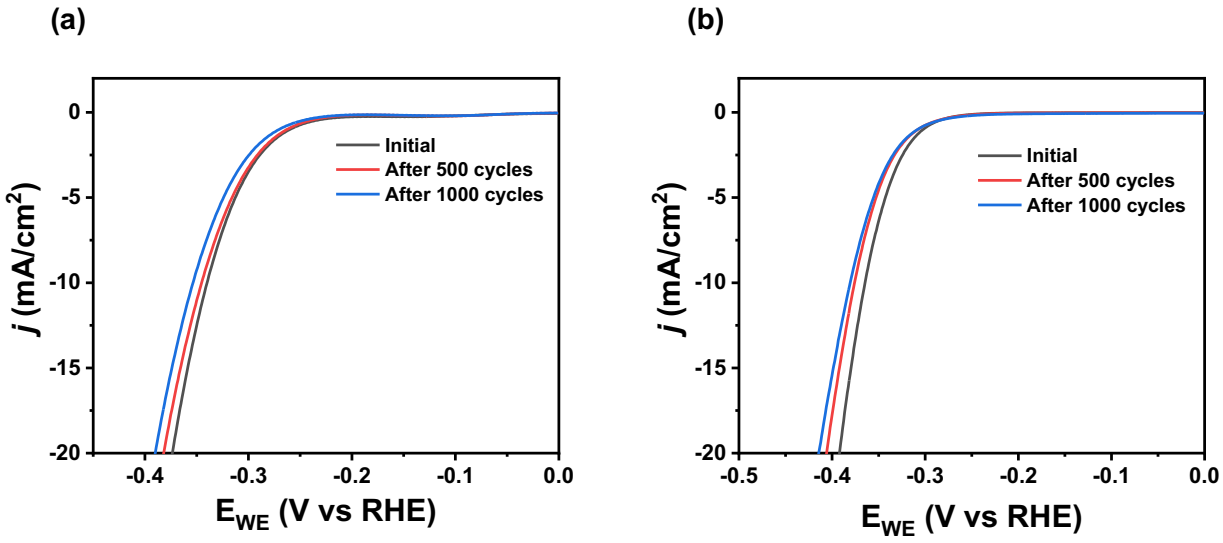

Figure S2.13. HER polarization curves recorded before and after 500 and 1000 cyclic voltamograms (0.0 to −0.45 V versus RHE) in 0.5 M H_2SO_4 for (a) Mo_6Se_8 and (b) Mo_6Te_8.

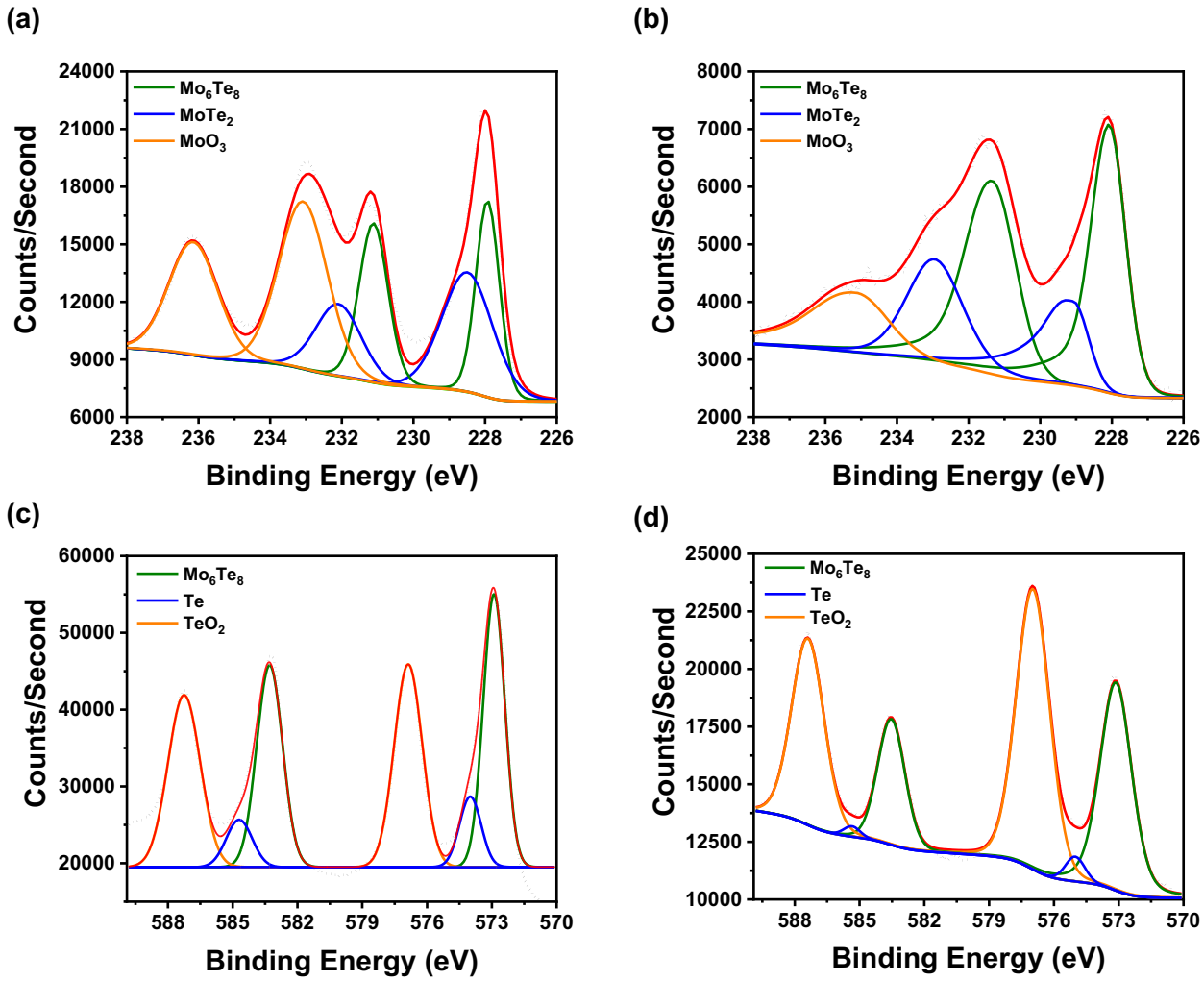

Figure S2.14. Mo 3d XPS spectra for Mo_6Te_8 (a) before, and (b) after electrolysis, as well as the Te 3d XPS spectra (c) before, and (d) after electrolysis.

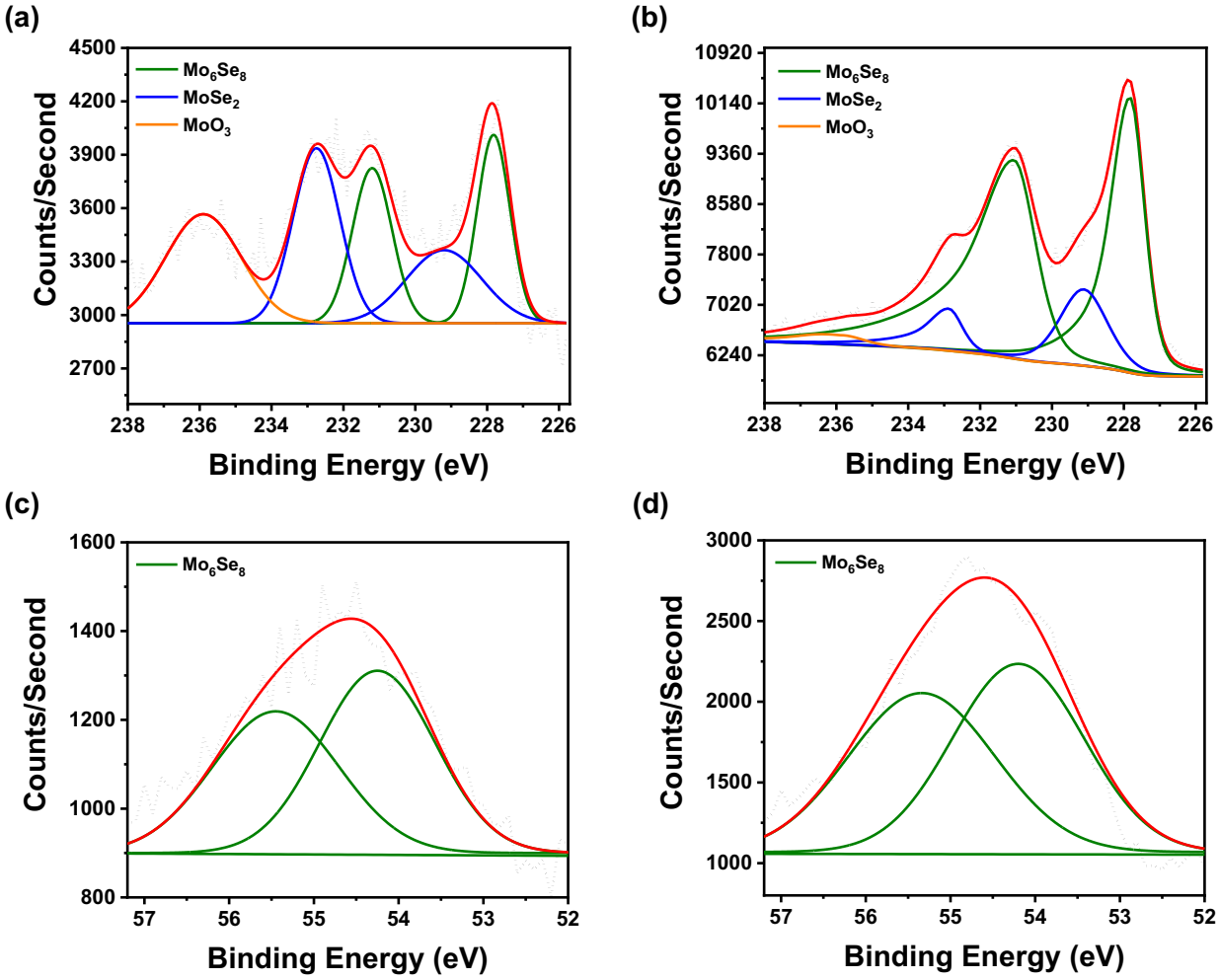

Figure S2.15. Mo 3d XPS spectra for Mo_6Se_8 (a) before, and (b) after electrolysis, as well as the Se 3d XPS spectra (c) before and (d) after electrolysis.

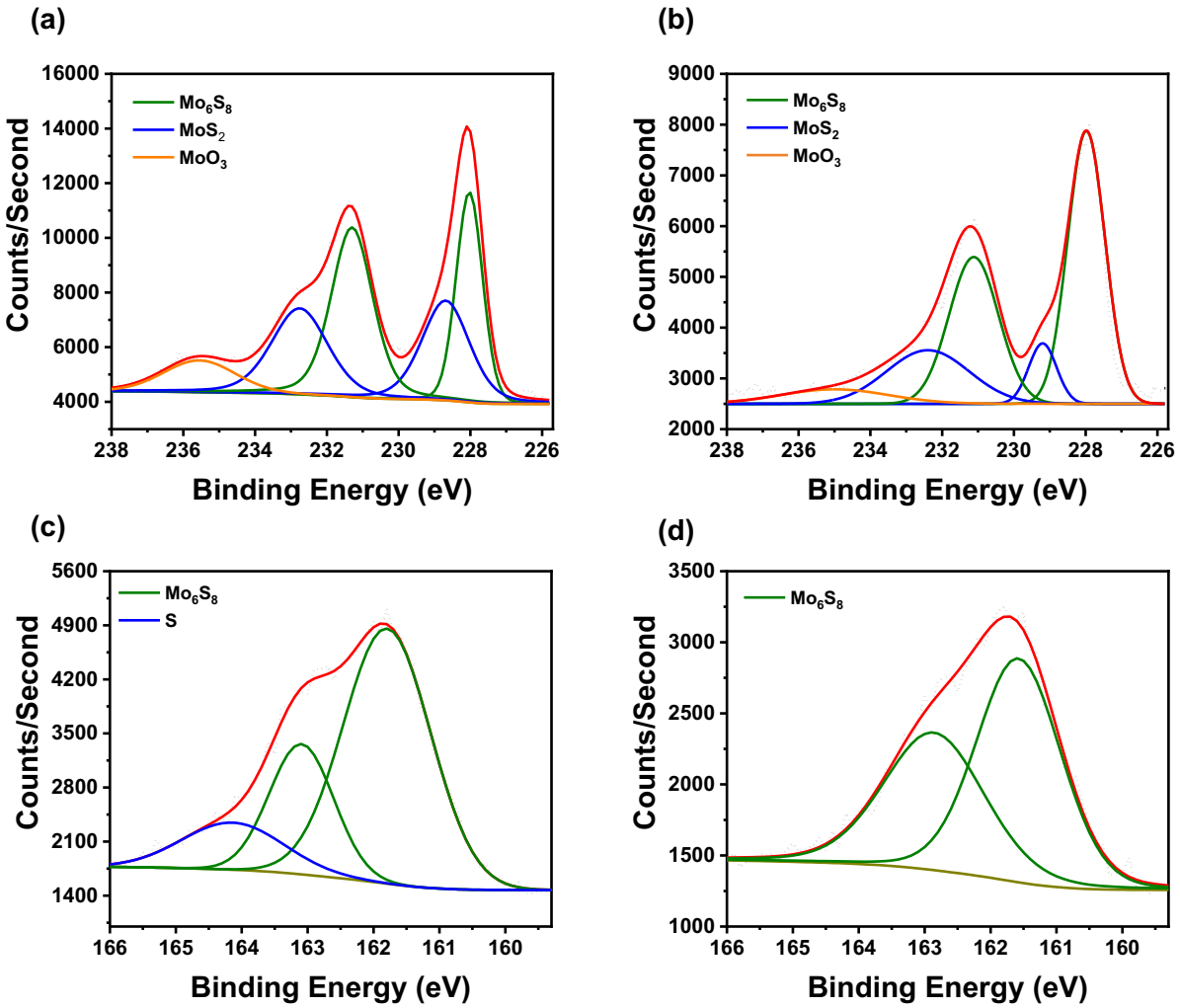

Figure S2.16. Mo 3d XPS spectra for Mo_6S_8 (a) before and (b) after electrolysis, as well as the S 2P XPS spectra (c) before and (d) after electrolysis.

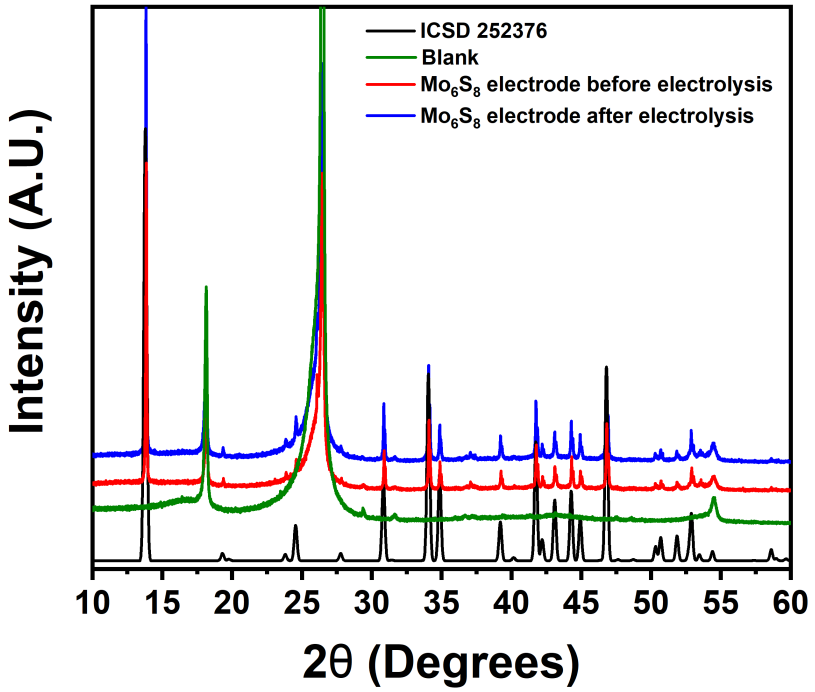

Figure S2.17. PXRD patterns for Mo_6S_8 electrode before (red) and after (blue) chronopotentiometry over 48 hrs along the corresponding Mo_6S_8 calculated pattern (black) and a blank (green) for comparison. The blank was made by dropcasting a carbon black/PTFE/IPA ink on toray paper.

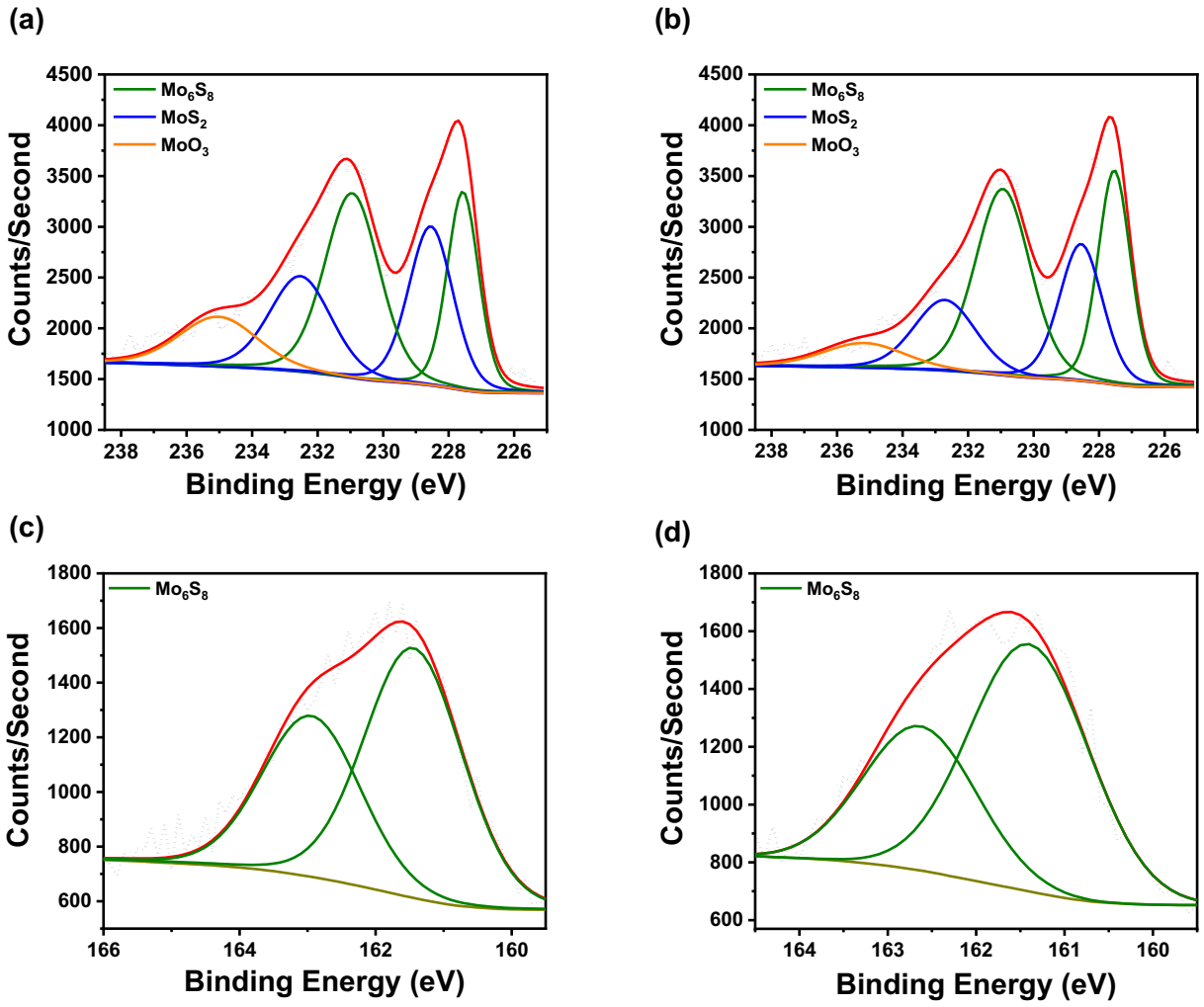

Figure S2.18. Mo 3d XPS spectra for Mo_6S_8 (a) before, and (b) after 48 hrs of chronopotentiometry, as well as the S 2P XPS spectra (c) before, and (d) after electrolysis.

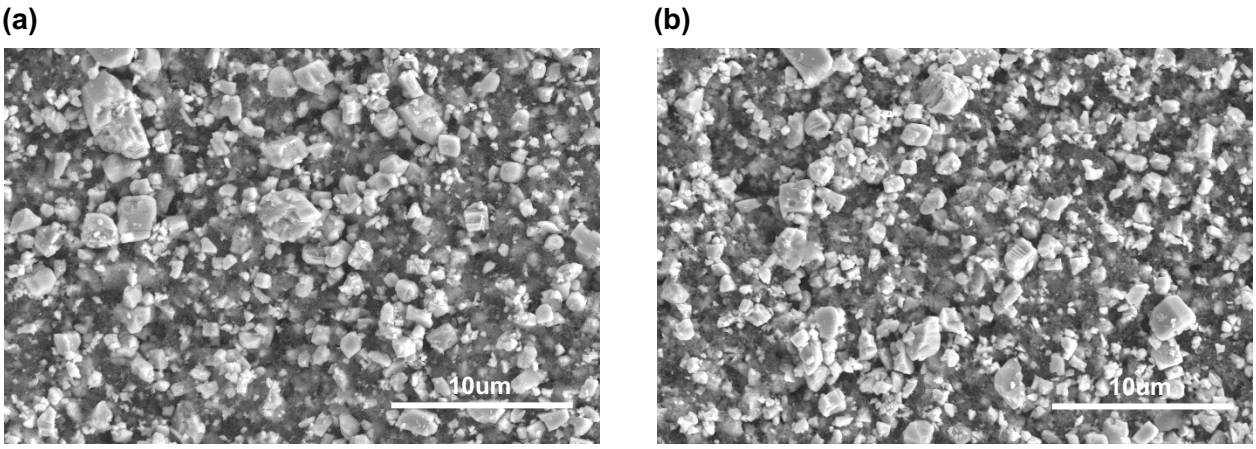

Figure S2.19. SEM images of Mo_6S_8 electrode before (a) and after (b) 48 hrs of chronopotentiometry showing no significant changes in the morphology or catalyst distribution on the surface over the course of electrolysis.

Material	Unit Cell Parameter	Experimental Value	Literature Value	% Difference
Mo_6S_8 (R-3H)	a	9.1924 Å	9.1910 Å	0.02
	b	9.1924 Å	9.1910 Å	0.02
	c	10.8886 Å	10.2290 Å	6.25
	α	90º	90º	0.00
	β	90º	90º	0.00
	γ	120º	120º	0.00
	Volume	796.820 $Å^3$	797.006 $Å^3$	0.02
Mo_6Se_8 (R-3H)	a	9.5751 Å	9.5448 Å	0.32
	b	9.5751 Å	9.5448 Å	0.32
	c	11.1311 Å	11.2095 Å	0.70
	α	90º	90º	0.00
	β	90º	90º	0.00
	γ	120º	120º	0.00
	Volume	883.798 $Å^3$	884.400 $Å^3$	0.07
Mo_6Te_8 (R-3H)	a	10.1882 Å	10.179Å	0.09
	b	10.1882 Å	10.179Å	0.09
	c	11.6448 Å	11.674Å	0.25
	α	90º	90º	0.00
	β	90º	90º	0.00
	γ	120º	120º	0.00
	Volume	1046.793 $Å^3$	1047.520$Å^3$	0.07

Table S2.1. Lattice parameters extracted from Pawley refinement for all CP chalcogenides structures studied in this work.

Material	ΔG_{ads} [1,2] (eV)	ΔH_{ads} [1] (eV)	Mo-H (Å)	X-H (Å)	d-band center (eV)	p-band center (eV)	X (surf) charge density	Mo (surf) charge density
Mo_6S_8	0.481	0.211	2.182	1.396	-2.732	-3.611	-0.4325	0.7522
Mo_6Se_8	0.558	0.313	2.058	1.565	-2.145	-2.856	-0.3343	0.6384
Mo_6Te_8	0.583	0.355	1.945	1.806	-2.096	-2.737	-0.1542	0.3377
Pt	-0.264[3]	-	-	-	-	-	-	-
Mo_6S_8-Se[4]	-	0.288	2.079	1.557	-2.731	-3.599	-0.3879	0.7188
Mo_6Se_8-S[4]	-	0.283	2.123	1.414	-2.145	-2.857	-0.3982	0.6759
Mo_6Te_8-S[4]	-	0.334	2.142	1.407	-2.131	-2.783	-0.3642	0.4638

Table S2.2. Calculated properties for CP chalcogenides.

[1] H_2O* included for Mo_6X_8

[2] Free energy of adsorption at 298 K

[3] H* calculated on Pt at full coverage. Additional adsorption energies (ΔG) calculated with SCAN are: -0.522, -0.374 and -0.649 eV for ¼, ½, and ¾ coverage, respectively. These values are notably lower than those calculated with RPBE: -0.126, -0.030, 0.052 and 0.154 for ¼, ½, ¾ and full coverage, respectively.

[4] Single X site substitution into the corresponding CP at the surface chalcogenide site that bonds with H*

Catalyst	η at -10mAcm^{-2} (mV)	Reference
MoS_2–MoO_3 core–shell nanowires	250	[1]
Mesoporous Double Gyroid MoS_2	220	[2,3]
Vertically Aligned MoS_2 Thin Films	440	[3,4]
Amorphous Molybdenum Sulfides	200	[5]
Electrodeposited amorphous MoS_3	242	[3,6]
Mo_6S_8	265	This work

Table S2.3. Comparison of the overpotentials of other Earth-abundant HER catalysts in acidic media based on current densities that were normalized against their geometric surface areas.

References:

(1) Chen, Z.; Cummins, D.; Reinecke, B. N.; Clark, E.; Sunkara, M. K.; Jaramillo, T. F. Core-Shell MoO3-MoS2 Nanowires for Hydrogen Evolution: A Functional Design for Electrocatalytic Materials. *Nano Lett*. 2011, *11* (10), 4168–4175.

(2) Kibsgaard, J.; Chen, Z.; Reinecke, B. N.; Jaramillo, T. F. Engineering the Surface Structure of MoS 2 to a Preferentially Expose Active Edge Sites for Electrocatalysis. *Nat. Mater.* 2012, *11* (11), 963–969.

(3) Benck, J. D.; Hellstern, T. R.; Kibsgaard, J.; Chakthranont, P.; Jaramillo, T. F. Catalyzing the Hydrogen Evolution Reaction (HER) with Molybdenum Sul Fi de Nanomaterials. *ACS Catal.* 2014, *4*, 3957–3971.

(4) Kong, D.; Wang, H.; Cha, J. J.; Pasta, M.; Koski, K. J.; Yao, J.; Cui, Y. Synthesis of MoS2 and MoSe2 Films with Vertically Aligned Layers. *Nano Lett.* 2013, *13* (3), 1341–1347.

(5) Benck, J. D.; Chen, Z.; Kuritzky, L. Y.; Forman, A. J.; Jaramillo, T. F. Amorphous Molybdenum Sulfide Catalysts for Electrochemical Hydrogen Production: Insights into the Origin of Their Catalytic Activity. *ACS Catal.* 2012, *2* (9), 1916–1923.

(6) Merki, D.; Fierro, S.; Vrubel, H.; Hu, X. Amorphous Molybdenum Sulfide Films as Catalysts for Electrochemical Hydrogen Production in Water. *Chem. Sci.* 2011, *2* (7), 1262–1267.

Chapter 3: Charge Transport Dynamics in Microwave Synthesized One-Dimensional Molybdenum Chalcogenides

Abstract

Scalable synthesis of one-dimensional molybdenum chalcogenides with tunable electronic properties may be critical for the development of nanoscale electronic device components as well as functional energy-conversion catalysts. Herein, we report the direct synthesis of one-dimensional potassium-intercalated molybdenum chalcogenides in the pseudo-Chevrel–Phase family [$K_2Mo_6X_6$; X = S, Se, Te] through a rapid microwave-assisted solid-state heating protocol. Interfacial capacitance as well as charge transfer dynamics during aqueous proton reduction are both explored as a function of chalcogen composition. We observe a significant change in the anisotropic nucleation of these structures as the chalcogen increases in size and decreases in electronegativity from sulfur to tellurium, with the former dramatically encouraging nucleation of well-defined nanomaterials in comparison to the latter. These anisotropic structures exhibit increased specific capacitance from 2.25 F g–1 to 10.28 F g–1 as the electronegativity of the chalcogen increases (Te < Se < S). Charge transfer kinetics for proton reduction follow a similar chalcogen-dependence, with the smallest charge transfer resistance being 1.16 Ω for K2Mo6S6 at −0.6 V vs RHE, compared to 3.7 Ω for K2Mo6Te6 at the same potential. Results discussed herein highlight interesting composition-dependent properties that could guide the future selection and development of molybdenum chalcogenide materials.

Introduction

Evolving industrial applications for functional materials are driving an increase in our need for precisely engineered compositions that exhibit favorable physicochemical properties for reactions of interest.[1–3] One approach to establishing transferrable design principles across material classes is to identify compositionally flexible frameworks to study and subsequently optimize.[4,5] Such frameworks would ideally

be characterized by i) tunable multinary compositions, ii) modular bonding landscapes that also lend themselves to efficient synthetic protocols allowing for fine control over dimensionality and morphology,[6] and iii) quantifiable and application-specific functionality criteria that—in the case of heterogeneous electrocatalysis, for example—include metrics like hydrogen adsorption affinity and interfacial resistance to charge transfer.[7–11] Identifying and investigating material families that have requisite properties for any given application will enable meaningful extraction of design principles that inform optimizations of functional atomic configurations.

To this end, metal chalcogenides are exceptionally promising because of their readily interchangeable binary and ternary compositions, their tendency to form well-defined 0D-3D dimensionalities at different composition thresholds, as well as their proven applications in electronics,[12–16] energy conversion,[15,17–2021] and energy storage.[16,19,22] While much attention has been afforded to understand composition-dependent properties in transition metal dichalcogenides (MX_2; M = transition metal; X = S, Se, Te) in particular,[12,13,16,20,22,23] far fewer experimental investigations have been dedicated to understanding ternary chalcogenides such as the interesting one-dimensional $M_2Mo_6X_6$ (M= alkali metal; X = S, Se, Te) system, also known as Pseudo-Chevrel-Phases (PCPs). [24–27] Besides the interesting properties associated to 1D systems due to electron confinement,[28–31] PCPs have been identified as alternative materials for nanodevices due to their predicted high elasticity, stiffness, thermal stability, and conductivity.[15,32] Furthermore, properties that lend themselves to composites[33,34], sensors[35], and photovoltaic devices[36] have also been explored for this family of materials.

As shown in Fig. 3.1, the PCP structure is characterized by infinite Mo_6X_6 chains separated by chalcogen-coordinated metal intercalant ions that reside in hexagonal channels formed between adjacent Mo_6X_6 chains. Intuitively, the wire-like extended structure of these chains results in a high degree of electrical anisotropy, which has made PCPs an excellent system for studying the effect composition on electron transport in their 1D structures and evaluating fundamental properties pertinent to the design of

novel nanomaterials.[15,25,26,32,37] Furthermore, the electronic properties of this ternary system can be easily tuned by changing chalcogen composition, intercalant composition, or both—making this an ideal system for studying composition-structure-function relationships. Although a variety of PCP compositions have been successfully synthesized using a various approaches,[24,27,38–44] efforts to elucidate the effect of chalcogen composition on their charge transport properties and electrochemical performance remain scarce.

Herein we report the synthesis of potassium-intercalated PCP chalcogenides ($K_2Mo_6X_6$; X = S, Se, Te) through rapid (10 min) microwave-assisted solid-state heating and investigate their charge-storage and electron-transfer properties as a function of changing chalcogen composition. Changes in growth kinetics and charge transport properties are correlated with anion composition in $K_2Mo_6S_6$ (S-PCP), $K_2Mo_6Se_6$ (Se-PCP), and $K_2Mo_6Te_6$ (Te-PCP) based on the results of our integrated microscopic, spectroscopic, and electroanalytical investigation. We highlight interesting performance trends in proton reduction electrocatalysis that scale directly with anion electronegativity and propose some additional elucidative

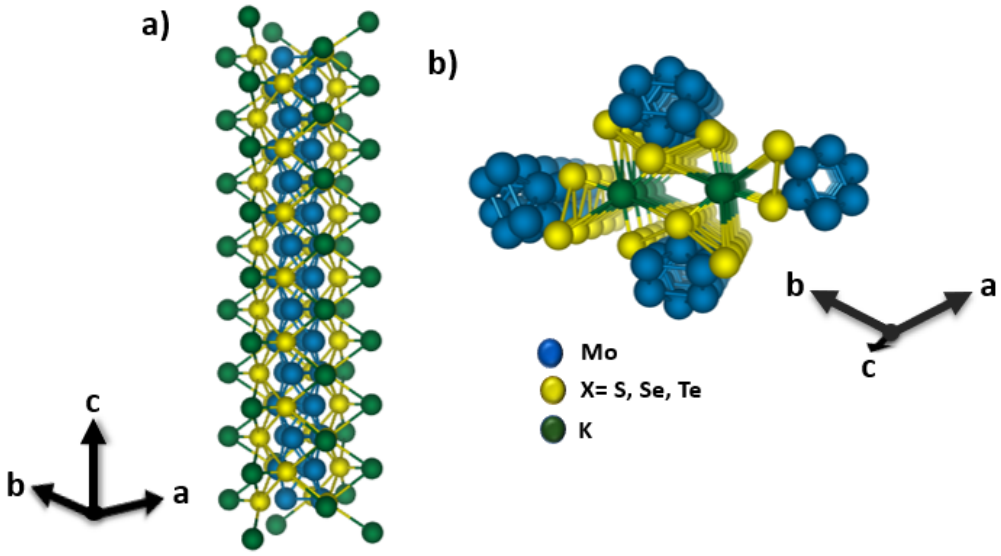

Figure 3.1. Structure of $K_2Mo_6X_6$ depicting the 1-dimensional growth along the *c*-axis with potassium surrounding the Mo_6X_6 unit (a). These elongated units adjoin to form hexagonal channels which are occupied by potassium (b).

spectroscopic and computational studies that will further support evolving design principles for these types of multinary chalcogenide compositions.

Experimental Section

Chemicals and Materials

MoS_2 powder (>95% purity, ~325 mesh) and $MoSe_2$ powder (99.999%, ~200 mesh) were used as purchased from Alfa Aesar. Mo powder (99.995%, ~250 mesh), graphite rods (~99.995%) Te powder (99.8%, ~200 mesh), K ingot (99.95%), graphite powder (<20μm) and concentrated H_2SO_4 acid (ACS grade) were used as purchased from Sigma Aldrich. K_2S (>95%) was used as purchased from Pfaltz and Bauer. Al_2O_3 microfiber was used as purchased from Thermo Fisher Scientific. Fused quartz tubes were purchased from AdValue Technology and made into round-bottom tubes with an in-house oxy-hydrogen torch. Gas diffusion media (GDL 28BC) was purchased from Ion Power. Ag/AgCl reference electrodes were purchased through ALS Japan. Selemion anion exchange membrane was purchased from AGC Engineering and stored in ultra-pure deionized water prior to use in electrochemical experiments. Ultra-pure water (18.2 MΩ) was obtained with a Barnstead E-Pure filtration system.

Catalyst Synthesis

The PCPs studied here were synthesized via high-temperature microwave-assisted solid-state heating as described in our previous work.[27] Briefly, stoichiometric amounts of precursors required to achieve a stoichiometry of $K_2Mo_6X_6$; X = S, Se, Te composition were weighed in a N_2 glovebox and ball milled under N_2 to homogenize. K_2S was used as the potassium source for the PCP sulfide due to its granular nature which facilitated the weighing process, while metallic potassium was used for the selenide and telluride phases owing to its high purity and the relative rarity of commercially available K_2Se and K_2Te. The resulting mixed precursor powders were then returned to a N_2 glovebox and pressed into pellets using a hydraulic press (Across International 40-ton cold press). Pellets were placed in round-bottom quartz tubes and

packed under N_2 using layers of Al_2O_3 microfiber and graphite. Samples were then removed from the glovebox and transferred to a graphite bath inside an alumina crucible and were irradiated in an Ar-filled conventional microwave with inverter technology (Toshiba ML2EM45PAESS; 1250W). The heating power was adjusted appropriately to maintain a temperature of ~750°C for 10 min, which was sufficient for synthesizing pure-phase PCPs in far less time than conventional solid-state methods.[24] Samples were then rapidly quenched in room temperature water after the heating time.

Structural and Electronic Characterization

PCP crystal structures were evaluated via Powder X-ray Diffraction (PXRD) using a Bruker D8 Advance diffractometer with Cu K-alpha radiation (1.541 Å). Experimental lattice parameters were obtained through Pawley refinement using the TOPAS suite from Bruker. Morphology was evaluated via scanning electron microscopy (SEM) using an FEI Nova NanoSEM430, and bulk composition was analyzed via energy-dispersive X-ray spectroscopy (EDX) using an FEI Scios Dual Beam FIB/SEM with an Oxford EDX detector. Surface composition was analyzed via X-ray photoelectron spectroscopy (XPS) using a Kratos Supra Axis spectrometer with an Al anode (1486.6 eV). STEM was performed using an Aberration- Corrected JEOL JEM-2100F. Images were acquired using an accelerating voltage of 200kV. Raman spectra were recorded using a Renishaw Confocal Raman Microscope equipped with a 1800 lines/mm grating and 785 nm laser.

Electrochemical Characterization

Electrochemical measurements were performed using a Bio-Logic VSP-300 potentiostat in a three-electrode H-cell configuration in which the counter and working electrode were separated by a Selemion ion exchange membrane. All measurements were taken in an aqueous H_2-sparged 0.5M H_2SO_4 electrolyte, with a Ag/AgCl (3M NaCl) reference electrode and graphite rod counter electrode. Potentials were converted to RHE scale using the following equation:

$$E_{RHE} = E(Ag/AgCl) + 0.210 + 0.059 \times pH$$

Working electrodes were prepared by depositing 15uL of PCP ink onto a 1 × 2 cm microporous layer carbon paper followed by drying under vacuum overnight. Deposited inks consisted of the appropriate PCP powder, conductive carbon black to improve electrical connectivity, polytetrafluoroethylene (PTFE) suspension as a binding agent, and isopropyl alcohol as a solvent. Inks were sonicated for 20 min prior to being drop cast onto the carbon paper. Blank electrodes were prepared as controls through the same method albeit without including any PCP powder. The H_2SO_4 electrolyte was de-oxygenated prior to each experiment by purging with H_2 for ∼30 minutes.

Specific capacitance measurements were made via cyclic voltammetry (CV) in a static solution by sweeping the potential across a non-Faradaic region (~100mV potential window centered around the open-circuit potential) at progressively increasing scan rates. A plot of charging current as a function of scan rate yields a linear response, from which per-gram specific capacitance is obtained by dividing slope by electrode mass loading. Subsequently, proton reduction behavior was evaluated via linear sweep voltammetry (LSV) at a scan rate of 5mV/s under vigorous stirring to mitigate mass transport limitations. Charge-transfer resistance was measured via electrochemical impedance spectroscopy (EIS) at different applied potentials, with a superimposed AC bias oscillating at frequencies ranging from 1 MHz to 1 Hz with a 10 mV sinus amplitude. Charge-transfer resistance is taken as the difference between x-intercepts of the resulting semi-circular Nyquist impedance plots.

Results and Discussion

We have expanded our previously reported synthetic protocol for inducing direct, solid-state nucleation of alkali-intercalated S-PCP[27] to the potassium-intercalated Se-PCP and Te-PCP studied here. Fig. 3.2a-c shows the morphologies that were obtained through our template-free microwave-assisted approach, while the PXRD patterns for each phase are depicted in Fig. 3.2d-f below each corresponding SEM image. An agglomeration of the crystalline structures is observed which is typical of template-free synthesis

approaches for PCPs due to intermolecular interactions between individual crystals.[27,45,46] High-resolution images of the one-dimensional structures are included in Fig. S3.1. Lattice parameters obtained through Pawley refinement of the PXRD patterns agree with the previously reported hexagonal crystal structure and $P6_3/m$ space group for each PCP (Fig. S3.2, Table S3.1). The unit cell parameters obtained from Pawley refinement show an expansion of the unit cell in all directions as a function of chalcogen (S<Se<Te). Fig. S3.3 shows the typical unit cell of PCPs, which makes it evident that the observed increases in the *a* and *b* lattice parameters as a function of chalcogen are associated with longer intercluster distances between Mo_6X_6. This in turn agrees with the observed left shift of the prominent (010) diffraction peak from S-PCP to Te-PCP (Fig. S3.4). Similarly, the expansion of the unit cell in the *c* direction is associated with an increase in the Mo-Mo and X-X intracluster distances. However, the smaller change in the *c* lattice parameter as a

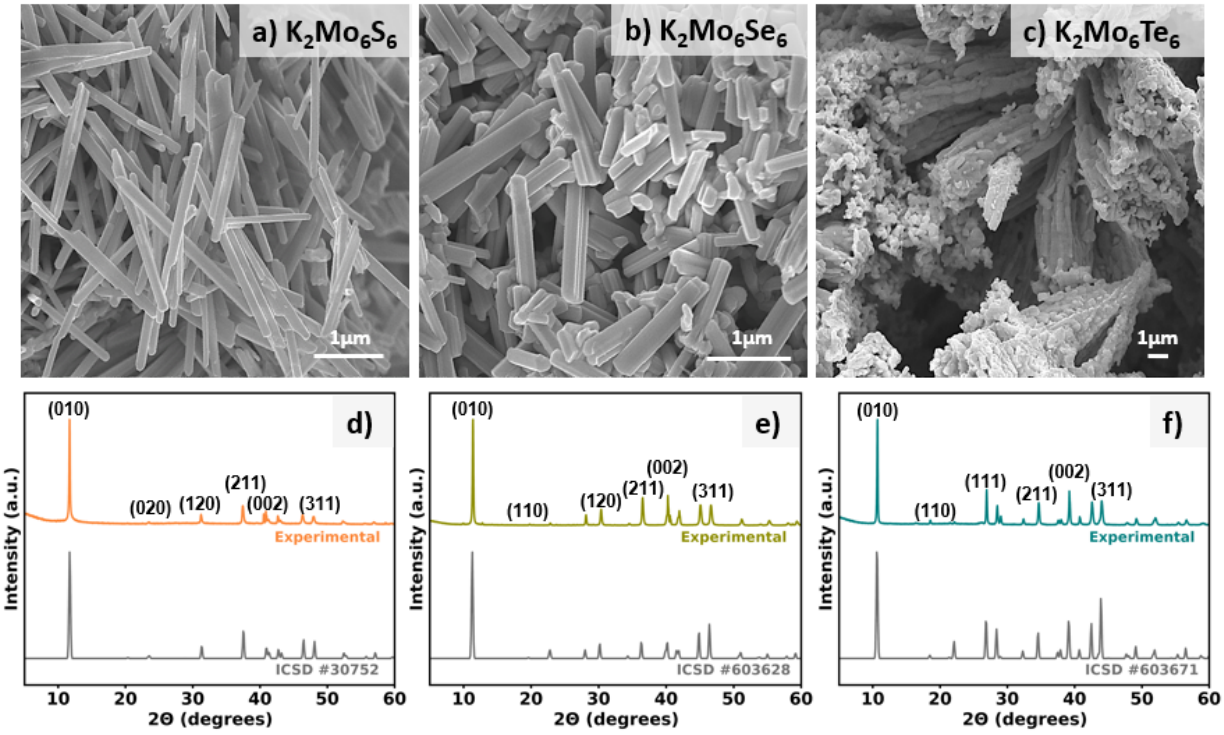

Figure 3.2. SEM micrographs for as-synthesized PCP sulfide (a) selenide (b) and telluride (c) along their corresponding PXRD patterns. Experimental diffractograms are overlaid with literature patterns from the International Crystal Structure Database (ICSD) for S-PCP (d), Se-PCP (e), and Te-PCP (f).

function of chalcogen corresponds to a more subtle change in intramolecular distances compared to intermolecular distances.[47]

The Raman spectra of PCP chalcogenides show similar vibrational modes for all of the materials studied (Fig. S3.5). As shown in Table S3.2, most of the Raman active modes calculated for PCPs are associated with vibrations that involve atoms in 6h Wyckoff positions (Mo, X). The similarity in Raman shift for all PCPs studied here, in conjunction with relatively small variations in Mo-Mo distances as a function of chalcogen could suggest that the observed Raman modes arise from Mo-Mo breathing modes, which have been assigned in previous literature. [43,44,48] Nevertheless, additional modeling is needed to deconvolute the corresponding Raman vibration modes. [43,44,48]All the PCPs evaluated exhibit pronounced one-dimensional growth, which agrees with the predominance of exposed {010} facets parallel to the hexagonal *c*-axis as observed via STEM (Fig. 3.3). This agrees with computational lattice energy calculations that were performed evaluated in our previous work for S-PCP [27], where facets parallel to the hexagonal axis had significantly lower surface energies relative to non-parallel surfaces (Table S3.3). Additional lattice planes observed for the synthesized PCP chalcogenides are included in Fig. S3.6-S3.7.

A significant morphology change is observed for Te-PCP compared to its sulfide and selenide analogues, as the telluride exhibits far less preferential one-dimensional growth. Fig. S3.7b shows a change in the exposed lattice from {010} to {001} within Te-PCP at ~45° angle. The change in exposed facets could be indicative of competing growth orientations, which may explain the less well-defined one-dimensional morphology of Te-PCP. However, the observed change in morphology could also stem from changes in potassium-chalcogen interactions, which have been identified to play a role in the distance between adjacent Mo_6X_6 chains in ternary PCPs. [24,49,50] Based on this theory, the repulsive $Mo_6X_6^{2-}$ chains are held together by ionic interactions with the ternary metal. As shown in Fig. S3.8 there is an overall increase in the Mo_6X_6—K bonds in Te-PCP compared to the S-PCP which could hinder the stabilization of the one-dimensional structure and lead to the less defined chains observed for Te-PCP.

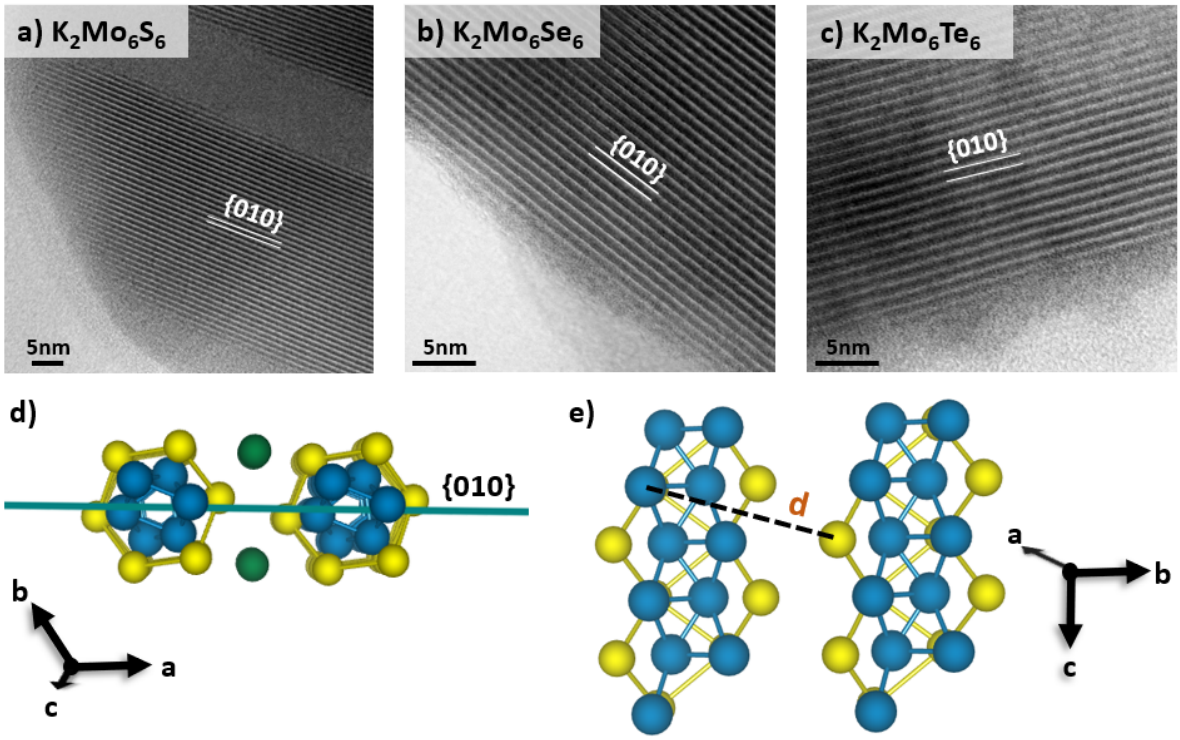

Figure 3.3. Bright-field STEM images for S-PCP (a) Se-PCP (b) and Te-PCP (c). The observed lattice d-spacing for each PCP corresponds to the Mo-X distance between adjacent one-dimensional clusters along the {010} family of planes (d, e).

Bulk PCP compositions were confirmed by EDX, where no impurities were identified for any material studied (Fig. S3.9). Similar results were obtained through XPS measurements, where only the corresponding elements, a native oxide layer, and adventitious carbon were identified at the surface of each PCP studied (Fig. S3.10-S3.12). The atomic percentages obtained by EDX for Se-PCP and Te-PCP agree with the expected 1:1 molybdenum to chalcogen ratio. For S-PCP, the Mo L- and S K-edges overlap, convoluting quantitative determination of Mo and S. Hence, reported atomic percentages appear to deviate significantly from expected values. Potassium quantification via EDX point scans yields atomic percent compositions between 12.31-12.98%, which is in good statistical agreement with a nominal composition of $K_2Mo_6S_6$.

Voltametric characterization of the materials in their respective non-Faradaic regions shows that their specific capacitance is chalcogen dependent and increases substantially as the electronegativity of the

chalcogen increases. S-PCP exhibited the highest ability to store charge, with a specific capacitance of 10.28 ± 0.89 F g^{-1}, compared to Se-PCP and Te-PCP at 4.20 ± 1.03 F g^{-1} and 2.25 ± 0.42 F g^{-1}, respectively (Fig. 3.4). The electrochemical response of PCPs in scanning from a non-Faradaic to a Faradaic region was evaluated via EIS under progressively more reductive potentials. Fig. 3.5 shows the Nyquist plot for each PCP acting as the working electrode material. A double-layer charging response is observed at low potentials as evidenced by the lack of an observable second x-axis intercept, while single-electron charge-transfer events along the proton reduction reaction mechanism are observable by the semicircular Nyquist plots from -0.2V to -0.6V vs RHE. These semicircular Nyquist plots also indicate that interfacial electron-transfer is modellable by a simple Randle's circuit involving a double-layer capacitive element, charge transfer resistance element, and a circuit resistance element (Fig. S3.13).

Shown in the inset of Fig. 3.5a, individual S-PCP Nyquist plots at each negative potential are characterized by a small potential-independent semicircle at high frequencies (left semicircle) and a larger, potential-dependent semicircle at low frequencies (right semicircle). The potential-independent semicircle is associated with resistance at the interface between the carbon paper electrode and the PCP layer.[51,52] This

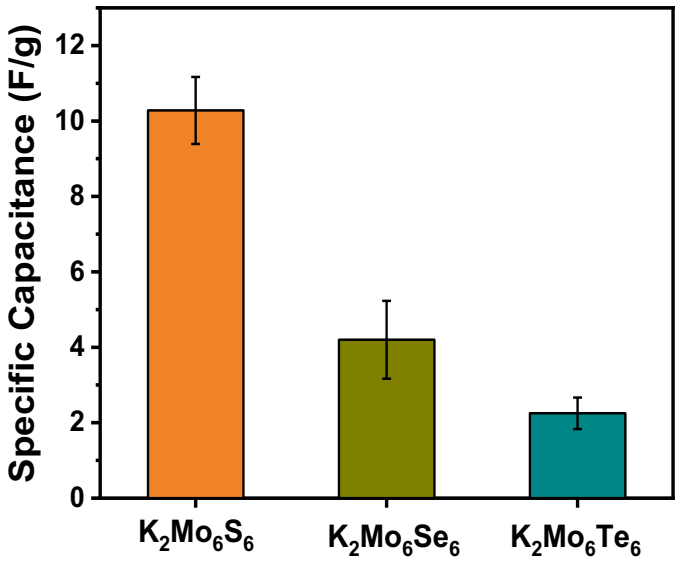

Figure 3.4. Specific capacitance per gram of each PCP studied.

potential-independent semicircle is less pronounced for Se-PCP and Te-PCP (Fig. 3.5b-c) which indicates better contact between the electrode, which may be a result of their increased lateral thickness. The potential-dependent semicircle is characteristic of a charge-transfer process.[53] An increase in the ability to transfer charge to adsorbed H^* is observed for all PCPs at more reductive potentials, which is expected since surface electrons are more energetic under these conditions and are therefore more likely to transfer to unoccupied orbitals of the adsorbed species. Fig. 3.5d shows the charge transfer resistance (R_{ct}) of all PCPs at different potentials. The R_{ct} of all PCPs decreased as the reductive potential was increased from -0.4 to -0.6 vs RHE, decreasing from 1.77 to 1.16Ω for S-PCP, 6.18 to 2.16Ω for Se-PCP and 10.2 to 3.7Ω for Te-PCPC. S-PCP shows the highest tendency to reduce protons, evidenced by its lower R_{ct} compared to Se-PCP and Te-PCP at every potential evaluated. This trend in R_{ct} may result from a gradual metal–to–semiconductor transition for PCPs as chalcogen electronegativity decreases, as has been computationally

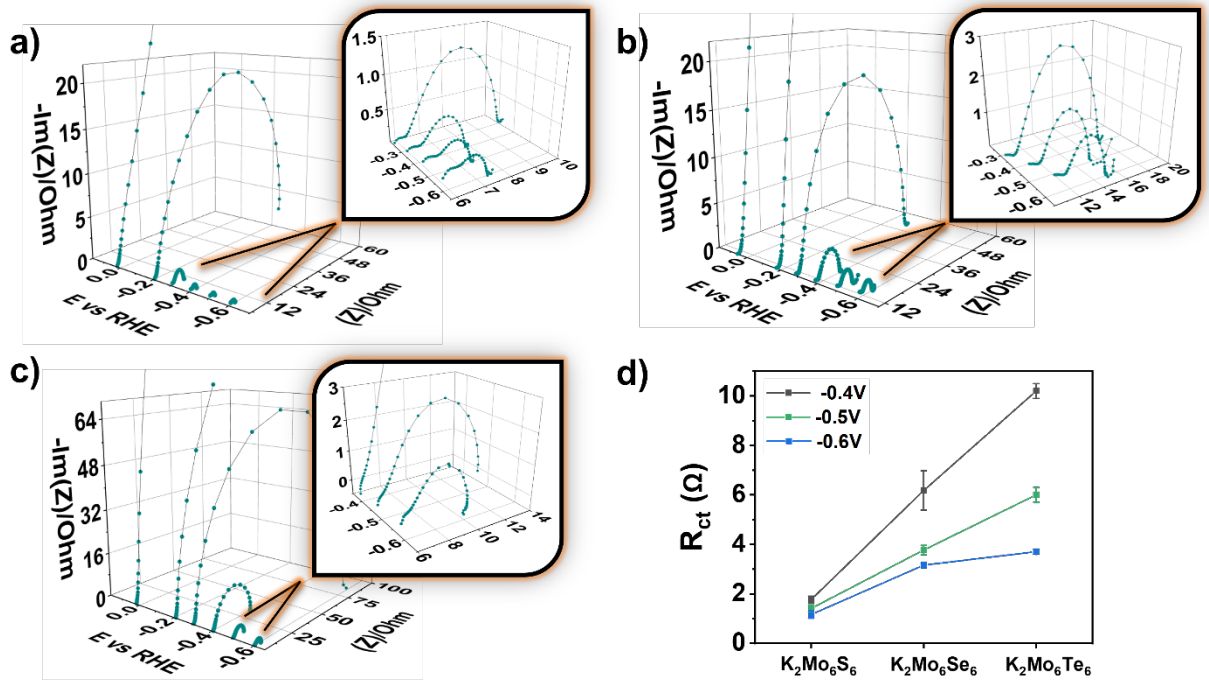

Figure 3.5. Nyquist plot for S-PCP(a), Se-PCP(b) and Te-PCP(c) at different potentials in a 0.5 M H_2SO_4 solution. Charge transfer resistance for proton reduction over all three PCPs studied, extracted from Nyquist plots (d).

predicted.[54,55] In other words, intrinsic electrical conductivity differences between S-PCP, Se-PCP, and Te-PCP appear to contribute significantly to the observed interfacial reactivity for proton reduction.

R_{ct} values correlate with the lower onset potential of S-PCP to generate H_2 which is shown in Fig. 3.6a. A steady increase in the overpotential required to achieve a current density of 10 mA cm^{-2} is observed, across the series of alkali-intercalated PCPs, with overpotentials of 203.3 mV, 316.8 mV, and 347.9 mV for S-PCP, Se-PCP, and Te-PCP respectively. Tafel slope analysis (Fig. 3.6b) suggest that all PCPs follow a Volmer-Heyrovsky mechanism where electrochemical desorption via proton-coupled electron transfer is the final step toward H_2 production.[56] Interestingly, the trend in increasing proton reduction activity for the PCPs studied here as chalcogen electronegativity increases is similar to that obtained by evaluating the proton adsorption stabilization in binary Mo_6X_8 (X = S, Se, Te) Chevrel-Phases in our previous work,[11] which indicates that a similar H^* adsorption configuration at Mo-X bridging sites may be stable within the PCPs framework. Combining computation with experimentation in our previous work on binary Chevrel-Phases, we showed that a more electronegative chalcogen stabilizes H^* adsorption more effectively due to improved X-H orbital overlap interactions which is likely to apply to PCP chalcogenides as well.

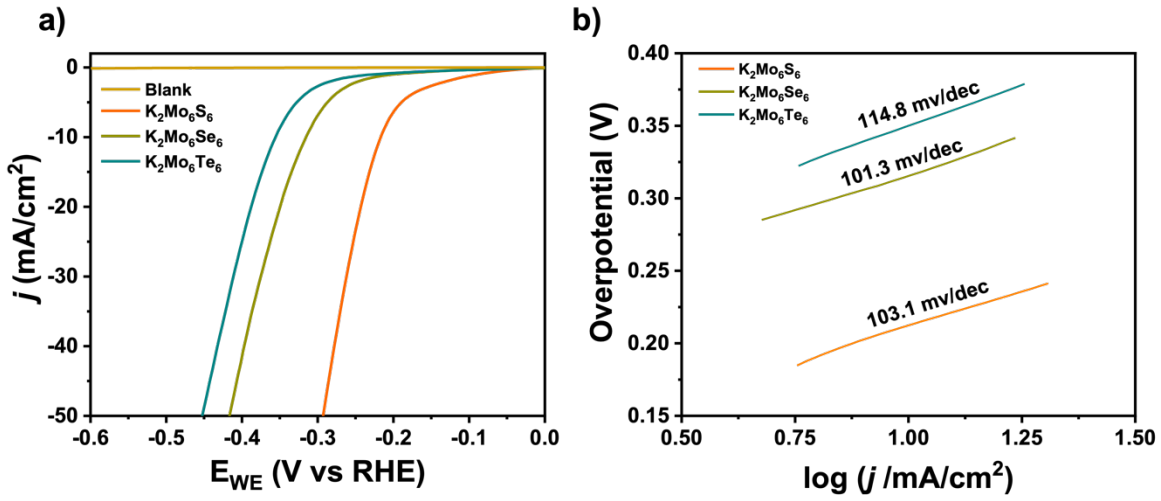

Figure 3.6. Polarization curves for PCP electrodes in 0.5 M H_2SO_4, along a blank for comparison (a). Tafel plots for PCP chalcogenides illustrating the current–potential response of each ink acting as a catalyst for proton reduction (b).

Considering the observable change in PCP morphology from a well-defined 1D sulfide to a pseudo-3D telluride, the observed trend changes in proton reduction activity could also be associated with a decrease in the relative number of exposed active sites per unit of exposed surface area. Hence, it will be beneficial to pinpoint the adsorption position of H* on each PCP so that exact active site densities per unit area can be compared. However, this will require a detailed computational analysis across several surface facets that also incorporates biasing and solvation effects to ascertain adsorption geometries and energetics; therefore, such an analysis is excluded from the present work.

The results of EIS are consistent with the observed performances of each PCP as a proton reduction electrocatalyst, indicating that charge transfer is a critical factor determining their interfacial reactivity. While S-PCP is the most promising electrocatalyst from an energy-input perspective (203.3 mV overpotential), the higher interfacial R_{ct} value observed for Te-PCP (3.7 Ω at -0.6V vs RHE) makes this composition more promising as an aqueous capacitor or as a component in systems wherein aqueous hydrogen generation is undesirable.

Conclusion

In this work, we report the expansion of microwave-assisted solid-state synthesis to one-dimensional selenide- and pseudo three-dimensional telluride-based PCP chalcogenides. Template-free preferential growth exposing the {010} surface was observed for all three ternary compositions studied, while chalcogen-dependent morphology changes are explained by the observation of competitive stabilization of {010} and {001} facets in the Te-PCP, as well as the reduction of chalcogen-potassium interactions in telluride PCPs. The double-layer capacitance, charge transfer resistance, and proton reduction reactivity of three potassium-intercalated PCP chalcogenides were all quantified in this work. The sulfide PCP displayed the highest charge storage capacity as well as faster charge-transfer behavior during proton reduction. Decreases in charge storage capacities and R_{ct} were observed as the electronegativity of the chalcogen

decreased, which agrees well with previous surface-proton interactions over analogous Chevrel-Phase materials.[11] In future studies of this interesting one-dimensional system to elucidate electronic versus morphological driving forces for proton reduction, fine control of particle size and shape should be coupled with a rigorous computational evaluation of surface-proton interactions. A similarly rigorous interrogation of surface-localized electronic states in each PCP structure during electrochemical analysis via ex-situ and operando X-ray absorption spectroscopy will also illuminate the nature frontier orbitals that contribute to H^* adsorption and reduction. These avenues of future studies will compound on the composition-structure-function relationships discussed herein and will potentially unravel novel reactivity in this underexplored, dimensionally reduced chalcogenide composition space.

Supporting Information

High resolution SEM micrographs for all three PCP chalcogenides, Pawley refinement for PCPs along lattice parameters obtained from refinement, PCP chalcogenides unit cell, Changes in 2θ values for the diffraction peak in the (010) plane for PCP chalcogenides, Raman spectra of PCP chalcogenides, Additional STEM for PCP chalcogenides, PCPs unit cell showing the changes in X-K and K-K distances as a function of chalcogen, EDS/XPS spectra for all PCP chalcogenides, Randle's circuit used to interpret the Nyquist plots of all three PCP chalcogenides, Raman active modes for the space group P63/m (No. 176) (PDF).

Acknowledgment

We would like to thank the University of California, Davis for start-up funding, as well as support from the Cottrell Scholar program supported by the Research Corporation for Science Advancement (RCSA 26780). JMV also acknowledges funding support from the NSF through the Faculty Early Career Development Program (DMR-2044403). JOR was funded by the National Science Foundation Graduate Research Fellowship (NSF 1650042). Part of this work was performed at the Stanford Nano Shared Facilities (SNSF)/Stanford Nanofabrication Facility (SNF), supported by the National Science Foundation under award

ECCS-1542152. XPS analysis at UC Davis was supported by the National Science Foundation (DMR-1828238). We gratefully acknowledge Brian Wuille Bille for assisting in the preparation of TEM grids and acquisition of Raman spectra for all PCP chalcogenides. We thank Andrew Thron for the acquisition of STEM images.

Publication Information, Copyright, and Author Acknowledgements

This chapter forms the basis for the following publication:

Ortiz-Rodríguez, J.C.; Perryman, J.T.; Velázquez, J.M.*, Charge transport dynamics in microwave synthesized one-dimensional molybdenum chalcogenides, *Industrial & Engineering Chemistry Research*, 2021, 60 (45) 16153–16161. https://pubs.acs.org/doi/10.1021/acs.iecr.1c02825

Jessica C. Ortiz-Rodríguez conducted material synthesis, electrochemistry experiments, PXRD, SEM and EDX. JTP contributed to material synthesis as well as XPS acquisition and processing.

Reference

(1) Davis, S. J.; Lewis, N. S.; Shaner, M.; Aggarwal, S.; Arent, D.; Azevedo, I. L.; Benson, S. M.; Bradley, T.; Brouwer, J.; Chiang, Y. M.; Clack, C. T. M.; Cohen, A.; Doig, S.; Edmonds, J.; Fennell, P.; Field, C. B.; Hannegan, B.; Hodge, B. M.; Hoffert, M. I.; Ingersoll, E.; Jaramillo, P.; Lackner, K. S.; Mach, K. J.; Mastrandrea, M.; Ogden, J.; Peterson, P. F.; Sanchez, D. L.; Sperling, D.; Stagner, J.; Trancik, J. E.; Yang, C. J.; Caldeira, K. Net-Zero Emissions Energy Systems. *Science* 2018, *360* (6396), eaas9793.

(2) She, Z. W.; Kibsgaard, J.; Dickens, C. F.; Chorkendorff, I.; Nørskov, J. K.; Jaramillo, T. F. Combining Theory and Experiment in Electrocatalysis: Insights into Materials Design. *Science* 2017, *355* (6321), eaad4998.

(3) Soriaga, M. P.; Baricuatro, J. H.; Cummins, K. D.; Kim, Y. G.; Saadi, F. H.; Sun, G.; McCrory, C. C. L.; McKone, J. R.; Velazquez, J. M.; Ferrer, I. M.; Carim, A. I.; Javier, A.; Chmielowiec, B.; Lacy, D. C.; Gregoire, J. M.; Sanabria-Chinchilla, J.; Amashukeli, X.; Royea, W. J.; Brunschwig, B. S.; Hemminger, J. C.; Lewis, N. S.; Stickney, J. L. Electrochemical Surface Science Twenty Years Later: Expeditions into the Electrocatalysis of Reactions at the Core of Artificial Photosynthesis. *Surf. Sci.* 2015, *631*, 285–294.

(4) Wang, C.; Liu, D.; Lin, W. Metal-Organic Frameworks as a Tunable Platform for Designing Functional Molecular Materials. *J. Am. Chem. Soc.* 2013, *135* (36), 13222–13234.

(5) Singstock, N. R.; Ortiz-Rodríguez, J. C.; Perryman, J. T.; Sutton, C.; Velázquez, J. M.; Musgrave, C. B. Machine Learning Guided Synthesis of Multinary Chevrel Phase Chalcogenides. *J. Am. Chem. Soc.* 2021, *143* (24), 9113–9122.

(6) Levi, E.; Aurbach, D. Chevrel Phases, MxMo6T8 (M = Metals, T = S, Se, Te) as a Structural Chameleon: Changes in the Rhombohedral Framework and Triclinic Distortion. *Chem. Mater.* 2010, *22* (12), 3678–3692.

(7) Jiao, Y.; Zheng, Y.; Davey, K.; Qiao, S. Z. Activity Origin and Catalyst Design Principles for Electrocatalytic Hydrogen Evolution on Heteroatom-Doped Graphene. *Nat. Energy* 2016, *1*, 16130.

(8) Koper, M. T. M. Thermodynamic Theory of Multi-Electron Transfer Reactions: Implications for Electrocatalysis. *J. Electroanal. Chem.* 2011, *660* (2), 254–260.

(9) Peng, Y.; Lu, B.; Wang, N.; Li, L.; Chen, S. Impacts of Interfacial Charge Transfer on Nanoparticle Electrocatalytic Activity towards Oxygen Reduction. *Phys. Chem. Chem. Phys.* 2017, *19* (14), 9336–9348.

(10) Göttle, A. J.; Koper, M. T. M. Proton-Coupled Electron Transfer in the Electrocatalysis of CO2 Reduction: Prediction of Sequential vs. Concerted Pathways Using DFT. *Chem. Sci.* 2016, *8* (1), 458–465.

(11) Ortiz-Rodríguez, J. C.; Singstock, N. R.; Perryman, J. T.; Hyler, F. P.; Jones, S. J.; Holder, A. M.; Musgrave, C. B.; Velázquez, J. M. Stabilizing Hydrogen Adsorption through Theory-Guided Chalcogen Substitution in Chevrel-Phase Mo6X8(X=S, Se, Te) Electrocatalysts. *ACS Appl. Mater. Interfaces* 2020, *12* (32), 35995–36003.

(12) Manzeli, S.; Ovchinnikov, D.; Pasquier, D.; Yazyev, O. V.; Kis, A. 2D Transition Metal Dichalcogenides. *Nat. Rev. Mater.* 2017, *2*, 17033.

(13) Huang, W.; Gan, L.; Li, H.; Ma, Y.; Zhai, T. 2D Layered Group IIIA Metal Chalcogenides: Synthesis, Properties and Applications in Electronics and Optoelectronics. *CrystEngComm* 2016, *18* (22), 3968–3984.

(14) Heine, T. Transition Metal Chalcogenides: Ultrathin Inorganic Materials with Tunable Electronic Properties. *Acc. Chem. Res.* 2015, *48*, 65–72.

(15) Shang, C.; Fu, L.; Zhou, S.; Zhao, J. Atomic Wires of Transition Metal Chalcogenides: A Family of 1D Materials for Flexible Electronics and Spintronics. *J. Am. Chem. Soc. Au* 2021, *1* (2), 147–155.

(16) Han, S. A.; Bhatia, R.; Kim, S. W. Synthesis, Properties and Potential Applications of Two-Dimensional Transition Metal Dichalcogenides. *Nano Converg.* 2015, *2* (17), 1–14.

(17) Voiry, D.; Shin, H. S.; Loh, K. P.; Chhowalla, M. Low-Dimensional Catalysts for Hydrogen Evolution and CO2 Reduction. *Nat. Rev. Chem.* 2018, *2* (1), 0105.

(18) Tang, Z.; Yang, H. Transition Metal Chalcogenides for Energy Storage and Conversion. In *Advanced Nanomaterials for Electrochemical-Based Energy Conversion and Storage*; Ran, F., Chen, S., Eds.; Elsevier, 2019; pp 355–391.

(19) Zhang, Y.; Zhou, Q.; Zhu, J.; Yan, Q.; Dou, S. X.; Sun, W. Nanostructured Metal Chalcogenides for Energy Storage and Electrocatalysis. *Adv. Funct. Mater.*2017, *27* (35), 1702317.

(20) Fu, Q.; Han, J.; Wang, X.; Xu, P.; Yao, T.; Zhong, J.; Zhong, W.; Liu, S.; Gao, T.; Zhang, Z.; Xu, L.; Song, B. 2D Transition Metal Dichalcogenides: Design, Modulation, and Challenges in Electrocatalysis. *Adv. Mater.* 2021, *33* (6), 1907818.

(21) Perryman, J. T.; Ortiz-Rodrıguez, J. C.; Jude, J. W.; Hyler, F. P.; Davis, R. C.; Mehta, A.; Kulkarni, A. R. Metal-Promoted Mo6S8 Clusters: A Platform for Probing Ensemble Effects on the Electrochemical Conversion of CO2 and CO to Methanol. *Mater. Horiz.* 2020, *7*, 193–202.

(22) Zhang, Y.; Zhang, L.; Lv, T.; Chu, P. K.; Huo, K. Two-Dimensional Transition Metal Chalcogenides for Alkali Metal Ions Storage. *ChemSusChem* 2020, *13* (6), 1114–1154.

(23) Hu, Z.; Wu, Z.; Han, C.; He, J.; Ni, Z.; Chen, W. Two-Dimensional Transition Metal Dichalcogenides: Interface and Defect Engineering. *Chem Soc Rev* 2018, *47* (9), 3100–3128.

(24) Tarascon, J. M.; Hull, G. W.; DiSalvo, F. J. A Facile Synthesis of Pseudo One-Monodimensional Ternary Molybdenum Chalcogenides M2Mo6X6 (X = Se,Te; M = Li,Na..Cs). *Mater. Res. Bull.* 1984, *19* (7), 915–924.

(25) Tarascon, J. M. DiSalvo, F.J. and Waszczak, J. V. Physical Properties of Several M2Mo6X6 Compounds (M = GROUP IA METAL; X = Se, Te). *Solid State Commun.* 1984, *52* (3), 227–231.

(26) Hor, P. H.; Meng, R. L.; Chu, C. W.; Tarascon, J. M.; Wu, M. K. High Pressure Study on Quiasi-One-Dimensional Compounds M2Mo6X6. *Physica B* 1985, *135* (1), 245–247.

(27) Perryman, J. T.; Kulkarni, A. R.; Velázquez, J. M. Direct Solid-State Nucleation and Charge-Transport Dynamics of Alkali Metal-Intercalated M2Mo6S6(M = K, Rb, Cs) Nanorods. *J. Mater. Chem. C* 2020, *8* (31), 10742–10748.

(28) Machín, A.; Fontánez, K.; Arango, J. C.; Ortiz, D.; De León, J.; Pinilla, S.; Nicolosi, V.; Petrescu, F. I.; Morant, C.; Márquez, F. One-Dimensional (1d) Nanostructured Materials for Energy Applications. *Materials* 2021, *14* (10), 2609.

(29) Weng, B.; Liu, S.; Tang, Z. R.; Xu, Y. J. One-Dimensional Nanostructure Based Materials for Versatile Photocatalytic Applications. *RSC Advances* 2014, *4* (25), 12685–12700.

(30) Pantano, M. F.; Kuljanishvili, I. Advances in Mechanical Characterization of 1D and 2D Nanomaterials: Progress and Prospects. *Nano Express* 2020, *1* (2), 022001.

(31) Arrabito, G.; Aleeva, Y.; Ferrara, V.; Prestopino, G.; Chiappara, C.; Pignataro, B. On the Interaction between 1d Materials and Living Cells. *J. Funct. Biomater.* 2020, *11* (2), 40.

(32) Çakir, D.; Durgun, E.; Gülseren, O.; Ciraci, S. First Principles Study of Electronic and Mechanical Properties of Molybdenum Selenide Type Nanowires. *Phys. Rev. B Condens. Matter.* 2006, *74* (23), 235433.

(33) Golden, J. H.; DiSalvo, F. J.; Fréchet, J. M. J.; Silcox, J.; Thomas, M.; Elman, J. Subnanometer-Diameter Wires Isolated in a Polymer Matrix by Fast Polymerization. *Science* 1996, *273* (5276), 782–784.

(34) Chin, S. J.; Hornsby, P.; Vengust, D.; Mihailović, D.; Mitra, J.; Dawson, P.; Mcnally, T. Composites of Poly(ε-Caprolactone) and Mo 6S 3I 6 Nanowires. *Polym. Adv. Technol.* 2012, *23* (2), 149–160.

(35) Qi, X.; Osterloh, F. E. Chemical Sensing with LiMo3Se3 Nanowire Films. *J. Am. Chem. Soc.* 2005, *127* (21), 7666–7667.

(36) Majkić, A.; Gadermaier, C.; Celic, N.; Topolovsek, P.; Bratina, G.; Mihailovic, D. Mo6S9-XIx Nanowires as Additives for Enhanced Organic Solar Cell Performance. *Sol. Energy Mater. Sol. Cells* 2014, *127*, 63–66.

(37) Jin, K. H.; Liu, F. 1D Topological Phases in Transition-Metal Monochalcogenide Nanowires. *Nanoscale* 2020, *12* (27), 14661–14667.

(38) Zhu, H.; Wang, Q.; Zhang, C.; Addou, R.; Cho, K.; Wallace, R. M.; Kim, M. J. New Mo6Te6 Sub-Nanometer-Diameter Nanowire Phase from 2H-MoTe2. *Adv. Mater.* 2017, *29* (18), 1606264.

(39) Lin, J.; Cretu, O.; Zhou, W.; Suenaga, K.; Prasai, D.; Bolotin, K. I.; Cuong, N. T.; Otani, M.; Okada, S.; Lupini, A. R.; Idrobo, J. C.; Caudel, D.; Burger, A.; Ghimire, N. J.; Yan, J.; Mandrus, D. G.; Pennycook, S. J.; Pantelides, S. T.; Zhang, Y.; Zhou, W.; Pantelides, S. T.; Kibsgaard, J.; Tuxen, A.; Levisen, M.; Lægsgaard, E.; Gemming, S.; Seifert, G.; Lauritsen, J. V; Besenbacher, F.; Uplaznik, M.; Bercic, B.; Strle, J.; Ploscaru, M. I.; Dvorsek, D.; Kuar, P.; Devetak, M.; Vengust, D.; Podobnik, B.; Mihailovic, D. D. Flexible Metallic Nanowires with Self-Adaptive Contacts to Semiconducting Transition-Metal Dichalcogenide Monolayers. *Nanotechnology* 2014, *9* (20), 436–442.

(40) Liu, X.; Xu, T.; Wu, X.; Zhang, Z.; Yu, J.; Qiu, H.; Hong, J. H.; Jin, C. H.; Li, J. X.; Wang, X. R.; Sun, L. T.; Guo, W. Top-down Fabrication of Sub-Nanometre Semiconducting Nanoribbons Derived from Molybdenum Disulfide Sheets. *Nat. Commun.* 2013, *4*, 1776.

(41) Lin, J.; Zhang, Y.; Zhou, W.; Pantelides, S. T. Structural Flexibility and Alloying in Ultrathin Transition-Metal Chalcogenide Nanowires. *ACS Nano* 2016, *10* (2), 2782–2790.

(42) Le, D.; Sun, D.; Lu, W.; Aminpour, M.; Wang, C.; Ma, Q.; Rahman, T. S.; Bartels, L. Growth of Aligned Mo6S6 Nanowires on Cu(111). *Surf. Sci.* 2013, *611*, 1–4.

(43) Nagata, M.; Shukla, S.; Nakanishi, Y.; Liu, Z.; Lin, Y. C.; Shiga, T.; Nakamura, Y.; Koyama, T.; Kishida, H.; Inoue, T.; Kanda, N.; Ohno, S.; Sakagawa, Y.; Suenaga, K.; Shinohara, H. Isolation of Single-Wired Transition-Metal Monochalcogenides by Carbon Nanotubes. *Nano Lett.* 2019, *19* (8), 4845–4851.

(44) Yoo, Y.; Jeong, J. S.; Ma, R.; Koester, S. J.; Johns, J. E. Ultrathin One-Dimensional Molybdenum Telluride Quantum Wires Synthesized by Chemical Vapor Deposition. *Chem.Mater.* 2020, *32* (22), 9650–9655.

(45) Chae, S.; Oh, S.; Siddiqa, A. J.; Choi, K. H.; Lee, W. G.; Jang, W. S.; Lee, J. S.; Kim, Y. M.; Huh, J.; Kim, S. M.; Choi, J. Y. Highly Concentrated Single-Chain Atomic Crystal LiMo3Se3 Solution Using Ion-Exchange Chromatography. *Chem Comms* 2018, *54* (88), 12503–12506.

(46) Tarascon, J. M. Mo6Se6: A New Solid-State Electrode for Secondary Lithium Batteries. *J. Electrochem. Soc.* 1985, *132*, 2089–2092.

(47) Hönle, W.; Von Schnering, H. G.; Lipka, A.; Yvon, K. New Compounds with Infinite Chains of Face-Condensed Octahedral Mo6 Clusters: InMo3Se3, InMo3Te3, TlMo3Se3 and TlMo3Te3. *J. less-common met.* 1980, *71* (1), 135–145.

(48) Yu, Y.; Wang, G.; Tan, Y.; Wu, N.; Zhang, X. A.; Qin, S. Phase-Controlled Growth of One-Dimensional Mo6Te6 Nanowires and Two-Dimensional MoTe2 Ultrathin Films Heterostructures. *Nano Lett.* 2018, *18* (2), 675–681.

(49) Chevrel, R.; Gougeon, P.; Potel, M.; Sergent, M. Ternary Molybdenum Chalcogenides: A Route to New Extended Clusters. *J. Solid State Chem.* 1985, *57* (1), 25–33.

(50) Jeon, J.; Oh, S.; Choi, K. H.; Chae, S.; Woo, C.; Dong, X.; Asghar, G.; Ahn, J.; Kim, T. Y.; Ali, J.; Yu, H. K.; Choi, J.-Y. Synthesis of One-Dimensional Atomic Chain LiMo3Se3 through Ion-Exchange Reaction from InMo3Se3: Kinetics and Thermodynamics. *Ceram. Int.* 2021, No. May, 1–5.

(51) Murthy, A. P.; Theerthagiri, J. Highly Active MoS2/Carbon Electrocatalysts for the Hydrogen Evolution Reaction – Insight into the Effect of the Internal Resistance and Roughness Factor on the Tafel Slope. *Phys. Chem. Chem. Phys* 2017, *19*, 1988–1998.

(52) Vrubel, H.; Moehl, T.; Grätzel, M.; Hu, X. Revealing and Accelerating Slow Electron Transport in Amorphous Molybdenum Sulphide Particles for Hydrogen Evolution Reaction. *Chem Comm* 2013, *49* (79), 8985–8987.

(53) Mei, B. A.; Lau, J.; Lin, T.; Tolbert, S. H.; Dunn, B. S.; Pilon, L. Physical Interpretations of Electrochemical Impedance Spectroscopy of Redox Active Electrodes for Electrical Energy Storage. *J. Phys. Chem. C* 2018, *122* (43), 24499–24511.

(54) Çakir, D.; Durgun, E.; Gülseren, O.; Ciraci, S. First Principles Study of Electronic and Mechanical Properties of Molybdenum Selenide Type Nanowires. *Phys. Rev. B Condens. Matter* 2006, *74* (23), 1–8.

(55) Zhang, W.; Wang, J.; Zhao, L.; Wang, J.; Zhao, M. Transition-Metal Monochalcogenide Nanowires: Highly Efficient Bi-Functional Catalysts for the Oxygen Evolution/Reduction Reactions. *Nanoscale* 2020, *12* (24), 12883–12890.

(56) Zeng, M.; Li, Y. Recent Advances in Heterogeneous Electrocatalysts for the Hydrogen Evolution Reaction. *J. Mater. Chem. A* 2015, *3* (29), 14942–14962.

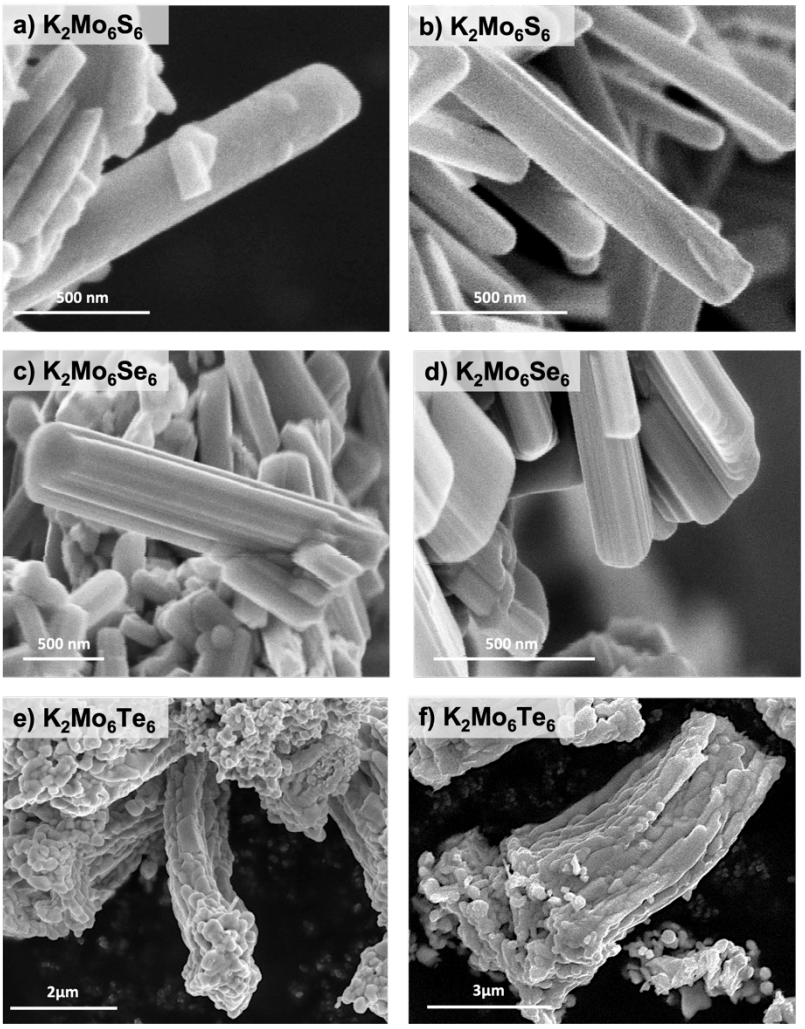

Figure S3.1. High-resolution SEM micrographs for as-synthesized PCP sulfide (a,b) selenide (c,d) and telluride (e,f).

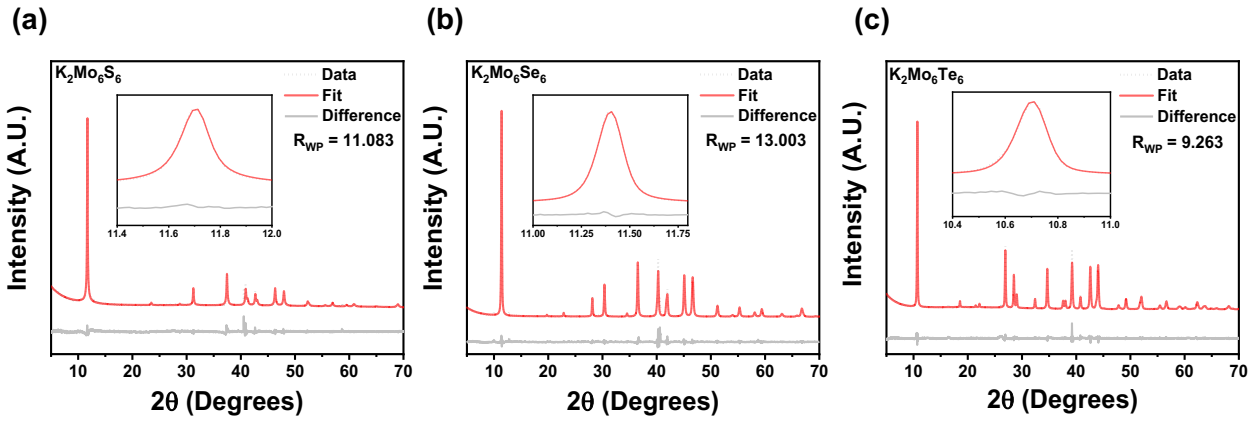

Figure S3.2. PXRD patterns used for Pawley refinement (dotted line), along with their calculated patterns (red line) and the difference curve (grey line) for S-PCP (a) Se-PCP (b) and Te-PCP (c). Lattice parameters obtained through refinement are included in Table S1.

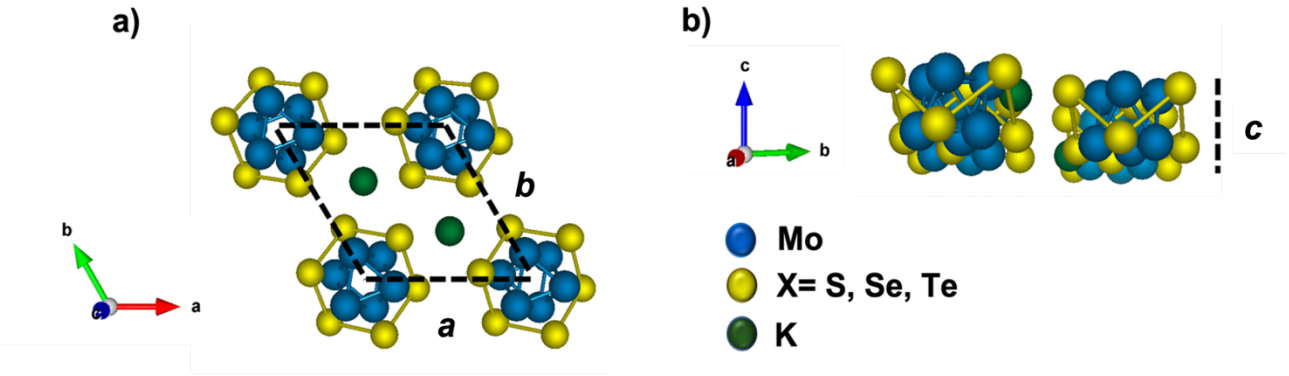

Figure S3.3. Unit cell of PCP chalcogenides depicting the horizontal (a) and vertical (b) lattice parameters. The corresponding values for the lattice parameters obtained by Pawley refinement are shown in Table S3.1.

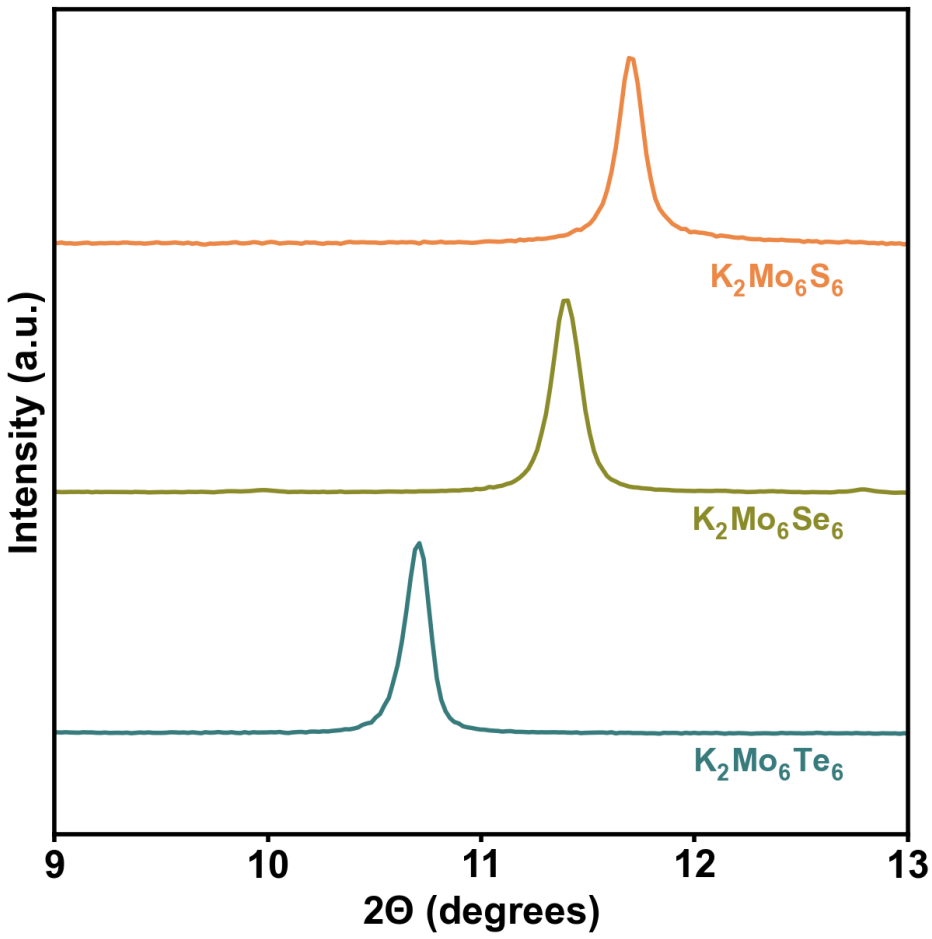

Figure S3.4. Changes in 2θ values for the diffraction peak in the (010) plane for PCPs as a function of chalcogen.

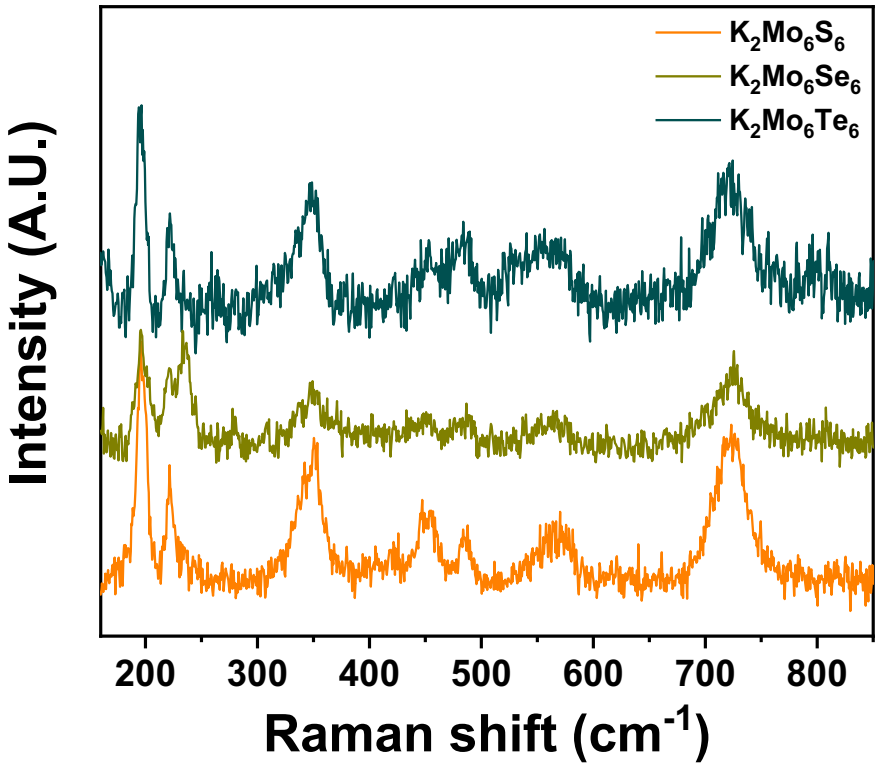

Figure S3.5. Raman spectra of PCP chalcogenides.

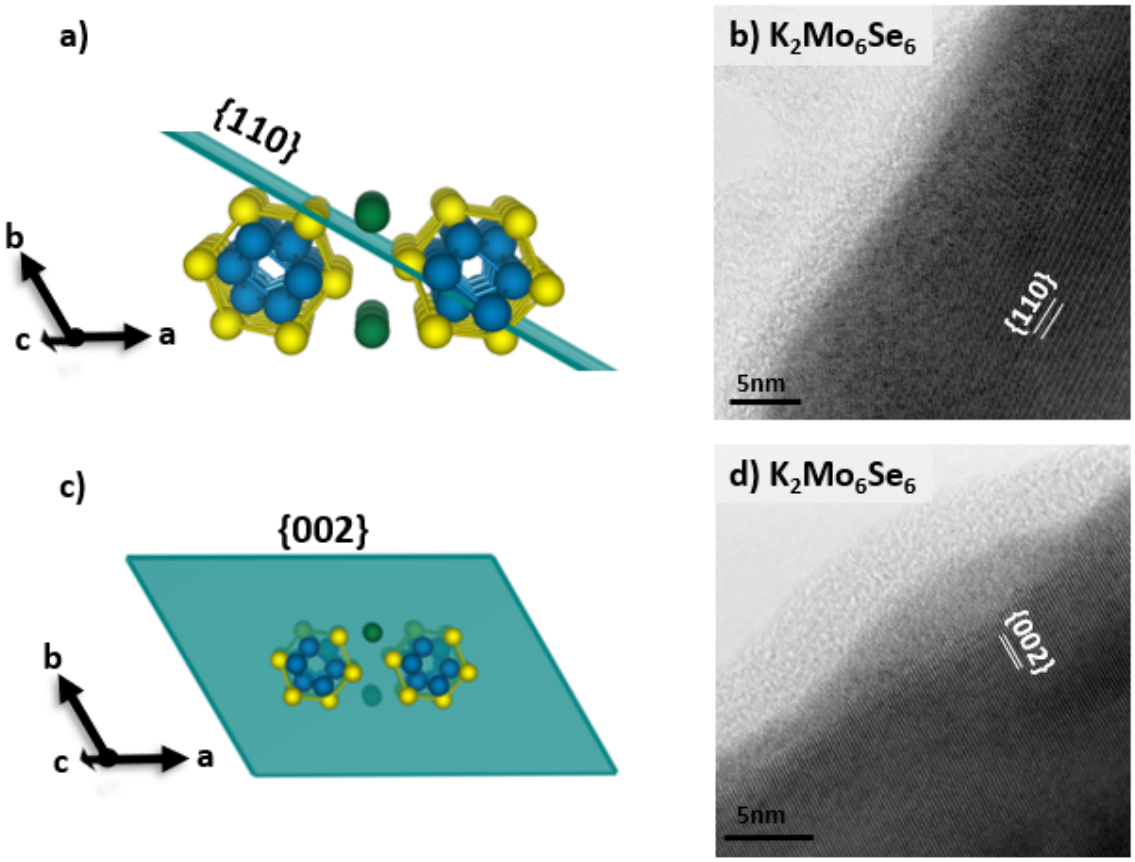

Figure S3.6. Visualization of the {110} and {002} planes for Se-PCP (a,c) along the bright-field STEM images associated to the respective plane (b,d).

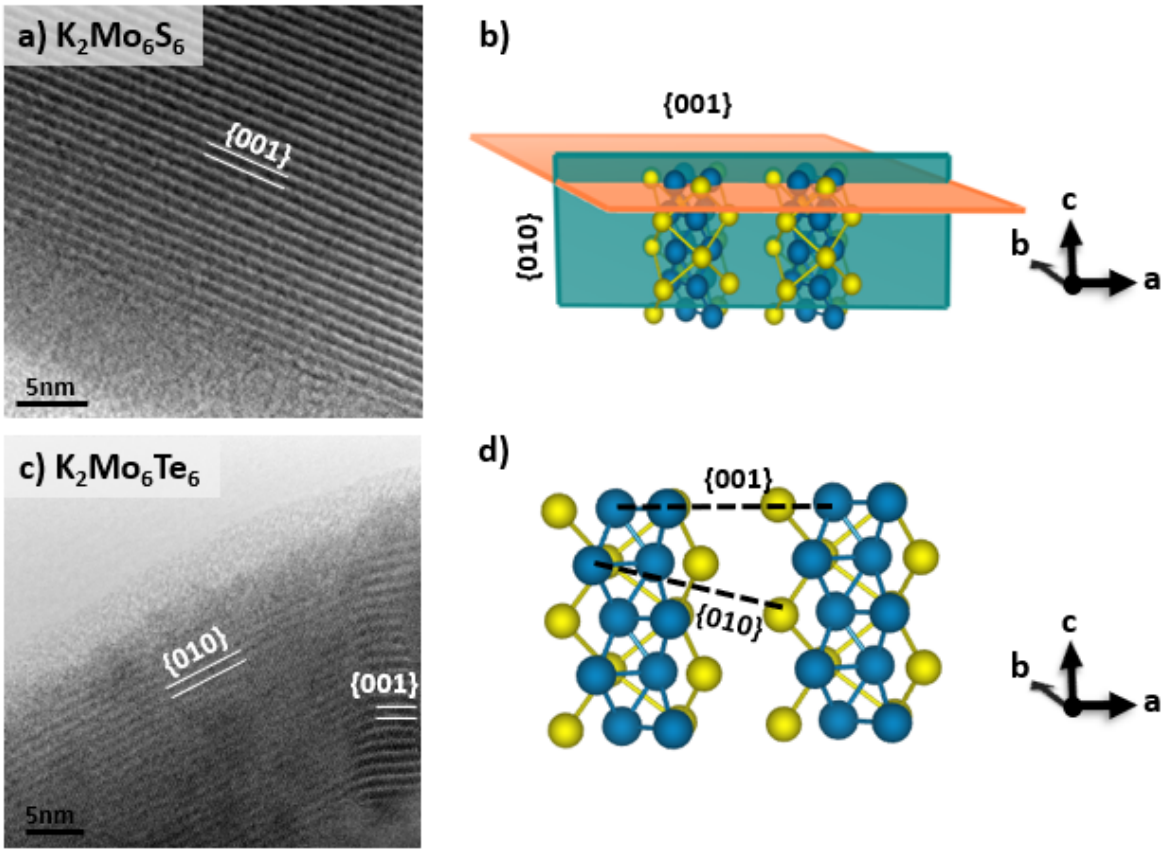

Figure S3.7. Bright-field STEM images for S-PCP (a) and Te-PCP (b) depicting the kinematically forbidden {001} plane (c,d). This plane intercepts with the kinematically allowed {010} plane (c) , therefore both {001} and {010} facets can be observed through the hexagonal c-axis of Te-PCP (b,d).[1,2]

a)

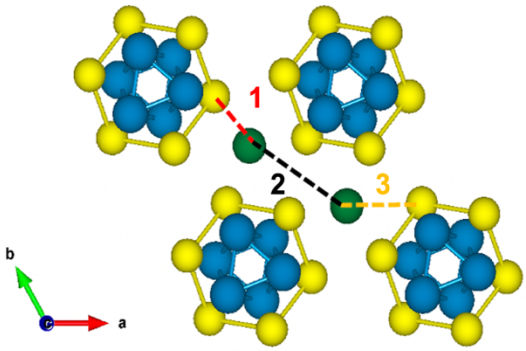

b)

	$K_2Mo_6S_6$	$K_2Mo_6Se_6$	$K_2Mo_6Te_6$
1 (X-K)	2.60Å	2.54Å	2.70Å
2 (K-K)	5.50Å	5.67Å	6.00Å
3 (X-K)	4.01Å	4.14Å	4.36Å

Figure S3.8. PCP unit cell depicting the different chalcogen-potassium (1,3) and potassium-potassium (2) bonds (a) along the corresponding bond distances reported in literature (b). [3,4]

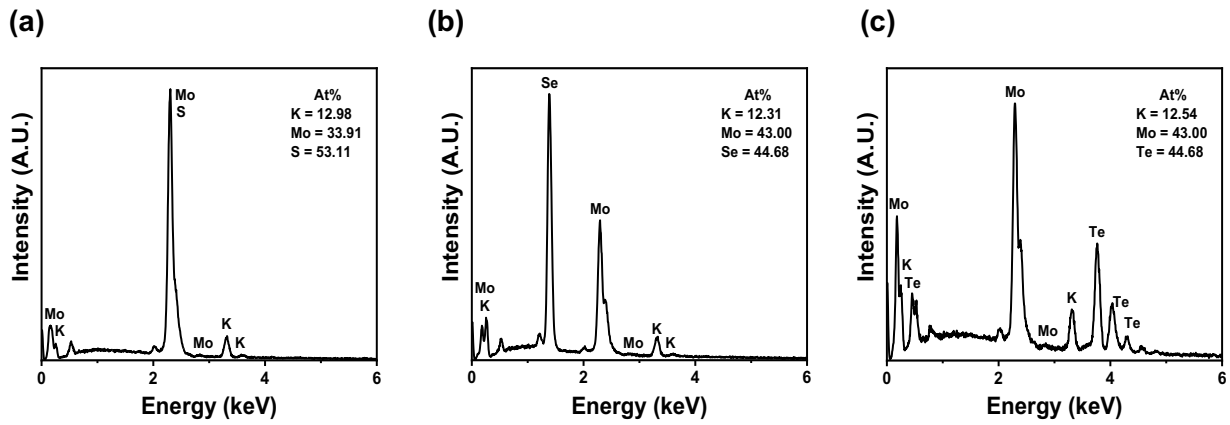

Figure S3.9. EDX spectra for S-PCP (a), Se-PCP (b) and Te-PCP (c). Mo L- and S K-edges overlap, convoluting quantitative determination of Mo and S for S-PCP, while atomic % obtained for Se-PCP and Te-PCP agree with the expected 1:1 molybdenum to chalcogen ratio.

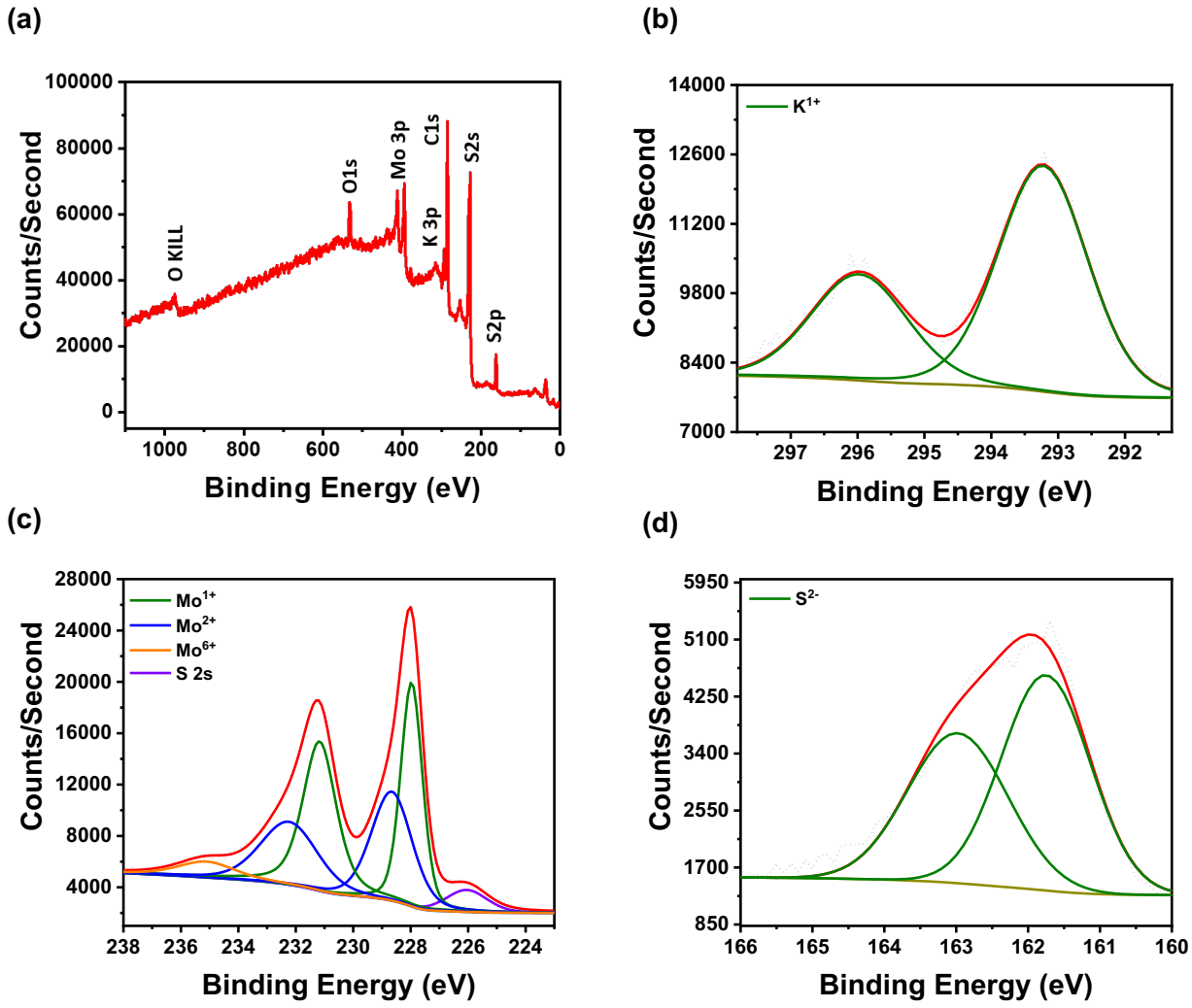

Figure S3.10. XPS survey scan of S-PCP (a) along high-resolution XPS spectra for K 2p (b) Mo 3d (c) and S 2p (d). Molybdenum +1 and +2 peaks are assigned assuming a mixture of Mo oxidation states among the structure leading to an average charge of +1.66 per Mo.[5] Higher binding energy signals for Te and Mo correspond to a surface oxide layer (MoO_3). Oxidation values were determined using the Perkin-Elmer handbook of XPS. [6]

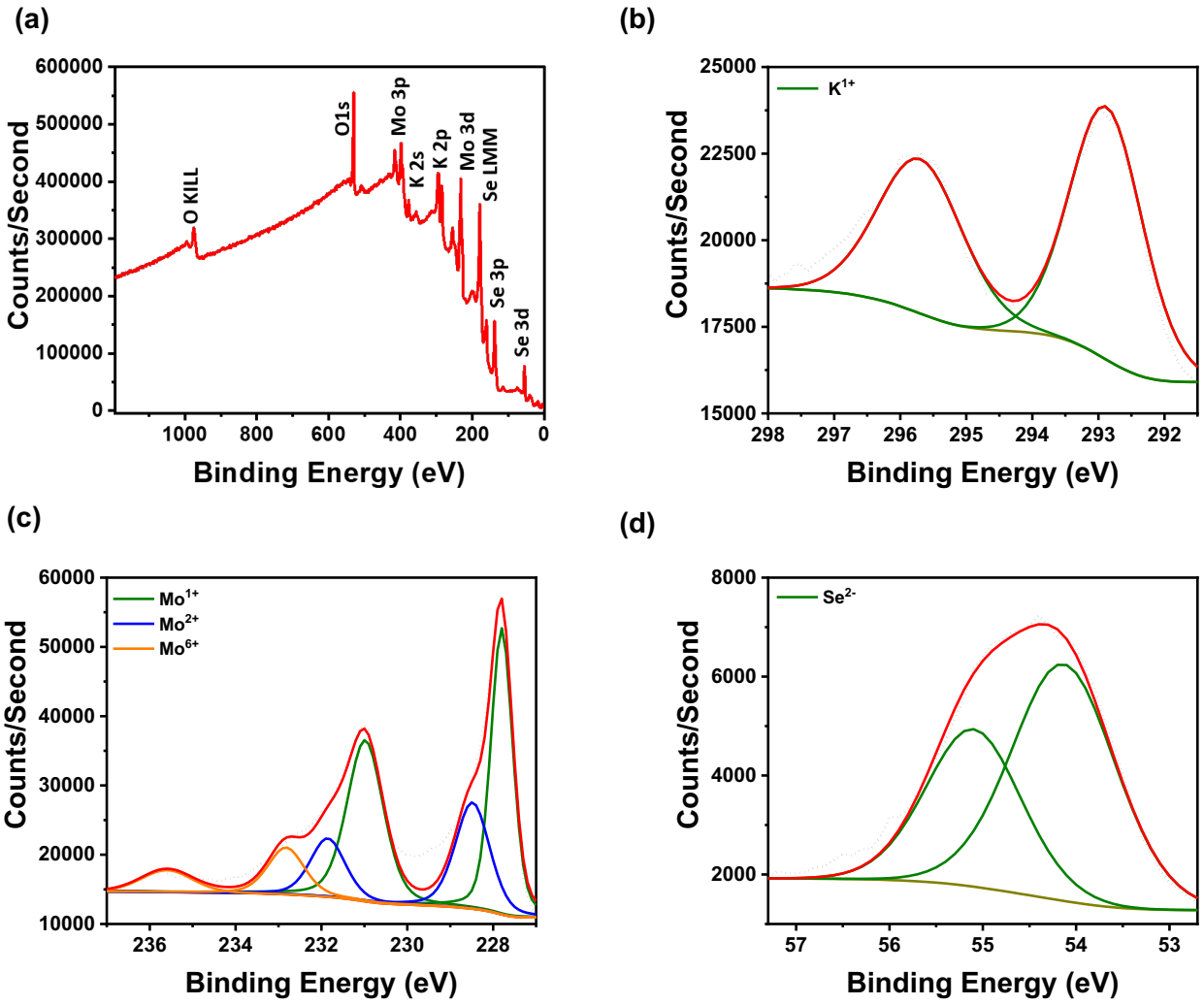

Figure S3.11. XPS survey scan of Se-PCP (a) along high-resolution XPS spectra for K 2p (b) Mo 3d (c) and Se 3d (d). Molybdenum +1 and +2 peaks are assigned assuming a mixture of Mo oxidation states among the structure leading to an average charge of +1.66 per Mo. [5] Higher binding energy signals for Se and Mo correspond to a surface oxide layer (MoO_3). Oxidation values were determined using the Perkin-Elmer handbook of XPS. [6]

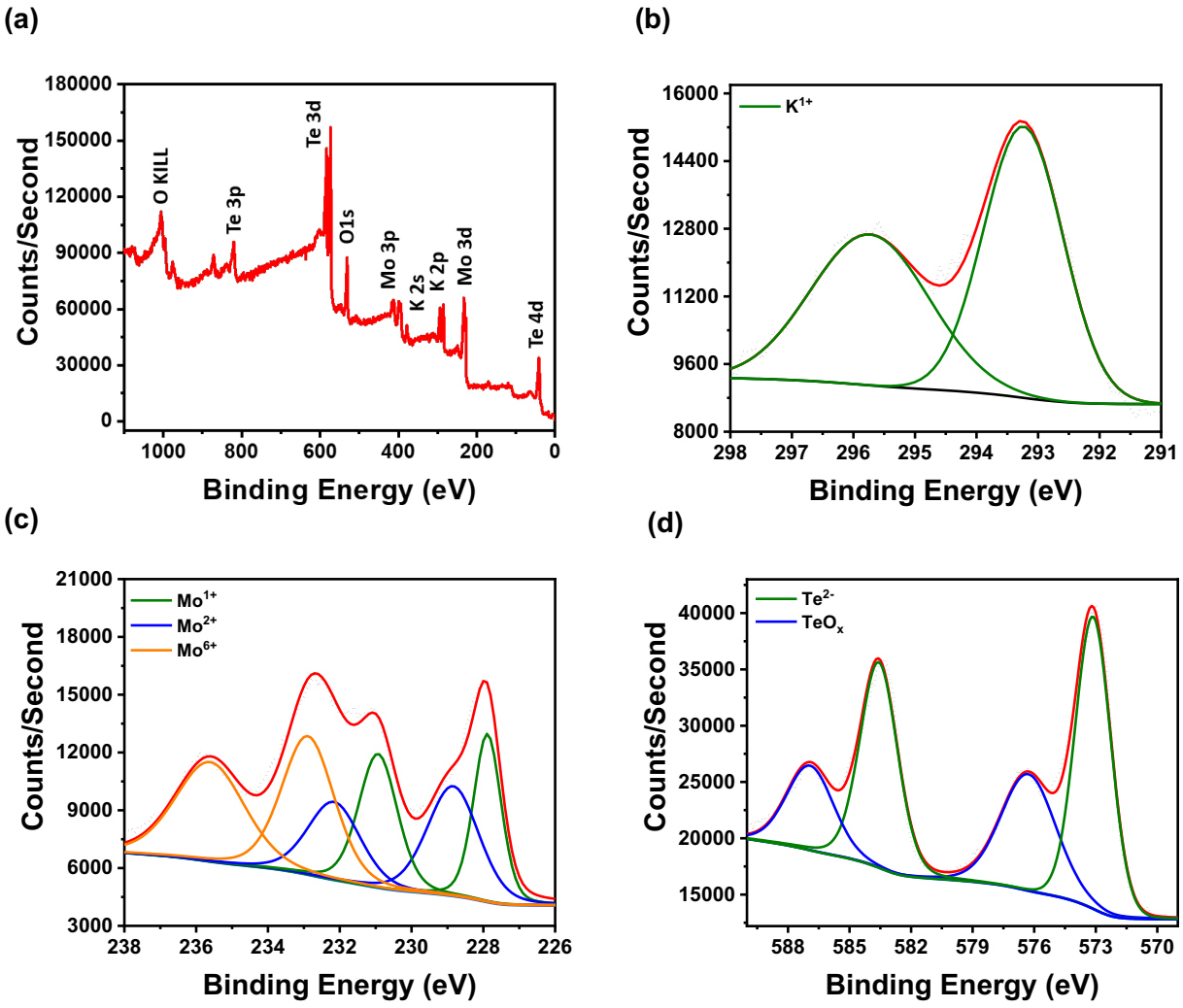

Figure S3.12. XPS survey scan of Te-PCP (a) along high-resolution XPS spectra for K 2p (b) Mo 3d (c) and Te 3d (d). Molybdenum +1 and +2 peaks are assigned assuming a mixture of Mo oxidation states among the structure leading to an average charge of +1.66 per Mo. [5] Higher binding energy signals for Te and Mo correspond to a surface oxide layer (MoO_3). Oxidation values were determined using the Perkin-Elmer handbook of XPS. [6]

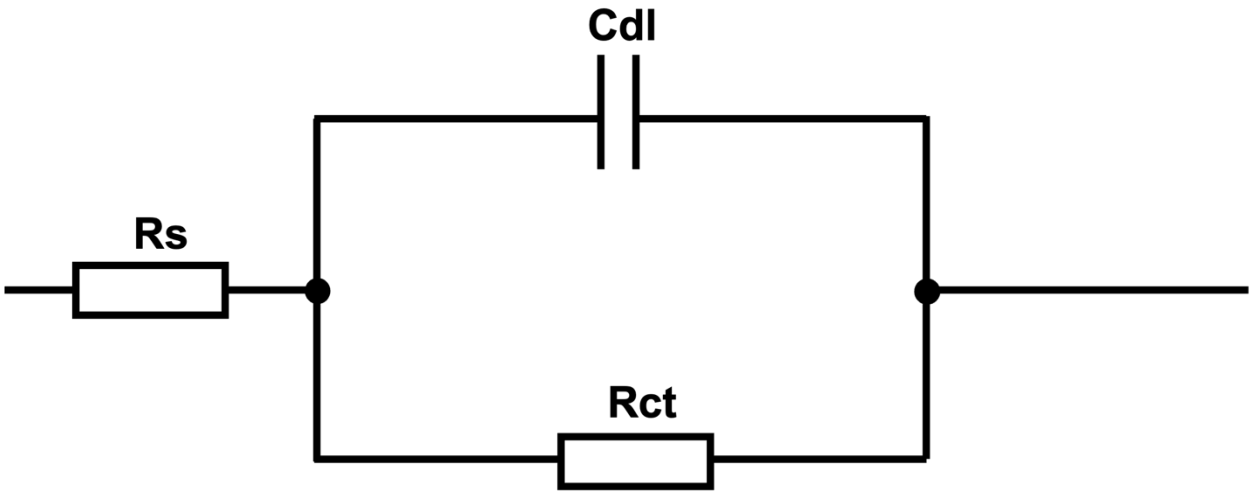

Figure S3.13. Simplified Randles circuit formed by a double-layer capacitive element (Cdl) charge transfer resistance element (Rct) and a circuit resistance element (Rs) that was used to interpret the Nyquist plots of all three PCP chalcogenides.

Material	Unit Cell Parameter	Experimental Value	Literature Value	% Difference
$K_2Mo_6S_6$ (P 63/m)	*a*	8.7473 Å	8.76 Å	0.14
	b	8.7473 Å	8.76 Å	0.14
	c	4.4123 Å	4.42 Å	0.17
	α	90º	90º	0.00
	β	90º	90º	0.00
	γ	120º	120º	0.00
	Volume	292.37Å^3	293.74Å^3	0.47
$K_2Mo_6Se_6$ (P 63/m)	*a*	9.008 Å	9.022 Å	0.16
	b	9.008 Å	9.022 Å	0.16
	c	4.482 Å	4.481 Å	0.02
	α	90º	90º	0.00
	β	90º	90º	0.00
	γ	120º	120º	0.00
	Volume	314.97Å^3	315.87 Å^3	0.28
$K_2Mo_6Te_6$ (P 63/m)	*a*	9.575 Å	9.597Å	0.23
	b	9.575 Å	9.597Å	0.23
	c	4.592 Å	4.600Å	0.17
	α	90º	90º	0.00
	β	90º	90º	0.00
	γ	120º	120º	0.00
	Volume	364.61 Å^3	366.91Å^3	0.63

Table S3.1. Lattice parameters extracted from Pawley refinement for all three PCP chalcogenides structures studied in this work.

Element	Wyckoff positions	A_g	$^2E_{2g}$	$^1E_{1g}$	$^1E_{2g}$	$^2E_{1g}$
Mo, X	6h	2	2	1	2	1
K	2c		1		1	

Raman active modes: $4A_g + 5^2E_{2g} + 2^1E_{1g} + 5^1E_{2g} + 2^2E_{1g}$

X= S, Se, Te

Table S3.2. Raman active modes for the space group $P6_3/m$ (No. 176).[7]

Facet	Surface energy (eV/Formula Unit)
<010>	0.37
<110>	0.93
<001>	4.19

Table S3.3. Previously reported results of computational surface energy modeling for $K_2Mo_6S_6$ <010>, <110>, and <001> surfaces.[8]

Reference

(1) Malo, S.; Vander Griend, D. A.; Poeppelmeier, K. R.; Wang, Y.; Dravid, V. P.Crystal Symmetry of La3Cu2VO9 and La4Cu3MoO12 Derived from the YA1O3 Hexagonal Structure by Transmission Electron Microscopy. *Solid State Sci.* 2001, *3* (1–2), 17–23.

(2) Liao, Y. Practical Electron Microscopy and Database www.globalsino.com/EM/.

(3) Potel, M.; Chevrel, R.; Sergent, M.; Armici, J. C.; Decroux, M.; Fischer. New Pseudo-One-Dimensional Metals: M2Mo6Se6 (M = Na, In, K, TI), M2Mo6S6 (M = K, Rb, Cs), M2Mo6Te6 (M = In, TI). *J. Solid State Chem.* 1980, *35* (2), 286–290.

(4) Tarascon, J. M.; Hull, G. W.; DiSalvo, F. J. A Facile Synthesis of Pseudo One-Monodimensional Ternary Molybdenum Chalcogenides M2Mo6X6 (X = Se,Te; M = Li,Na..Cs). *Mater. Res. Bull.* 1984, 19 (7), 915–924.

(5) Chevrel, R.; Gougeon, P.; Potel, M.; Sergent, M. Ternary Molybdenum Chalcogenides: A Route to New Extended Clusters. *J. Solid State Chem.* 1985, *57* (1), 25–33.

(6) Briggs, D. X-Ray Photoelectron Spectroscopy (XPS). *Handb. Adhes. Second Ed.* 2005, 621–622.

(7) Kroumove et. al. *Phase Transitions* (2003), 76, Nos. 1-2, 155-170.

(8) Perryman, J. T.; Kulkarni, A. R.; Velázquez, J. M. Direct Solid-State Nucleation and Charge-Transport Dynamics of Alkali Metal-Intercalated M2Mo6S6(M = K, Rb, Cs) Nanorods. *J. Mater. Chem. C* 2020, *8* (31), 10742–10748.

Chapter 4: Structure-reactivity relationships in Chevrel Phase electrocatalysts for small-molecule reduction reactions

Abstract

Chevrel Phases, $M_xMo_6X_8$ (M= metal intercalant, X= chalcogen), constitute a family of materials with composition-dependent physicochemical properties that have shown promising electrocatalytic activity for various small-molecule reduction reactions. The wide range of possible compositions among the Chevrel Phase family offers the opportunity to tune the local and electronic structure of discrete Mo_6X_8 cluster units within the extended $M_xMo_6X_8$ framework. Thus, making them an ideal platform for studying structure-function relationships and generating design principles for improved electrocatalytic reactivity. This review summarizes the state of the art in experimental and computational evaluations of Chevrel Phases as electrocatalysts for hydrogen evolution, CO_2 reduction, and nitrogen reduction reactions. We aim to elucidate the uncharted small-molecule electrochemical reactivity of Chevrel Phases as a function of composition and consequently guide the design of promising multinary chalcogenides for energy conversion reactions.

Keywords: Chevrel Phases (CPs), Multinary chalcogenides, Electrocatalysis, Hydrogen Evolution Reaction (HER), CO_2 Reduction Reaction (CO_2RR), Nitrogen Reduction Reaction (NRR).

1. CPs as HER catalyst

Since their discovery, CPs have been extensively evaluated as HER catalysts [1–9]. As shown in Table 1, HER relies on the ability of the catalytic surface to adsorb H, making the adsorption/desorption behaviors of the solid surface a crucial property in HER catalysis. [10,11]

Table 4.1. HER mechanism in acidic electrolyte

Acidic electrolyte $2H_{(aq)}^{+} + 2e^{-} \rightarrow H_{2(g)}$	
Volmer step	$H^{+} + e^{-} \rightarrow H_{ads}$
Tafel step	$2H_{ads} \rightarrow H_2$
Heyrovsky step	$H^{+} + H_{ads} + e^{-} \rightarrow H_2$

Theoretical studies under various reaction conditions agree that H adsorption (H_{ads}) interactions in CPs occur through the chalcogen-molybdenum bridging site [6,12–14]. A recent investigation by Ortiz-Rodríguez et al. [6] has supported such results by elucidating changes in the HER activity of CPs as a function of chalcogen (Mo_6X_8, X = S, Se, Te) in acidic media. Fig. 4.1a shows the polarization curves for polycrystalline CP powders deposited on a carbon substrate. The decrease in overpotential to achieve a current density of 10 mA cm⁻

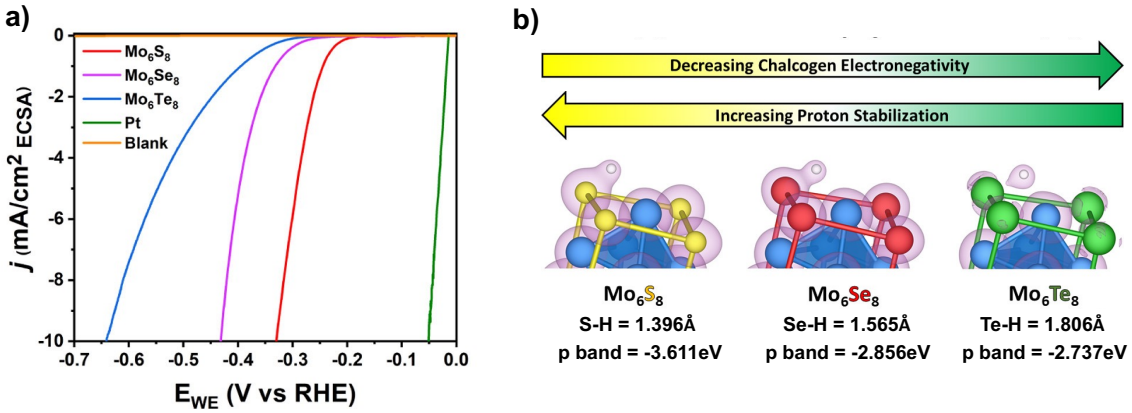

Figure 4.1. (a) HER polarization curves for CP chalcogenide electrodes in 0.5 M H_2SO_4, along with 20% Pt/C on Vulcan Carbon Cloth and a blank (carbon paper with PTFE/carbon black/IPA ink) for comparison. (b) Graphical representation of the changes in H_{ads} interactions as a function of chalcogen along the calculated X-H bond distances and corresponding p band center. Copyright 2020 American Chemical Society. Figure reproduced with permission from ref 6.

$^{2}_{ECSA}$ indicates an increase in the HER activity as the Lewis basicity of the X_8 chalcogen cage increases. The reactivity trend was explained by the decrease in X-H distance as well as the improved H_{ads} energy calculated for the CP sulfide compared to the selenide and telluride phases. Such changes are illustrated in Fig. 4.1b where H_{ads} occurs farther from the chalcogen as the electronegativity of the chalcogen decreases (H-S<H-Se<H-Te). Furthermore, Mo_6S_8 maintained a steady time-dependent overpotential at a current density of 10 mA cm^{-2} over 48 hrs.

It was concluded that the changes in H stabilization are influenced by changes in the local bonding environment (local effect) and the bulk electronic structure as a function of chalcogen (electronic effect), which can be described using the simplified orbital representation in Fig.4.2. Hughbanks and Hoffmann [15] elucidated that the frontier orbitals of CPs are formed by twelve bonding and eighteen antibonding orbitals, primarily Mo d in character. The relative positions and the width of the d bands are strongly influenced by the covalent mixing with the X p states, which decreases in the sequence Mo_6S_8< Mo_6Se_8< Mo_6Te_8 [16]. The lower 3p sulfur orbitals of Mo_6S_8 shown in Fig. 4.2 have a higher p character which improves the H-S orbital

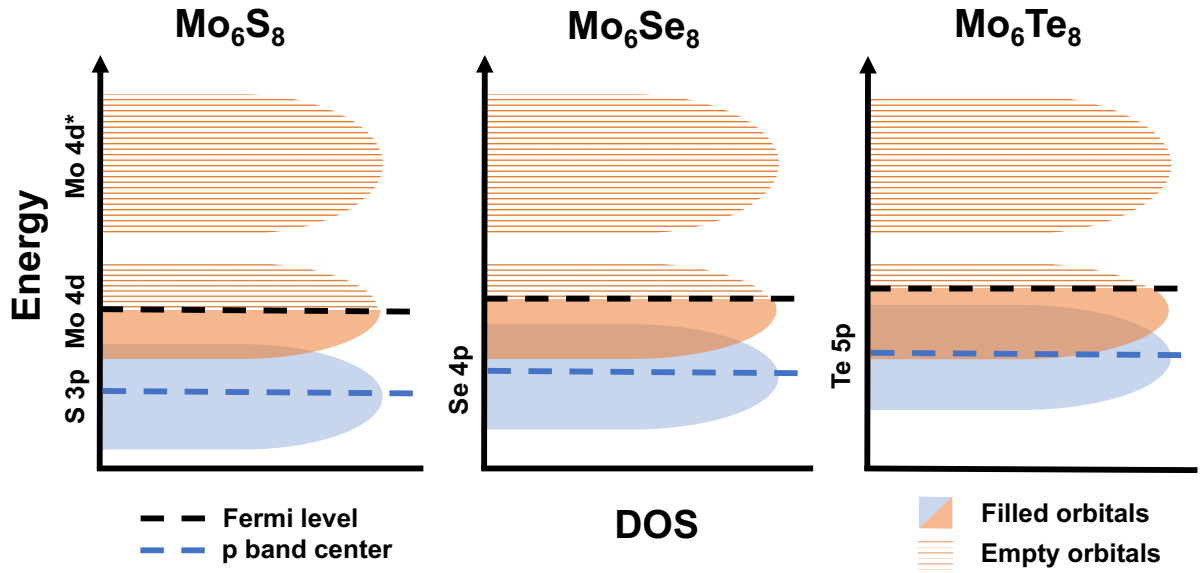

Figure 4.2. Simplified representation of the frontier orbital interactions of CP chalcogenides based on ref [2,16,66,67] The slight increase in the density of states at the Fermi level as the electronegativity of the chalcogen decreases is caused by a decrease in the formal charge of the chalcogen. [66–72]

overlap and allows the favorable stabilization of H at the chalcogen site (local effect). Likewise, the increase in energy of the chalcogen p orbitals leads to a higher p band center (Fig.4.2, dashed blue line) which scales inversely with the observed HER overpotentials (electronic effect). Therefore, the observed reactivity trend suggests that in binary CPs the position of the p-band center is a useful descriptor to predict their HER activity, which has also been the case for other recent HER catalyst [17–20].

Metal-intercalated and Mo_6 octahedron substituted CPs have also been evaluated as HER catalyst [1,2,4,8,9]. By evaluating various metal-intercalated and octahedron substituted CPs, Shubert and Tributsch [4] identified that the single most active metal center favors HER. That is, either the Mo of the Mo_6-octahedron or the intercalated/substituted metal determines the catalytic activity. Fig. 4.3 shows the results that lead to this conclusion. The authors evaluated the exchange current (i_0) and overpotential (η) of various polycrystalline CPs with the same figures of merit for monometallic electrodes of the corresponding intercalated/substituted metal in acidic media (e.g., $CdMo_6S_8$/Cd; $Mo_2Re_4S_8$/Re). To identify the active center for HER, correlations between the i_0 and η of CPs and the monometallic electrodes were made. It

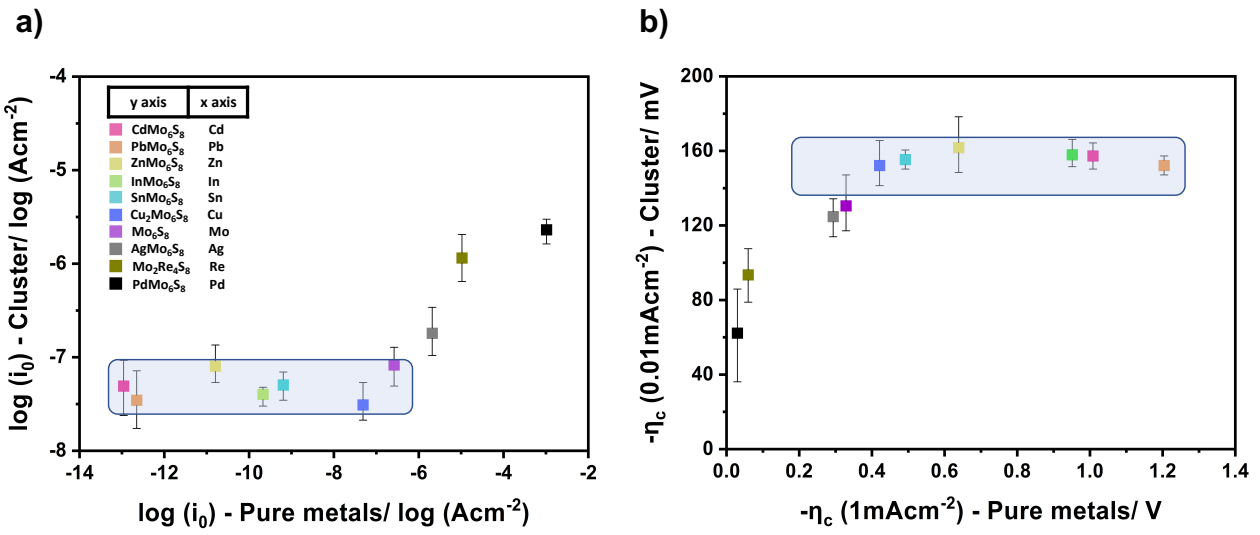

Figure 4.3. (a) Correlation between log (i_0) of CPs and log (i_0) of monometallic electrodes of the corresponding intercalated/substituted metal. (b) Correlation between η of CPs and the η of monometallic electrodes of the corresponding intercalated/substituted metal. CP electrodes contained polycrystalline CP powders, graphite powder (improve conductivity) and nujol (pasting medium). Shaded area includes materials in which the Mo-octahedron is strongly dominating the reduction mechanism. Data obtained from ref 4.

was noticed that although the i_0 and η varied continuously for each monometallic electrode (x axis), multiple CPs share the same i_0 and η value (y axis). The shaded areas indicate CPs with statistically identical i_0 and η values while the values for their corresponding metal intercalant (Cd, In, Pb, Sn, Zn, Cu, Mo) change. Thus, it is believed that the Mo octahedron is mainly responsible for proton reduction in this case as if the metal intercalant was the active center, the i_0 and η values for the CPs will vary. In contrast, deviations from the shaded area suggest that the intercalated or substituted metal strongly influences the catalytic activity as the i_0 and η for the CP and the monometallic electrode change continuously.

Based on these results, HER activity is directed by the Mo octahedron for MMo_6S_8 (M= Cd, In, Pb, Sn, Zn, Cu_2), which all have a lower HER activity than Mo_6S_8. The trend observed is further exemplified by the descriptors elucidated by Ortiz-Rodriguez et al. [6] since higher p-band centers are expected upon metal intercalation due to the electron donation from the metal intercalant to the chalcogen. [21–24] Interestingly, the intercalated or substituted metal dominates HER activity in MMo_6S_8 (M=Ag, Pd) and $Mo_2Re_4S_8$. The improved HER activity of these CPs compared to Mo_6S_8 suggest the direct participation of the intercalated/substituted metal as an active site for H_{ads}. However, further evaluations that elucidate changes in proton adsorption as the chemical environments that influence HER activity change (intercalated/substituted metal or Mo octahedron) remain to be performed.

Recent efforts to improve the HER activity of CPs have been focused on the design of nanoscale CPs [3,5,7]. A comparison between bulk and nanoparticulate Mo_6S_8 in acidic media shows an increase in the HER activity as the surface area-to-volume increases as well as structural stability after 1,000 voltammetry cycles [3]. Nanoscale Mo_6S_8 also shows an improved HER activity to nanoscale MMo_6S_8 (M= Cu, Zn), which agrees with the results obtained by Shubert and Tributsch [4]. Improvements in the catalytic activity of CP nanoparticles have also been observed by the inclusion of carbon additives in the catalyst electrode [7,8]. Although these approaches have shown to successfully enhance the HER activity of CPs, significant improvements could be made by atomically identifying the most active surface sites(s) in CP nanoparticles and generating synthetic

approaches that could preferentially yield such active site ensembles. Likewise, fewer reports have evaluated the HER activity of CPs in alkaline media, which have shown promising electrocatalytic activity and stability under these conditions [5,9]. Therefore, the reactivity trends discussed remain to be further evaluated in alkaline reaction conditions.

2. CPs as CO_2RR and NRR catalyst

Favorable intermediates energies are predicted for the reduction of CO_2 to methanol in Mo_6S_8 and metal-intercalated CPs [12,25] following the chemical equation:

$$CO_2 + 6H^+ + 6e^- \rightarrow CH_3OH + H_2O$$

As shown in Fig.4.4, CO_2RR intermediates are predicted to interact at the Mo sites in Mo_6S_8 preferentially, whereas S atoms facilitate H-H bond cleavage by forming relatively strong S-H bonds [12]. The addition of metal intercalants and substitutions in the Mo octahedron are expected to change the interactions of CO_2RR intermediates compared to Mo_6S_8; however, H_{ads} still preferentially occurs through chalcogen interactions [13,25–28]. Fig. 4.5 shows the expected influence of metal intercalants in the CO_2RR mechanism of CPs, which includes interactions through modifications in the electronic structure (ligand effect) or participation of the metal intercalant as an active site (ensemble effect) [25].

Perryman et al. [24] experimentally validated the CO_2RR activity of CPs elucidated by theory. This study evaluated the ability of polycrystalline Mo_6S_8, $Cu_2Mo_6S_8$, $Ni_2Mo_6S_8$, and $Cr_{1.73}Mo_6S_8$ to reduce CO_2 and CO in 0.1 M Na_2CO_3 and 0.1 M $NaHCO_3$, respectively. Electrochemical results followed by gaseous and liquid product analysis show that all CPs reduced CO_2 to only methanol and formate in the liquid phase, while H_2 production had the highest faradaic efficiency. The electrocatalytic performance of $Cu_2Mo_6S_8$ was maintained over the course of multiple hours of electrolysis, even at a reductive potential of -1V vs. RHE.

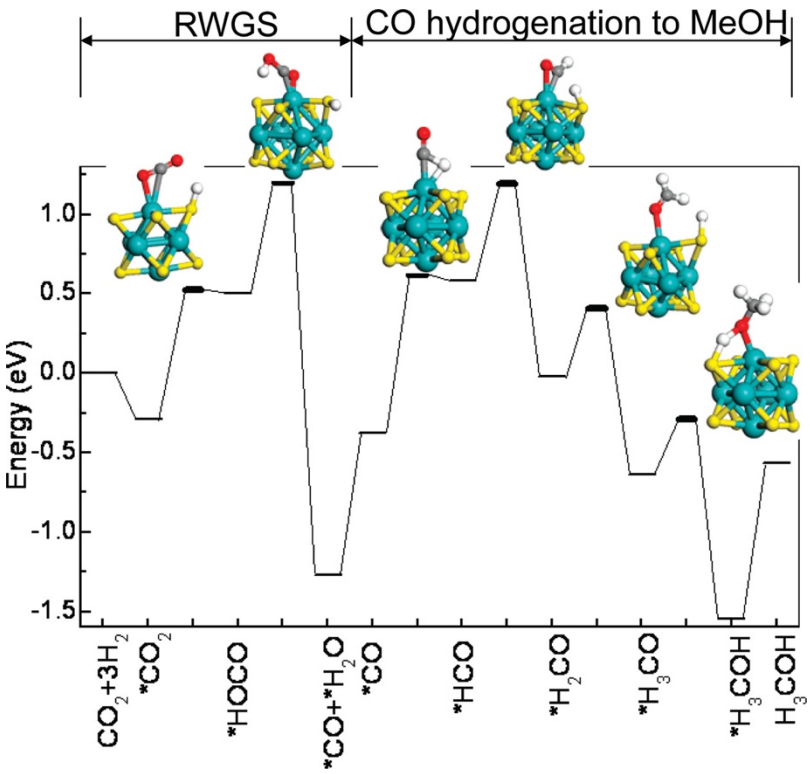

Figure 4.4. Optimized potential energy diagram for methanol synthesis from CO_2 and H_2 on a Mo_6S_8 cluster. Thin bars represent the reactants, products, and intermediates; the thick bars stand for the transition states (Mo, cyan; S, yellow; C, gray; O, red; H, white). Copyright 2009 American Chemical Society. Figure reproduced with permission from ref 12.

Furthermore, the selectivity of $Cu_2Mo_6S_8$ towards methanol production was increased when CO was introduced as the target for reduction, which circumvents formate production. These results suggest that the pathway for methanol production on $Cu_2Mo_6S_8$ catalysts does proceed via CO hydrogenation following the predicted mechanism for CO_2RR in Mo_6S_8 [12] (Fig. 4.4). Therefore, the dominance of the ligand effect

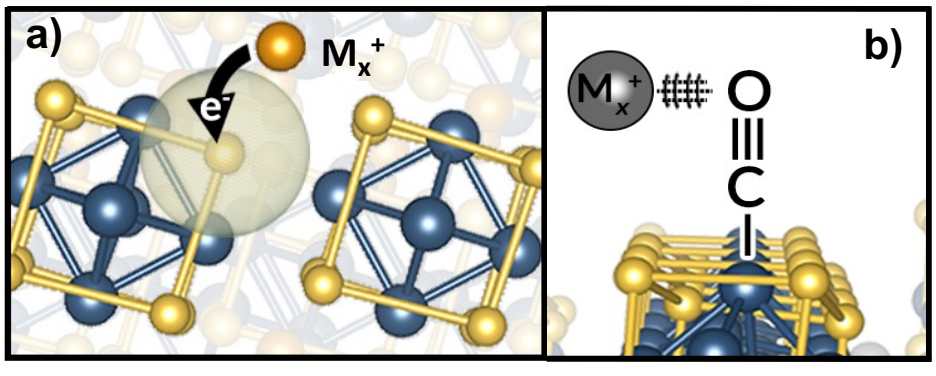

Figure 4.5. Electrocatalytic (a) ligand and (b) ensemble effect of metal intercalants in the CP structure.

over the ensemble effect is expected for $Cu_2Mo_6S_8$, but further operando experiments are needed to confirm this hypothesis.

Fig. 4.6 shows the changes in the electronic structure upon Cu intercalation into the Mo_6S_8 cluster obtained through X-ray Absorption Near-Edge Structure (XANES). The minimal shift in the Mo K-edge absorption observed for Mo_6S_8 and $Cu_2Mo_6S_8$ in Fig.4.6a indicates an insignificant change in the electronic structure of the Mo, which is predicted to be crucial in the stabilization of CO_2RR intermediates [12,13,25–28]. The intercalation of Cu seems to preferably influence the electronic structure of the chalcogen cage as it fills available S 3p orbitals causing a decrease in the S K pre-edge shoulder (~2471 eV) of $Cu_2Mo_6S_8$ compared to Mo_6S_8 (Fig. 4.6b). Following the previous discussion regarding H_{ads} interactions, the electronic changes induced by Cu intercalation could influence H_{ads} at the S-Mo bringing site rather than CO_2RR intermediates at the Mo site, which could be a topic of interest for future studies.

An alternative to increase methanol production in CPs could be to increase the d-band electron density, which has been shown to increase the activity of CPs for ORR. Vante et al. [1] evaluated different Mo-

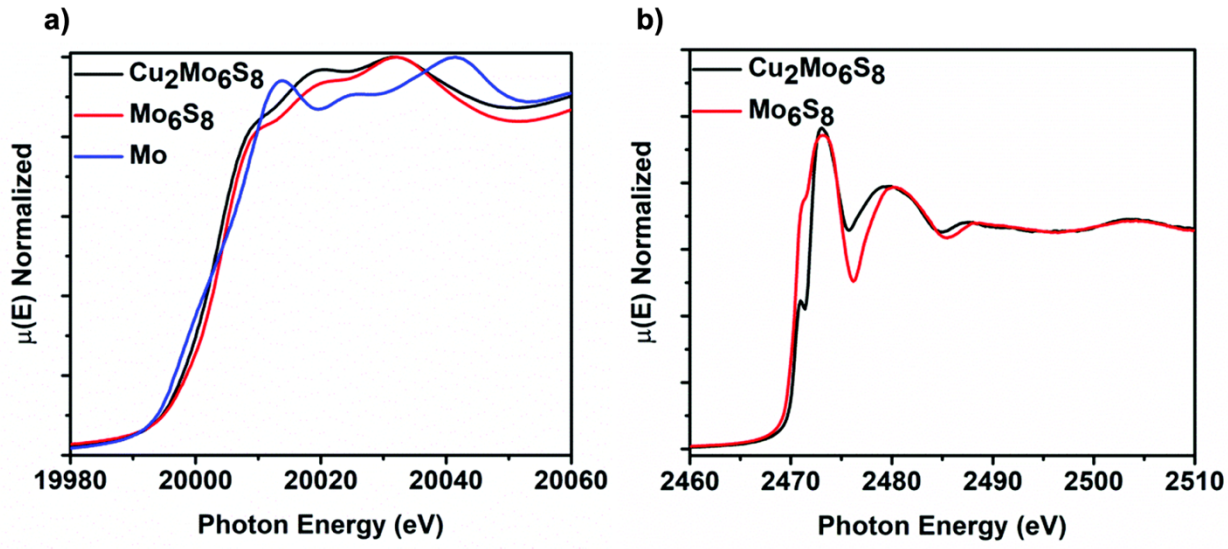

Figure 4.6. (a) K-edge XANES for Mo in $Cu_2Mo_6S_8$ and Mo_6S_8, with Mo^0 foil for reference. (b) K-edge XANES for S in $Cu_2Mo_6S_8$ and Mo_6S_8. Copyright 2020 Royal Society of Chemistry. Figure reproduced with permission from ref 24.

containing compounds in which the concentration of d electrons changes by rising the Fermi level when going from the Mo cluster (Mo_6Se_8) to the substituted ones ($Mo_4Ru_2Se_8$/ $Mo_2Re_4Se_8$). As shown in Fig.8, partial substitution of the Mo octahedron by Re or Ru raises the valency electron concentration in the cluster from $20e^-$ to 24 e^-, which increases the occupation of metal d states near the Fermi level while the chalcogen electronic structure is minimally altered [29–31] (Fig.4.7). Such electronic changes have been shown to significantly improve the ORR activity of CPs [32–35]. The poor ORR catalytic properties of Mo_6Se_8 compared to $Mo_4Ru_2Se_8$/ $Mo_2Re_4Se_8$ can be related to the small metal d-density at the Fermi edge, which decreases the stabilization of oxygen intermediates [33,34,36]. Similar to what is predicted for CO_2, molecular oxygen interacts preferentially with the metallic centers at the octahedron, therefore the evaluation of CPs with increased metal d-density at the Fermi edge could lead to improved CO_2RR catalytic activity.

Lastly, computational calculations can also assist in designing CPs with improved CO_2RR efficiencies. KMo_6S_8 has been predicted to facilitate CO_2 to methanol conversion due to a strong ensemble effect of K, which could stabilize CO_2 intermediates through electrostatic interactions and lower the corresponding transition states involving H_xCO_y radicals [25]. Single-atom catalysis on CPs [14,26,27] and other metal intercalated CPs [13,28,37]

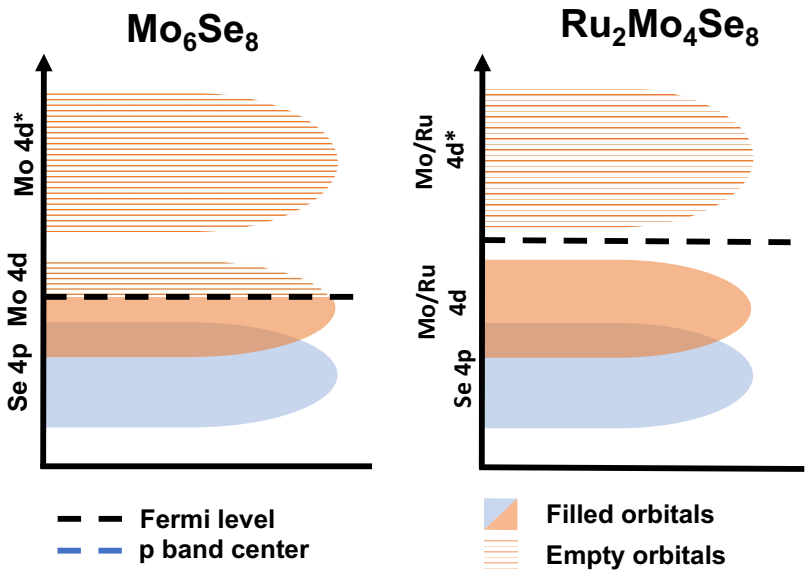

Figure 4.7. Simplified representation of the changes in frontier orbital interactions for Mo_6Se_8 and $Ru_2Mo_4Se_8$ based on ref 31, 34, 35.

have also been computationally evaluated as CO_2 and CO conversion catalysts, showing promising C_1 and C_2 products. However, there is currently no experimental evidence to confirm such predictions. It is important to mention that most of the computational studies discussed do not consider structural effects such as the synthetic accessibility of CPs, [38,39] changes in cavity occupancy as a function of metal intercalant stoichiometry and/or identity, [38,40–42] metal intercalant mobility, [43–45] and metal de-intercalation upon applied potential [2]. Therefore, there is a broad opportunity to experimentally validate computational predictions and study other structural effects not considered by theory.

Although NRR has been less studied in CPs, experimental results strongly suggest that the ensemble effect dominates the reaction. Lu et al. [46] evaluated polycrystalline Mo_6S_8, $Cu_2Mo_6S_8$, $Mn_2Mo_6S_8$, and $Fe_2Mo_6S_8$ as electrocatalysts for the conversion of N_2 to NH_3 in aqueous solution (pH ~4.6), following the equation:

$$N_2 + 6H^+ + 6e^- \rightarrow 6NH_3$$

An increase in faradaic efficiency and NH_3 production rate was observed in metal-intercalated CPs, being $Fe_2Mo_6S_8$ the best performing catalyst (Fig. 4.8a). The intercalation of Fe into the CP cluster also increased the overpotential for the competing HER (Fig. 4.8b) leading to the increased NRR selectivity. In addition,

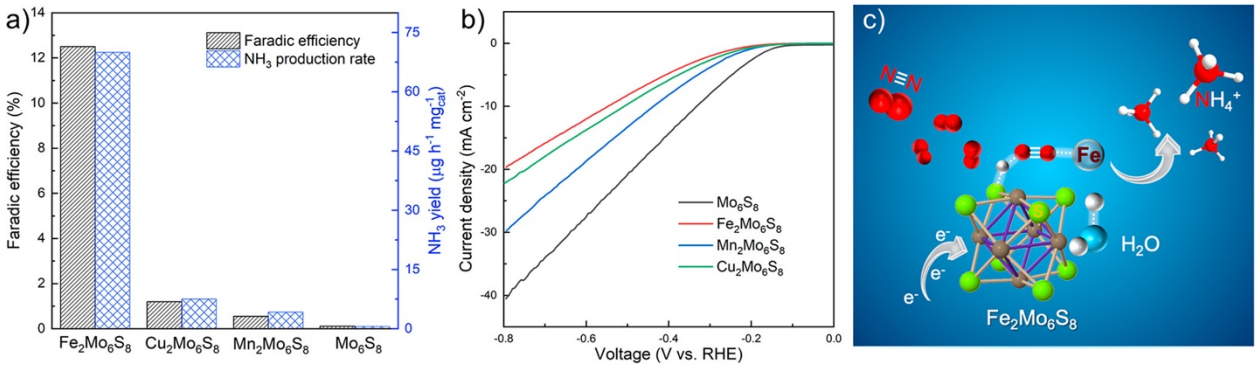

Figure 4.8. (a) Comparison of N_2 to NH_3 conversion efficiency and average NH_3 production rate for Mo_6S_8 and $M_2Mo_6S_8$ (M = Fe, Mn, and Cu) electrocatalysts in aqueous electrolyte (0.5 M Na_2SO_4/0.1 M sodium citrate buffer). (b) Linear sweep voltammetry (LSV) curves for hydrogen evolution in Ar-saturated electrolyte. (c) Schematic illustration of the proposed binding mechanism for N_2 absorption and subsequent conversion to NH_3. Copyright 2021 American Chemical Society. Figure reproduced with permission from ref 46.

chronoamperometric responses for $Fe_2Mo_6S_8$ at potentials ranging from -0.15V to -0.40V vs RHE show stable currents for the 2hr testing period. It was concluded that Fe must participate in the absorption and/or conversion of N_2, while Mo and S atoms alone are unable to activate N_2. The proposed mechanism for N_2 conversion on $Fe_2Mo_6S_8$ is shown in Fig. 4.8c in which Fe directly interacts with N_2 while the chalcogen sites are expected to assist in H_{ads}. Further improvements in catalytic activity will highly benefit from computational work that unravels the NRR mechanism on Fe2Mo6S8 and could identify ways to enhance intermediate stabilization.

Conclusion and outlook

This review emphasized the adsorption of key intermediates in CPs under HER, CO_2RR, and NRR conditions as well as their composition-dependent electrochemical properties. The discussion highlights the compositional control over orbital population, orbital symmetry, and intermediate adsorption strength in CPs which provide a platform to generate transferable principles for improved catalyst design. Among those, we highlight the influence of the local and electronic structure in the HER activity of CPs as well as the predicted ligand and ensemble effects that dominate reaction trajectories in CO_2RR, and NRR. Several routes to improve the electrocatalytic activity of CPs are proposed, considering computational and experimental efforts that elucidate electrochemical small-molecule reactivity.

As the electrochemical evaluation of CPs for energy conversion reactions moves forward, it is imperative to unravel the structural changes at the catalyst interface under an electrochemical environment in order to generate reactivity descriptors that extend from the bulk electronic properties discussed. To this end, we suggest the incorporation of in situ/operando experimentation such as in situ atomic scale scanning transmission electron microscopy (STEM) [47,48], electrochemical scanning tunneling microscopy (ECSTM) [49,50] and in situ/operando synchrotron-based X-ray techniques to understand changes at the electrode-electrolyte interface [51,52]. Likewise, the incorporation of electroanalytical techniques such as scanning

electrochemical microscopy (SECM) [53,54], differential electrochemical mass spectrometry (DEMS) [55–57] and in-situ electrochemical Fourier transform infrared spectroscopy (FTIR) [58–60] will enable direct probing of the local activity and improve the current mechanistic understanding of CO_2RR and NRR on the CP interface by allowing the detection of key intermediate species beyond those included herein.

Besides the inherent challenges of applying the suggested techniques to fully understand the electrocatalytic activity of CPs, [61–63] it is essential to develop alternative synthetic approaches that would generate well-defined CP nanoparticles and thin films which allow the proper characterization of the outermost atomic layer of CPs at which intermediate adsorption and charge transfer interactions take place. The latter is specifically important when considering spectroscopy techniques in which the penetration depth of the emission source will lead to contributions from the bulk and surface electronic structure [52,64,65]. Lastly, a systematic evaluation of catalytic activity as a function of reaction conditions (e.g., pH, electrolyte ions, crystallinity of the electrode), as well as long-term stability measurements, must be evaluated for future comparisons with state-of-the-art electrocatalysts. We expect that the comprehensive conceptualization in this review reveals the underexplored potential of CPs as a highly tunable platform to study composition-dependent reactivity trends and generate design principles for improved catalyst design.

Acknowledgments

We gratefully acknowledge Brian Wuille Bille for assisting in the design of the table of contents image.

Publication Information, Copyright, and Author Acknowledgements

This chapter forms the basis for the following publication:

Ortiz-Rodríguez, J.C.; Velázquez, J.M.*, Structure-reactivity relationships in Chevrel Phase electrocatalysts for small-molecule reduction reactions, Current Opinion in Electrochemistry, 2022, 34, 101002. https://www.sciencedirect.com/science/article/pii/S2451910322000679

Reference

(1) Alonso Vante, N. A.; Schubert, B.; Tributsch, H.; Perrinf, A. Influence of D-State Density and Chemistry of Transition Metal Cluster Selenides on Electrocatalysis. *J. Catal* 1988, *112*, 384–391.

(2) Alonso Vante, N.; Schubert, B.; Tributsch, H. Transition Metal Cluster Materials for Multi-Electron Transfer. *Mater. Chem. Phys.* 1989, *22*, 281–307.

(3) Strachan, J.; Masters, A. F.; Maschmeyer, T. Chevrel Phase Nanoparticles as Electrocatalysts for Hydrogen Evolution. *ACS Appl. Nano Mater.* 2021, *4* (2), 2030–2036.

(4) Schubert B; Tributsch H. Single-Metal Catalytic Centers for Hydrogen Evolution. *J. Electrochem. Soc* 1993, *140*, 98–103.

(5) Naik, K. M.; Sampath, S. Cubic Mo6S8-Efficient Electrocatalyst towards Hydrogen Evolution over Wide PH Range. *Electrochim Acta* 2017, *252*, 408–415.

(6) Ortiz-Rodríguez, J. C.; Singstock, N. R.; Perryman, J. T.; Hyler, F. P.; Sarah, J.; Holder, A. M.; Musgrave, B.; Velázquez, J. M. Stabilizing Hydrogen Adsorption through Theory-Guided Chalcogen Substitution in Chevrel-Phase Mo6X8 (X = S , Se , Te) Electrocatalysts. *ACS Appl Mater Interfaces* 2020, *12* (32), 35995–36003.

(7) Elgendy, A.; Papaderakis, A. A.; Byrne, C.; Sun, Z.; Lauritsen, J. v.; Higgins, E. P. C.; Ejigu, A.; Cernik, R.; Walton, A. S.; Lewis, D. J.; Dryfe, R. A. W. Nanoscale Chevrel-Phase Mo6S8 Prepared by a Molecular Precursor Approach for Highly Efficient Electrocatalysis of the Hydrogen Evolution Reaction in Acidic Media. *ACS Appl. Energy Mater.* 2021.

(8) Ojha, K.; Banerjee, S.; Sharma, M.; Dagar, P. Synthesis of Chevrel Phase (Cu61.8Mo6S8) in Composite with Molybdenum Carbide for Hydrogen Evolution Reactions. *Bull. Mater. Sci.* 2018, *41* (119), 1–7.

(9) Jiang, J.; Gao, M.; Sheng, W.; Yan, Y. Hollow Chevrel-Phase NiMo3S4 for Hydrogen Evolution in Alkaline Electrolytes. *Angew. Chem.* 2016, *128* (49), 15466–15471.

(10) Li, F.; Han, G. F.; Noh, H. J.; Jeon, J. P.; Ahmad, I.; Chen, S.; Yang, C.; Bu, Y.; Fu, Z.; Lu, Y.; Baek, J. B. Balancing Hydrogen Adsorption/Desorption by Orbital Modulation for Efficient Hydrogen Evolution Catalysis. *Nat. Commun.* 2019, *10* (1), 4060.

(11) Wang, J.; Liu, J.; Zhang, B.; Ji, X.; Xu, K.; Chen, C.; Miao, L.; Jiang, J. The Mechanism of Hydrogen Adsorption on Transition Metal Dichalcogenides as Hydrogen Evolution Reaction Catalyst. *Phys. Chem. Chem. Phys.* 2017, *19* (15), 10125–10132.

(12) Liu, P.; Choi, Y.; Yang, Y.; White, M. G. Methanol Synthesis from H2 and CO2 on a Mo6S8 Cluster: A Density Functional Study. *J. Phys. Chem. A* 2010, *114* (11), 3888–3895.

(13) Cao, Z.; Guo, L.; Liu, N.; Zheng, X.; Li, W.; Shi, Y.; Guo, J.; Xi, Y. Theoretical Study on the Reaction Mechanism of Reverse Water-Gas Shift Reaction Using a Rh-Mo6S8 Cluster. *RSC Adv* 2016, *6* (110), 108270–108279.

(14) Zheng, X.; Guo, S.; Guo, L. Ethanol Synthesis Catalyzed by Single Ni Atom Supported on Mo6S8 Support. *Appl Catal A Gen* 2018, *553*, 52–64.

(15) Timothy Hughbanks; Roald Hoffmann. Molybdenum Chalcogenides: Clusters, Chains, and Extended Solids. The Approach to Bonding in Three Dimensions. *J Am Chem Soc* 1983, *105* (5), 1150–1162.

(16) Andersen, O. K.; Klose, W.; Nohl, H. Electronic Structure of Chevrel-Phase High-Critical-Field Superconductors. *Phys. Rev. B* 1978, *17* (3), 1209–1237.

(17) Wang, J.; Li, X.; Wei, B.; Sun, R.; Yu, W.; Hoh, H. Y.; Xu, H.; Li, J.; Ge, X.; Chen, Z.; Su, C.; Wang, Z. Activating Basal Planes of NiPS3 for Hydrogen Evolution by Nonmetal Heteroatom Doping. *Adv Funct Mater* 2020, *30* (12), 1908708.

(18) Zhang, B.; Fu, X.; Song, L.; Wu, X. Computational Screening toward Hydrogen Evolution Reaction by the Introduction of Point Defects at the Ddges of Group IVA Monochalcogenides: A First-Principles Study. *J. Phys. Chem. Lett.* 2020, *11* (18), 7664–7671.

(19) Wang, Y.; Wang, D.; Gao, J.; Hao, X.; Li, Z.; Zhou, J.; Gao, F. Optimized Electronic Structure and P-Band Centre Control Engineering to Enhance Surface Absorption and Inherent Conductivity for Accelerated Hydrogen Evolution over a Wide PH Range. *Phys. Chem. Chem. Phys.* 2020, *22* (26), 14537–14543.

(20) Yang, T.; Xie, H.; Ma, N.; Liu, E.; Shi, C.; He, C.; Zhao, N. Unraveling the Mechanism of Hydrogen Evolution Reaction on Cobalt Compound Electrocatalysts. *Appl. Surf. Sci.* 2021, *550*.

(21) Perryman, J. T.; Hyler, F. P.; Ortiz-Rodríguez, J. C.; Mehta, A.; Kulkarni, A. R.; Velázquez, J. M. X-Ray Absorption Spectroscopy Study of the Electronic Structure and Local Coordination of 1st Row Transition Metal-Promoted Chevrel-Phase Sulfides. *J Coord Chem* 2019, *72* (8), 1322–1335.

(22) Wan, L. F.; Wright, J.; Perdue, B. R.; Fister, T. T.; Kim, S.; Apblett, C. A.; Prendergast, D. Revealing Electronic Structure Changes in Chevrel Phase Cathodes upon Mg Insertion Using X-Ray Absorption Spectroscopy. *Phys. Chem. Chem. Phys.* 2016, *18* (26), 17326–17329.

(23) Thole, F.; Wan, L. F.; Prendergast, D. Re-Examining the Chevrel Phase Mo6S8 Cathode for Mg Intercalation from an Electronic Structure Perspective. *R. Soc. Chem.* 2015, *19*, 22548–22551.

(24) Perryman, J. T.; Ortiz-Rodríguez, J. C.; Jude, J. W.; Hyler, F. P.; Davis, R. C.; Mehta, A.; Kulkarni, A. R.; Patridge, C. J.; Velázquez, J. M. Metal-Promoted Mo6S8 Clusters: A Platform for Probing Ensemble Effects on the Electrochemical Conversion of CO2 and CO to Methanol. *Mater. Horiz.* 2020, *7* (1), 193–202.

(25) Liu, C.; Liu, P. Mechanistic Study of Methanol Synthesis from CO2 and H2 on a Modified Model Mo6S8 Cluster. *ACS Catal* 2015, *5* (2), 1004–1012.

(26) Zhang, Q.; Guo, L.; Hao, Z. Computational Investigation of M1/W6S8 (M = Fe, Ru, and Os) Single-Atom Catalysts for CO2 Hydrogenation. *Catal. Surv. from Asia* 2018, *22* (4), 195–207.

(27) Zhang, Q.; Guo, L.; Hao, Z. Exploration of High-Performance W6S8-Supported Single-Atom Rh1 Catalysts for Reverse Water–Gas Shift Reaction and Methanol Formation via DFT Computational Study. *Polyhedron* 2018, *146*, 108–120.

(28) Zheng, X.; Guo, L.; Li, W.; Cao, Z.; Liu, N.; Zhang, Q.; Xing, M.; Shi, Y.; Guo, J. Insight into the Mechanism of Reverse Water-Gas Shift Reaction and Ethanol Formation Catalyzed by Mo6S8-TM Clusters. *Mol. Catal.* 2017, *439*, 155–162.

(29) Berry, F. J.; Gibbs, C. D.; Greaves, C. Structural Properties of the Molybdenum-Ruthenium Telluride of Composition. *J. Solid State Chem.* 1991, *92*, 148–153.

(30) Chevrel, R.; Gougeon, P.; Potel, M.; Sergent, M. Ternary Molybdenum Chalcogenides: A Route to New Extended Clusters. *J. Solid State Chem.* 1985, *57*, 25–33.

(31) Jaegermann, W.; Tributsch, H. Interfacial Properties of Semiconducting Transition Metal Chalcogenides. *Prog. Surf. Sci* 1988, *29* (112), 1–167.

(32) Malakhov, I. v.; Nikitenko, S. G.; Savinova, E. R.; Kochubey, D. I.; Alonso-Vante, N. In Situ EXAFS Study to Probe Active Centers of Ru Chalcogenide Electrocatalysts during Oxygen Reduction Reaction. *J. Phys. Chem. B* 2002, *106* (7), 1670–1676.

(33) Alonso-Vante, N.; Fieber-Erdmann, M.; Rossner, H.; Holub-Krappe, E.; Giorgetti, C.; Tadjeddine, A.; Dartyge, E.; Fontaine, A.; Frahm, R. The Catalytic Centre of Transition Metal Chalcogenides Vis-à-Vis the Oxygen Reduction Reaction: An in Situ Electrochemical EXAFS Study. *J. Phys. IV France* 1997, *7* (C2), 887-889.

(34) Jaegermann, W.; Pettenkofer, C.; Alonso Vante, N.; Schwarzlose, Th.; Tributsch, H. Chevrel Phase Type Compounds: Electronic, Chemical and Structural Factors in Oxygen Reduction Electrocatalysis. *Ber. Bunsenges. Phys. Chem.* 1990, *94* (4), 513–520.

(35) Alonso Vante, N.; Jaegermann, W.; Tributsch, H.; Hónle, W.; Yvon, K. Electrocatalysis of Oxygen Reduction by Chalcogenides Containing Mixed Transition Metal Clusters. *J Am Chem Soc* 1987, *2025*, 3251–3257.

(36) Mora-Hernández, J.; Luo, Y.; Alonso-Vante, N.; Mora-Hernández, J. M. What Can We Learn in Electrocatalysis, from Nanoparticulated Precious and/or Non-Precious Catalytic Centers Interacting with Their Support? *Catalysts* 2016, *6* (145), 1–55.

(37) Guo, L.; Han, Y.; Guo, S. Synthesis Gas Conversion over Cu and Ca Modified Model Mo6S8 Catalysts: A Systematic Theoretical Investigation. *Int J Hydrogen Energy* 2020, *45* (23), 12798–12814.

(38) Singstock, N. R.; Ortiz-Rodríguez, J. C.; Perryman, J. T.; Sutton, C.; Velázquez, J. M.; Musgrave, C. B. Machine Learning Guided Synthesis of Multinary Chevrel Phase Chalcogenides. *J Am Chem Soc* 2021, *143* (24), 9113–9122.

(39) Lilova, K.; Perryman, J. T.; Singstock, N. R.; Abramchuk, M.; Subramani, T.; Lam, A.; Yoo, R.; Ortiz-Rodríguez, J. C.; Musgrave, C. B.; Navrotsky, A.; Velázquez, J. M. A Synergistic Approach to Unraveling the Thermodynamic Stability of Binary and Ternary Chevrel Phase Sulfides. *Chem. Mater.* 2020, *32* (16), 7044–7051.

(40) Mançour-Billah, A.; Chevrel, R. The Transition Element Sulfo-Selenide Chevrel Phases: A New Way to Stabilize the Mo6(S,Se)8 Framework. *J Alloys Compd* 2004, *383* (1–2), 49–56.

(41) Belin, S.; Chevrel, R.; Sergent, M. Single Crystal Structural Investigations on Ni(y)Mo6Se(8-x)S(x) Solid Solution: A New Location of Nickel Counterions. *J Solid State Chem* 2000, *155* (1), 250–258.

(42) Mancour-Billah, A.; Gougeon, P.; Pivan, J. Y.; Sergent, M.; Chevrel, R. New Type-Structure of Chevrel Phase: Unusual Location of the 3d Chromium Ions in the Mo6S8 Host Lattice. *Croat. Chem. Acta* 1995, *68* (4), 891–899.

(43) Levi, E.; Gershinsky, G.; Aurbach, D.; Isnard, O.; Ceder, G. New Insight on the Unusually High Ionic Mobility in Chevrel Phases. *Chem. Mater.* 2009, *21* (7), 1390–1399.

(44) Yvon, K. On the Lattice Instabilities in Chevrel Phases. *Solid State Commun* 1978, *25* (5), 327–331.

(45) Levi, E.; Gershinsky, G.; Aurbach, D.; Isnarcr, O. Crystallography of Chevrel Phases, MMo6T8 (M = Cd, Na, Mn, and Zn, T = S, Se) and Their Cation Mobility. *Inorg. Chem* 2009, *48* (18), 8751–8758.

(46) Lu, K.; Xia, F.; Li, B.; Liu, Y.; Abdul Razak, I. B.; Gao, S.; Kaelin, J.; Brown, D. E.; Cheng, Y. Synergistic Multisites Fe2Mo6S8 Electrocatalysts for Ambient Nitrogen Conversion to Ammonia. *ACS Nano* 2021, *15* (10), 16887–16895.

(47) Arán-Ais, R. M.; Rizo, R.; Grosse, P.; Algara-Siller, G.; Dembélé, K.; Plodinec, M.; Lunkenbein, T.; Chee, S. W.; Roldan Cuenya, B. Imaging Electrochemically Synthesized Cu2O Cubes and Their Morphological Evolution under Conditions Relevant to CO2 Electroreduction. *Nat Commun* 2020, *11* (1).

(48) Li, Y.; Kim, D.; Louisia, S.; Xie, C.; Kong, Q.; Yu, S.; Lin, T.; Aloni, S.; Fakra, S. C.; Yang, P. Electrochemically Scrambled Nanocrystals Are Catalytically Active for CO 2-to-Multicarbons. *Proc. Natl. Acad. Sci.* 2020, 117(17), 9194-9201.

(49) Kim, Y. G.; Baricuatro, J. H.; Soriaga, M. P. Surface Reconstruction of Polycrystalline Cu Electrodes in Aqueous KHCO3 Electrolyte at Potentials in the Early Stages of CO2 Reduction. *Electrocatalysis* 2018, *9* (4), 526–530.

(50) Hahn, C.; Hatsukade, T.; Kim, Y. G.; Vailionis, A.; Baricuatro, J. H.; Higgins, D. C.; Nitopi, S. A.; Soriaga, M. P.; Jaramillo, T. F. Engineering Cu Surfaces for the Electrocatalytic Conversion of CO2: Controlling Selectivity toward Oxygenates and Hydrocarbons. *Proc Natl Acad Sci U S A* 2017, *114* (23), 5918–5923.

(51) Yang, Y.; Xiong, Y.; Zeng, R.; Lu, X.; Krumov, M.; Huang, X.; Xu, W.; Wang, H.; Disalvo, F. J.; Brock, J. D.; Muller, D. A.; Abrunã, H. D. Operando Methods in Electrocatalysis. *ACS Catal.* 2021, 11(3), 1136–1178.

(52) Timoshenko, J.; Roldan Cuenya, B. In Situ/ Operando Electrocatalyst Characterization by X-Ray Absorption Spectroscopy. *Chem. Rev.* 2021, 121 (2), 882–961.

(53) Monteiro, M. C. O.; Mirabal, A.; Jacobse, L.; Doblhoff-Dier, K.; Barton, S. C.; Koper, M. T. M. Time-Resolved Local PH Measurements during CO 2 Reduction Using Scanning Electrochemical Microscopy: Buffering and Tip Effects. *J. Am. Chem. Soc. Au* 2021, *1* (11), 1915–1924.

(54) Mayer, F. D.; Hosseini-Benhangi, P.; Sánchez-Sánchez, C. M.; Asselin, E.; Gyenge, E. L. Scanning Electrochemical Microscopy Screening of CO2 Electroreduction Activities and Product Selectivities of Catalyst Arrays. *Commun Chem* 2020, *3* (1), 155.

(55) Clark, E. L.; Singh, M. R.; Kwon, Y.; Bell, A. T. Differential Electrochemical Mass Spectrometer Cell Design for Online Quantification of Products Produced during Electrochemical Reduction of CO2. *Anal Chem* 2015, *87* (15), 8013–8020.

(56) Bondue, C. J.; Koper, M. T. M. A DEMS Approach for the Direct Detection of CO Formed during Electrochemical CO2 Reduction. *J. Electroanal. Chem.* 2020, *875, 113842*.

(57) Yao, Y.; Zhu, S.; Wang, H.; Li, H.; Shao, M. A Spectroscopic Study of Electrochemical Nitrogen and Nitrate Reduction on Rhodium Surfaces. *Angew. Chem., Int. Ed.* 2020, *59* (26), 10479–10483.

(58) Zeng, L.; Li, X.; Chen, S.; Wen, J.; Huang, W.; Chen, A. Unique Hollow Ni-Fe@MoS2 Nanocubes with Boosted Electrocatalytic Activity for N2 Reduction to NH3. *J Mater Chem A Mater* 2020, *8* (15), 7339–7349.

(59) Firet, N. J.; Smith, W. A. Probing the Reaction Mechanism of CO2 Electroreduction over Ag Films via Operando Infrared Spectroscopy. *ACS Catal* 2017, *7* (1), 606–612.

(60) Zhu, S.; Li, T.; Cai, W. bin; Shao, M. CO2 Electrochemical Reduction As Probed through Infrared Spectroscopy. *ACS Energy Lett.* 2019, 4, 3, 682–689.

(61) Kalz, K. F.; Kraehnert, R.; Dvoyashkin, M.; Dittmeyer, R.; Gläser, R.; Krewer, U.; Reuter, K.; Grunwaldt, J. D. Future Challenges in Heterogeneous Catalysis: Understanding Catalysts under Dynamic Reaction Conditions. *ChemCatChem* 2017, *9* (1), 17–29.

(62) Frenkel, A. I.; Rodriguez, J. A.; Chen, J. G. Synchrotron Techniques for in Situ Catalytic Studies: Capabilities, Challenges, and Opportunities. *ACS Catal.* 2012, 2, 11, 2269–2280.

(63) Weckhuysen, B. M. Determining the Active Site in a Catalytic Process: Operando Spectroscopy Is More than a Buzzword. *Phys. Chem. Chem. Phys.*, 2003,5, 4351-4360.

(64) Portela, R.; Perez-Ferreras, S.; Serrano-Lotina, A.; Bañares, M. A. Engineering Operando Methodology: Understanding Catalysis in Time and Space. *Front. Chem. Sci. Eng.* 2018, 12, 2095-0179.

(65) Negahdar, L.; Parlett, C. M. A.; Isaacs, M. A.; Beale, A. M.; Wilson, K.; Lee, A. F. Shining Light on the Solid-Liquid Interface: In Situ/Operando Monitoring of Surface Catalysis. *Catal. Sci. Technol.*, 2020,10, 5362-5385.

(66) Fischer. Chevrel Phases: Superconducting and Normal State Properties. *Applied Physics* 1978, *16* (1), 1–28.

(67) Bullett, D. W. Relation between Electronic Structure and Tc in Binary and Ternary Molybdenum Chalcogenides. *Phys Rev Lett* 1977, *39* (10), 664–666.

(68) Yvon K; Paoli A. Charge Transfer and Valence Electron Concentration in Chevrel Phases. *Solid State Commun.* 1977, *24*, 41–45.

(69) Mccallum, R. W.; Pobell, F.; Shelton, R. N. 125 Te Mossbauer Effect in Chevrel Phase Compounds Mo6(Se1-x Tex)8. *Phys. Lett.* 1982, *89* (6), 316–318.

(70) Berry, F. J.; Gibbs, C. Bonding in Mo4.5Ru1.5Te8, Ni0.85Mo6Te8, Chevrel Phase, and Related Compounds. *J. Solid State Chem.* 1994, *109*, 22–29.

(71) Sergent, M.; Fischer, Q.; Decroux, M.; Perrin, C.; Chevrel, R. Stabilization of Mo6S8 by Halogens; New Superconducting Compounds: Mo6SaBr2, Mo6S6I2. *J. Solid State Chem.* 1977, *22*, 87–92.

(72) Hamard, C.; Auffret, V.; Pena, O.; le Floch, M.; Nowak, B.; Wojakowski, A. Chevrel-Phase Solid Solution Mo6Se8-XTex. Study of Its Super-Conducting, Magnetic and NMR Properties. *Phys. B* 1999, *291*, 339–349.